INVESTIGATIONS OF MEMORY, ENTANGLEMENT, AND LONG-RANGE INTERACTIONS USING ULTRA-COLD ATOMS

A Thesis
Presented to
The Academic Faculty

by

Yaroslav O. Dudin

In Partial Fulfillment
of the Requirements for the Degree
Doctor of Philosophy in the
School of Physics

Georgia Institute of Technology
August 2012

INVESTIGATIONS OF MEMORY, ENTANGLEMENT, AND LONG-RANGE INTERACTIONS USING ULTRA-COLD ATOMS

Approved by:

Professor Alex Kuzmich, Advisor
School of Physics
Georgia Institute of Technology

Professor Shina Tan
School of Physics
Georgia Institute of Technology

Professor T. A. Brian Kennedy
School of Physics
Georgia Institute of Technology

Professor Dzmitry Matsukevich
Center for Quantum Technologies
National University of Singapore

Professor Ken Brown
School of Chemistry and Biochemistry
Georgia Institute of Technology

Dr. Steve Jefferts
Time and Frequency Division
National Institute of Standards and Technology

Dr. Jason Amini
Georgia Tech Research Institute
Georgia Institute of Technology

Date Approved: June 13, 2012

To my parents

ACKNOWLEDGEMENTS

I would like to start by thanking my thesis advisor Alex Kuzmich for his support, encouragement, and inspiration. I have been very fortunate to do my research in an environment as outstanding as his lab. Thanks to Alex I learned a great deal of physics and experimental tricks during my time at Georgia Tech. I thank him for his brilliant ideas, long hours of illuminating discussions (not always limited to physics), and great company.

The work constituting this thesis is a product of many years of collective effort and it would have been impossible without my colleagues. Five years ago, when I had just started working in the lab I was lucky to join Ran Zhao's quantum memory project. Coming from a vapor-cell experimental background, I was astonished with the complexity of the monster cold-atom setup. I would like to thank Ran for her patience and thoroughness when teaching me about every little detail of the experiment and helping me troubleshoot even after she had defended. It was my pleasure to work with Ran and I would like to thank her for being a great teammate and friend.

All neutral atom work in our lab rests on the foundation built up by Dima Matsukevich and Thierry Chanelière, and I would like to thank them for this. Even after they left the lab they continued to provide a strong influence. Thierry's idea about optical lattice geometry for the memory and Dima's help figuring out the data during his visits to Tech were indispensable. A special thanks to Dima for his continuing advice on experimental matters and his design of really neat pieces of electronics, such as his famous FPGA board.

I had the pleasure of sharing the lab with Shau-Yu Lan and Corey Campbell. Both supported me with great experimental advice, Shau-Yu during a one and a half

year overlap, and Corey throughout my entire stay at Georgia Tech, and I am very thankful for that.

I would like to thank Lin Li for all the work that he has done on our new generation memory effort and more recent Rydberg work. It was great luck that he joined our group two years ago and after a short time was single-handedly running the experiment and getting great results. I enjoyed every day working with him and never stopped being astonished by his determination and excellent data taking abilities.

I would like to thank our collaborators, Brian Kennedy and the members of his group, Stewart Jenkins, Richard Jen, and Francesco Bariani for their insightful theory, which over the years has proved to be very valuable. It was a pleasure and a privilege to work with them. Stewart provided vast contributions to the quantum memory projects, while Francesco's calculations were indispensable for the more recent Rydberg work. I would also like to thank Brian for his guidance and outstanding teaching of the quantum mechanics class, which was very useful and which I was very lucky to attend.

I am indebted to Alex Radnaev, my constant best friend since college for his company, great ideas, and optimism about everything. It has been a pleasure to work with him in the same labs in Troizk, Boulder, and Atlanta, especially on the joint telecom/memory experiments. He is a great guy and I would like to use this opportunity to enter this into permanent record.

The influence of those who I worked with before coming to Georgia Tech continues to be important. I would not probably be where I am now had I not joined Vladimir Velichansky's group in college. I would like to thank him for that opportunity, the enormous amount of science that I learned from him, and for being a great teacher and mentor. I am also indebted to Sergey Zibrov, a graduate student who I was working with closely at the time, and Vitali Vassiliev, a senior research scientist, for giving me experimental knowledge that has become invaluable.

I was incredibly fortunate to spend the summer before coming to Georgia Tech doing research at NIST in Boulder. The visit strongly influenced my decision to go to graduate school as well. I am most grateful to Steve Jefferts, Stefi Romisch, and Tom Heavner for giving me the opportunity to work on very interesting projects, teaching me a lot of the physics and engineering involved with precision timekeeping, and providing a really cool summer experience. I also thank Stefi and Steve for their support and continued friendship.

I would like to thank the undergraduate members of our group, including Dave Naylor, Jacob Blumoff, Anastasia Marchenkova, Amin Agha, Diya Radhakrishna, Michael Valdes, John Parker, and Alex Lind for keeping a fun and joyful atmosphere. Special thanks to Anastasia for the enormous help with the electronics and the new memory experiment (from the equipment rack to the new vacuum system and lasers).

I would like to thank the members of the Chapman group, including Chris Hamley, Eva Bookjans, Peyman Ahmadi, Chung-Yu Shin, Michael DePalatis, Thai Hoang, and Corey Gerving, for numerous discussions and borrowed equipment. A special thanks to Chris for his invaluable help with the design of the new memory vacuum system.

Finally, I would like to thank my parents, Oleg and Olga, for their encouragement of my early interest in science, their infinite love and support, and for always being the best company. This thesis is dedicated to you.

TABLE OF CONTENTS

LIST OF TABLES

LIST OF FIGURES

SUMMARY

Long-term storage of quantum information has diverse applications in quantum information science. This work presents an experimental realization of quantum memories with lifetimes greater then 0.1 s. The memories are based on cold rubidium atoms confined in one-dimensional optical lattices. First realization of lattice-based quantum memory and entanglement between a light field and a spin wave is presented in Chapter II. Chapter III describes two different methods (two-photon and magnetic) of compensation for inhomogeneous differential light shifts between the memory levels due to optical trapping potentials, and demonstration of entanglement between a telecom-band light field and a light-shift compensated memory qubit. Storage of coherent light pulses with $1/e$ lifetime of 16 s is demonstrated in a magnetically-compensated lattice augmented by a train of resonant population-inverting microwave π-pulses on the clock transition.

Highly excited Rydberg atoms present a unique platform for study of strongly correlated systems and quantum information, because of their enormous dipole moments and consequent strong, long-range interactions. In the experiment described in Chapter IV single collective Rydberg excitations are created in a cold atomic gas. After a variable storage period the excitations are converted into light. As the principal quantum number n of the Rydberg level is increased beyond ~ 70, no more than a single excitation is retrieved from the entire mesoscopic ensemble of atoms. In Chapter V, by spatially selective conversion of the spin wave into a light field, we demonstrate that Rydberg-level interactions create long-range correlations of collective atomic excitations. These results hold promise for studies of dynamics and

disorder in many-body systems with tunable interactions and for scalable quantum information networks. Chapter VI presents initial observations of coherent many-body Rabi oscillations between the ground level and a Rydberg level using several hundred cold rubidium atoms. The strongly pronounced oscillations indicate a nearly complete excitation blockade of the entire mesoscopic ensemble by a single excited atom.

CHAPTER I

INTRODUCTION

1.1 Study of quantum systems

A quantum many-particle system in which interactions can be tuned over a vast range may enable profound changes in the way we understand and explore physics of the microscopic realm [4]. For example, it may lead to novel phases of matter and aid in the discovery of new phenomena. Strong coupling allows for fast, controllable many-body dynamics, while the weakly interacting mode can be used for precise external manipulations and measurements. In the context of quantum information science, strong interactions are required to implement fast quantum gates and long-lived quantum memories can be realized in the non-interacting regime [5, 6].

Cold atomic gases are a fruitful platform for such studies. They permit one to perform experiments under well-understood and controlled conditions. Tuning the strength of short-range interactions can be accomplished using magnetic and optical Feschbach resonances [4, 7]. Resonant optical driving of an atomic gas between the ground and a high-lying Rydberg level is a particularly promising setting for studies of many-body systems with strong, long-range interactions [8, 9, 10, 11, 12, 13, 14, 15, 16]. On the other hand, ground state hyperfine levels are ideal for storing quantum states. Achieving long lifetimes for atomic coherence is therefore of major importance for quantum simulation and communication, as well as for several types of precision measurements.

1.2 Quantum memory

Protocols for quantum communication are typically based on remote parties sharing and storing an entangled quantum state. The generation of such remote entanglement must necessarily be done locally and distributed by light transmission over optical fiber links or through free space [17]. For the distribution of entanglement over a length L the characteristic timescale for storage is the light travel time L/c, where c is the speed of light in the medium. For $L = 1000$ km, $L/c \approx 5$ ms for an optical fiber.

In practice, direct entanglement distribution over optical fibers is limited by absorption to distances $l \sim 100$ km. In order to distribute entanglement over longer distances, the channel should be divided into links of length $\leq l$. The division circumvents attenuation in the fiber provided the intermediate memory nodes, which terminate the links, have a non-zero quantum memory time. Entanglement distributed over these shorter links is then connected over length L according to a family of protocols generically known as the quantum repeater. The entanglement distribution rate of a network depends critically on the memory time of these storage elements. For $L \sim 1000$ km, required memory times vary from many seconds for simple network topology [18, 19] to milliseconds for more complex (e.g., multiplexed) topologies and architectures [20, 21, 22]. Such long-lived quantum memories could revolutionize deterministic single photon sources [23] and lead to the generation of entangled states over extended systems [24]. This thesis presents the first experimental realization of long-lived quantum memory and light-matter entanglement based on optically trapped atoms.

Ground level coherences, for atoms at different positions in the lattice, will accumulate different phases due to the differential ac-Stark shift caused by the lattice field. This limited the memory lifetime to several milliseconds in our first experiments. The differential light shifts for degenerate atomic gases can be decreased by

employing colder atoms and shallower trap potentials [25]. A drawback of this approach is a small number of atoms and long sample preparation times, which make it very difficult to carry out protocols, such as DLCZ (Duan-Lukin-Cirac-Zoller), central to quantum repeater implementations [19].

For optical transitions in alkaline-earth atoms there exist special wavelengths of the lattice light at which the ac-Stark shifts for ground and excited states are identical. This is used in realizing high accuracy optical clocks [26]. In contrast, complete elimination of the ac Stark shift for the microwave ground level coherences of alkali atoms in optical lattices or micro-trap arrays did not appear to be feasible.

In this thesis I describe the elimination of the differential lattice Stark shift by employing a two-photon transition [6]. One leg of the transition is driven by the trapping field and the other involves a compensating laser field with a spatially uniform profile. Since the compensation field is uniform the compensating light shift profile is intrinsically aligned with the trapping field and therefore this technique is applicable to many trapping geometries.

A differential Stark shift-free lattice based on elliptically polarized light fields has been proposed [27, 28]. However, the scheme applies to hyperfine coherences which are first-order sensitive to magnetic fields, and therefore requires an extremely high degree of magnetic field control. More recently, Lundblad et al. have proposed, and demonstrated spectroscopically, that by mixing the two ground hyperfine levels with a dc magnetic field, it is possible to eliminate ac-Stark shift on the clock transition in an elliptically polarized lattice at a particular (magic) magnetic field value [29]. While the clock coherence becomes first-order sensitive to magnetic field, it is weakly so, and this is promising for greatly increased coherence times. This thesis describes the first measurements of increased clock coherence times using this technique. We achieve coherent light storage and retrieval in the atomic sample of $\sim 10^7$ rubidium atoms confined in a 1-D optical lattice at a temperature of ~ 10 μK, with lifetime

of 0.32 seconds, bettering previous results achieved via laser compensation [6] and in a shallow-lattice Mott insulator [25] by about 30%. In our most recent work we have achieved a 16 s lifetime for storage of coherent light pulses in a magnetically compensated optical lattice augmented by a refocusing microwave pulse sequence [30].

1.3 Telecom wavelengths

A long-distance quantum information network requires transmission between quantum memory elements at telecom wavelengths where absorption is minimized. Due to the paucity of suitable ground-state atomic transitions, a quantum memory coupled to telecom light has not been previously realized. In this thesis I describe its demonstration by wavelength conversion of the near-infrared light emitted on the ground-state transition, to telecom wavelengths. The conversion is achieved with a diamond configuration of electronic transitions, in an optically thick gas of cold rubidium. The quantum memory is also realized with atomic rubidium, trapped in a light-shift compensated optical lattice. Entanglement of a 795 nm light polarization qubit and an atomic Rb spin wave qubit for a storage time of 0.1 s is observed by measuring the violation of Bell's inequality ($S = 2.65 \pm 0.12$). By violating Bell's inequality ($S = 2.66 \pm 0.09$ at 10 ms storage) with memory and a light field after telecom down-conversion, transmission and up-conversion, we demonstrate a basic memory element for scalable quantum networking.

1.4 Quantum information with Rydberg atoms

Rydberg-level atoms possess long-range interactions which scale as $1/R^6$ in the van der Waals regime and $1/R^3$ in the dipole-dipole regime. While dipole-dipole interactions are normally operational for inter-atom distances R smaller than a critical distance $R_c \sim 10$ μm, their reach can be extended by microwave mixing of Rydberg levels of opposite parity [31]. The strength of these interactions for values of the principle quantum number $n \gtrsim 100$ can be comparable to the strength of the Coulomb

interaction between ions.

An important manifestation of Rydberg-level interactions is excitation blockade, where an atom promoted to a Rydberg level shifts the energy levels of nearby atoms, suppressing their excitation. Previously, excitation blockade has been used to prepare entangled states of two isolated atoms [32, 33] and has also been observed in atomic gases [34, 35, 36, 37, 38, 39, 40, 41]. However, controlled creation and manipulation of collective quantum excitations would open the door to investigations of interacting bosonic and fermionic fields, simulations of engineered quantum systems, and generation of complex entangled states of matter and light [8, 9, 10, 11, 12, 13, 14, 15, 16]. Encoding of quantum information into symmetrized many-atom quantum states, or spin waves, is particularly attractive as discrimination against various types of noise is built into the manipulation and measurement protocols [19, 42, 43]. Notably, atomic spin waves can be efficiently mapped onto light fields, making such systems naturally suited for distribution of quantum information among remote locations.

In this thesis I describe a series of experiments in which we studied collective single Rydberg excitations in an ultra-cold atomic gas. For a sufficiently small atomic sample and sufficiently high principal quantum numbers $n \sim 70$ of Rydberg levels, we observed that no more than a single excitation was retrieved from the entire mesoscopic ensemble of atoms. A prominent coherent multi-atom Rabi oscillation was also observed for a fully blockaded atomic sample. As the atomic sample size was increased we observed an emergence of long-range correlations between Rydberg spin waves. These results hold promise for studies of dynamics and disorder in many-body systems with tunable interactions and for scalable quantum information networks.

CHAPTER II

LATTICE-BASED QUANTUM MEMORIES

This chapter is based on Ref. [44, 45].

2.1 Long-lived quantum memory

2.1.1 Quantum memories based on atomic ensembles

A workhorse for atomic ensemble quantum memories is the DLCZ protocol, named after the authors: L.-M. Duan, M. D. Lukin, J. I. Cirac, and P. Zoller [19]. The basic idea is illustrated in Fig. 1. An optically thick sample of three-level atoms is prepared in state $|a\rangle$. A weak laser pulse with one photon detuning Δ from $|a\rangle$-$|c\rangle$ resonance illuminates the ensemble. With a small probability p_s, typically in the $10^{-3} - 10^{-4}$ range, a signal light field is scattered into a detection mode, defined by position of the single photon detector D_1. If a detection event by D_1has not occurred the atoms are reinitialized in state $|a\rangle$ by a strong cleaning pulse on $|b\rangle$-$|c\rangle$ transition and the sequence is repeated. A detection event by D_1 announces a successful creation of a collective spinwave $S \equiv 1/\sqrt{N}\sum_i e^{i(\mathbf{k_w}-\mathbf{k_s})\mathbf{r_i}}|a_i\rangle\langle b|$, where the sum is over all the atoms, $\mathbf{r_i}$ is the $i-$th atom position, $\mathbf{k_w}$ and $\mathbf{k_s}$ are the write and signal fields wave vectors respectively. The spin wave, which has the basic properties of a dark state polariton [46], may be stored for a desired time interval limited by decoherence and converted later into a single-photon idler light field by adiabatically switching on read field on the $|b\rangle$-$|c\rangle$ resonance.

Enhancing the matter coupling to a single spatial light mode is an advantage shared by cold optically thick atomic ensembles [42] and single atoms in high-finesse cavities [47]. The longest quantum memory time previously reported, 32 μs in a cold rubidium ensemble [23], is insufficient to carry out quantum repeater protocols over

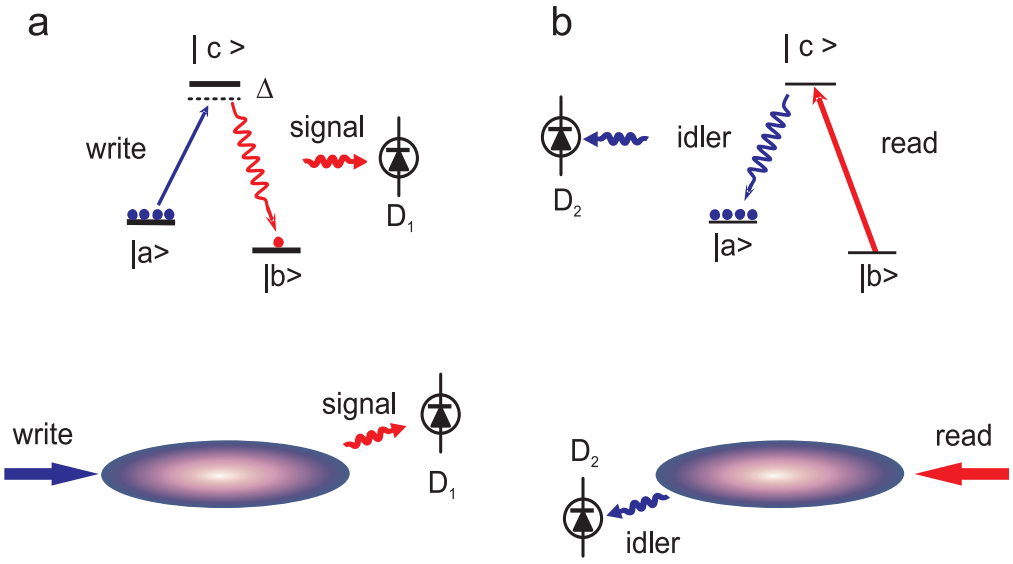

Figure 1: Illustration of the DLCZ protocol. Levels $|a\rangle$ and $|b\rangle$ are ground state hyperfine sublevels, level $|c\rangle$ is excited state. (a) Generation of a spin wave, write process. (b) Conversion of the spin wave into a light field, read process. D_1 and D_2 are single-photon detectors.

the distances where direct transmission fails. The rubidium sample, prepared in state of zero average magnetization, was allowed to freely fall during the protocol and the quantum memory time was limited by the effects of small uncompensated magnetic fields. In short, equally populated atomic states of opposite magnetization, $\pm m\mu_B$, where m is the angular momentum projection and μ_B is the Bohr magneton, respond asymmetrically to ambient fields [48, 49, 50, 51, 52, 53, 54, 55].

Ballistic expansion of the freely falling gas provides a longer memory time limitation which can be estimated from the time $\tau = \Lambda/(2\pi v) \sim 100$ μs it takes an atomic spin grating to dephase by atomic motion (we use some representative parameters typical of the MOT environment: grating wavelength $\Lambda = 50$ μm, atomic velocity $v = \sqrt{k_B T/M} \simeq 8$ cm/s for $T = 70$ μK). Millisecond storage of classical, coherent light has been reported in atomic gases [56, 57, 58], while coherence times in excess of 1 s have been achieved in the solid state [59].

2.1.2 Experimental setup

In order to demonstrate quantum memory lifetimes of many milliseconds we must suppress atomic motion and use magnetically-insensitive atomic coherence as the basis of the quantum memory. We achieve this goal by confining rubidium-87 atoms in an optical lattice of 25 μm period employing the $m = 0 \leftrightarrow 0$ ground-state atomic hyperfine transition for storage. We thereby take advantage of the magnetic insensitivity of the so-called clock transition, whose energy depends only quadratically on external magnetic fields. The ground hyperfine levels a and b of ^{87}Rb have angular momenta $F_a = 1$ and $F_b = 2$, and the upper and lower clock states are written as $|+\rangle \equiv |b, m = 0\rangle$ and $|-\rangle \equiv |a, m = 0\rangle$, respectively. If the atoms are prepared in the upper clock state by optical pumping, the $|+\rangle$ and $|-\rangle$ states can be coupled by Raman scattering of a weak linearly polarized *write* laser field into an orthogonally polarized signal field detected in the near-forward direction (Fig. 2).

As noted earlier, ballistic expansion limits the quantum memory time, and to increase it into the millisecond regime we load the atoms into a 1-D optical lattice as shown in Fig. 2. The period of the lattice 25 μm is shorter than the spin grating wavelength $\Lambda \simeq \lambda/\theta \approx 50$ μm, determined by the angle $\theta \approx 0.9^\circ$ between the write and signal fields of wavelength $\lambda = 795$ nm.

2.1.3 Lifetime and quantum statistics measurements

We optically pump the atoms into the $|+\rangle$ state. High retrieval efficiencies at long storage times are observed. In Fig. 3 two sets of data are shown, corresponding to maximum trap depths $U_0 = 40$ μK and $U_0 = 80$ μK, respectively, with a longer coherence time in the former case. All magnetic coherences are strongly suppressed by optical pumping, and, on the timescale shown, the fast magnetic coherences are completely dissipated, leaving primarily the clock hyperfine coherence. Atoms in the $|+\rangle$ and $|-\rangle$ clock states experience different, spatially varying light shifts in the

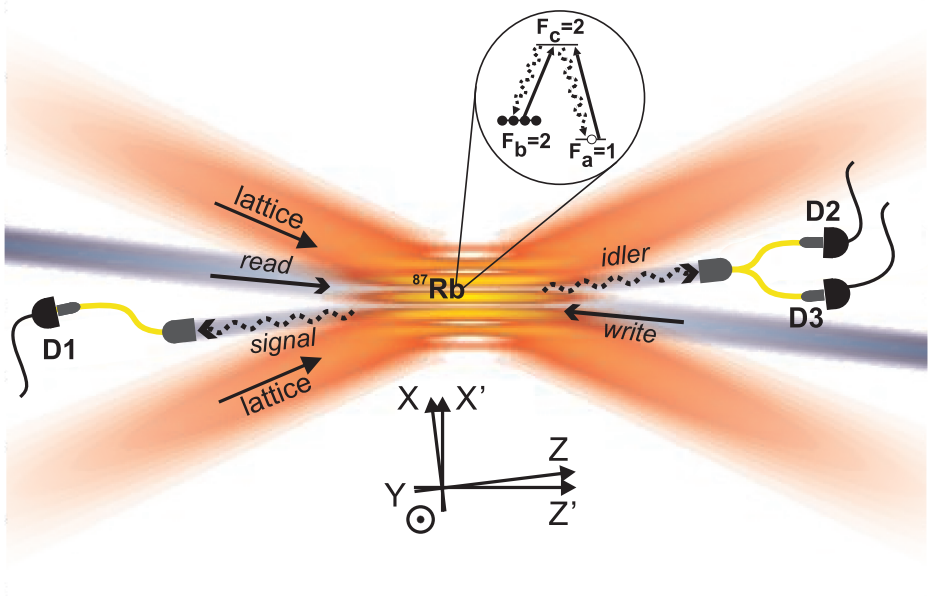

Figure 2: Essential elements of the experimental set-up. Between 10^5 and 10^6 sub-Doppler cooled ^{87}Rb atoms are loaded into an optical lattice, and detection of the signal field, generated by Raman scattering of the write laser pulse (red-detuned by 20 MHz), heralds the presence of a *write* spin wave excitation. A resonant *read/control* field converts the surviving atomic excitation into an idler field after a storage period T_s. The inset shows the atomic level scheme of ^{87}Rb with levels a and b the hyperfine components of the ground $5S_{1/2}$ level, and level c a hyperfine component of the excited $5P_{1/2}$ level.

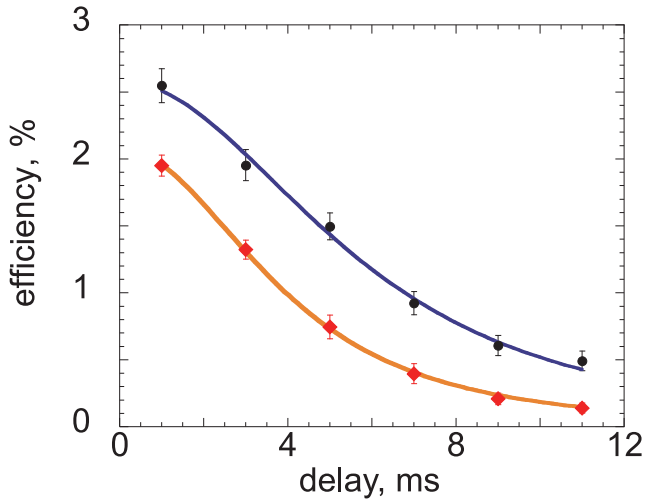

Figure 3: Retrieval efficiency as a function of storage time: optically pumped atoms in an optical lattice. Diamonds, trap depth $U_0 = 80$ μK; circles, $U_0 = 40$ μK. The solid lines are fits of the form $(1 + (t/T_c)^2)^{-3/2}$, with $T_c = 7.2 \pm 0.25$ ms (blue) and $T_c = 5.0 \pm 0.1$ ms (red) [1]. Error bars represent ± 1 standard deviation based on photoelectron counting statistics.

lattice. The observed millisecond-scale decoherence of the clock spin wave may be attributed to the atomic motion in the lattice potential, accompanied by the phase broadening resulting from the differential light shifts [1].

Having measured high retrieval efficiencies, we now demonstrate the quantum nature of the memory, on the 5 ms timescale. Specifically we characterize how well the retrieved idler field compares to a single photon state by measuring the α-parameter of Grangier et al. [60]. The value $\alpha = 0$ corresponds to an ideal, heralded single-photon state, whereas for classical fields $\alpha \geq 1$.

A field in a single-photon state incident on a beamsplitter is either transmitted or reflected, and the joint photoelectric detection probability vanishes. We determine α from the measured set of joint photoelectric detection probabilities on the three detectors, D1-3, Fig. 2. It is important to appreciate that α is weakly dependent on retrieval efficiency until the idler field background becomes significant [48], and

for this reason we do not expect α to significantly increase with storage time under the conditions of our experiment. Accounting for the measured signal field detection probability and efficiency, and idler channel background contribution, we theoretically estimate $\alpha \approx 0.02$ for 1.2 μs delay and $\alpha \sim 0.05 - 0.1$ for longer delays. In Table 1 we give the measured values of α, demonstrating quantum memory for storage times up to 6 ms. We have verified that detection of classical light with our protocol gives $\alpha = 0.97 \pm 0.08$, consistent with unity. Also shown in Table I are the corresponding values of the measured and intrinsic retrieval efficiencies obtained from the same data runs as the α-parameter. We note that the short time measured (6.3%) and intrinsic (25%) retrieval efficiencies are smaller than our previous values of 7.5% and 34%, respectively [23], due to the difficulty of spatially matching the lattice-loaded atomic sample and the signal-idler modes.

An important, immediate application of this long quantum memory is the realization of a deterministic single photon source based on quantum measurement and feedback, as proposed in Ref. [23]. There, the source was implemented using a freely expanding atomic cloud, with a quantum memory time of 32 μs, and two-photon events were reduced to 40% of the coherent state value [23]. As the protocol's success is based on long memory times, we are now able to significantly improve the quality of the single-photon source. The procedure closely resembles that used to measure retrieval efficiencies and α, with the following important distinction: instead of waiting for a period T_s after the signal detection event, we decide to read out the idler at time t_p. Hence, we begin the quantum feedback protocol at time $t_p - T_s$.

The quality of a deterministic single photon source is demonstrated by measuring sub-Poissonian photoelectron statistics of the second-order coherence function $0 \leq g_D^{(2)}(0) < 1$. The source efficiency, defined as the probability ϵ to detect a photoelectric event per trial, is the second important figure of merit. Ideally, $g_D^{(2)}(0) = 0$ and $\epsilon = 1$. The measured values of $g_D^{(2)}(0)$ and ϵ are given in Table 2. The former are comparable

Table 1: Measured values of α, measured efficiency η and intrinsic efficiency η_{int}.

T, ms	α	η	η_{int}
0.0012	0.02 ± 0.01	6.3%	25%
1	0.12 ± 0.04	2.8%	11%
4	0.17 ± 0.07	1.3%	5%
6	0.10 ± 0.10	1.1%	4.5%

Table 2: Measured values of $g_D^{(2)}(0)$, measured deterministic single photon source efficiency ϵ and intrinsic source efficiency ϵ_{int}.

t_p, ms	$g_D^{(2)}(0)$	ϵ	ϵ_{int}
4	0.06 ± 0.04	1.9%	8%
5	0 ± 0.06	1.6%	6%

to those recently achieved using a single trapped atom in a high-finesse cavity, while our measured efficiencies are about a factor of two greater [47].

2.2 Long-lived entanglement

In this section I describe an experiment in which we measure Bell inequality violation between signal and idler fields as a function of the delay, up to a value of 3.3 ms. This is achieved by storing orthogonal magnetically insensitive spin-waves while confining the atomic sample in a one-dimensional optical lattice to suppress the additional dephasing effects of atomic motion. In the experiment described in previous section, the clock transition between $m = 0$ hyperfine ground states was employed to reduce magnetic sensitivity. By contrast, in the experiment presented here the clock coherence plays a minor role and instead two orthogonal spin-waves associated with the $m = \pm 1 \leftrightarrow m' = \mp 1$ coherences are used to encode the long-lived atomic qubit. Moreover, the atoms are prepared in the $F = 1$ rather than $F = 2$ hyperfine ground level.

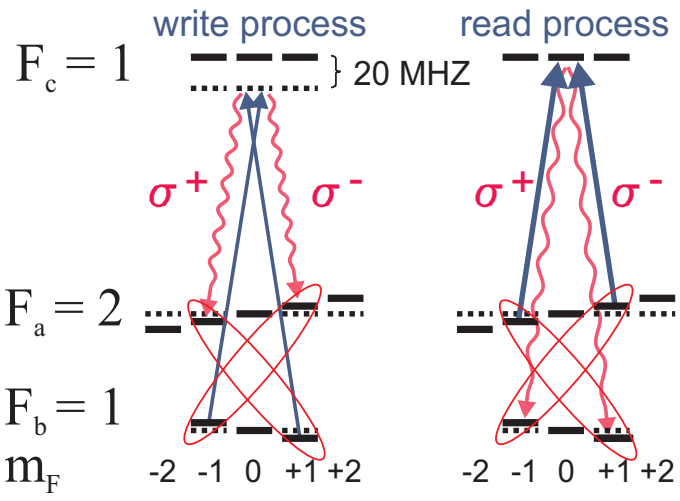

Figure 4: The ^{87}Rb levels $|a\rangle, |b\rangle$ and $|c\rangle$, associated with the D_1 line at 795 nm used in the write/read protocol, see text. $\{|a\rangle; |b\rangle\}$ correspond to the $5S_{1/2}, F = \{2, 1\}$ levels, and $|c\rangle$ represents the $\{5P_{1/2}, F = 1\}$ level. The atoms are assumed to be prepared in states $|b, m\rangle$ with populations $p_{|m|}$. Orthogonally polarized write and read lasers are assumed to counter-propagate along the quantization, z, axis. The Zeeman shifts are determined by a bias magnetic field directed along the z-axis.

2.2.1 Entanglement generation

Raman scattering of the write field from the ensemble creates a pair of excitations: a signal photon, and a correlated collective atomic excitation. The latter is comprised of the clock spin wave $\hat{s}_{0,0}(z)$ and the magnetic spin waves $\hat{s}^H_{m_b,m_a}(z) \equiv -i(\hat{s}_{m_b,m_a}(z) + \hat{s}_{-m_b,-m_a}(z))/\sqrt{2}$, $\hat{s}^V_{m_b,m_a}(z) \equiv (\hat{s}_{m_b,m_a}(z) - \hat{s}_{-m_b,-m_a}(z))/\sqrt{2}$, where $\hat{s}_{m_b,m_a}(z)$ is the local spin wave operator associated with the hyperfine transition $|b, m_b\rangle \leftrightarrow |a, m_a\rangle$, see Fig. 4. To lowest order in the coupling parameter $\chi \ll 1$ which scales with the product of dipole moments on the Raman transition and is inversely proportional to the write laser detuning [61], the joint signal-excitation density operator is given by $(1 + \chi\hat{\Phi}^\dagger)\hat{\rho}_0(1 + \chi\hat{\Phi})$, where $\hat{\rho}_0$ describes the atomic ground state, and

$$\hat{\Phi} \equiv \cos\eta \hat{a}_V \hat{A}_H + \sin\eta \hat{a}_H \hat{A}_V, \tag{1}$$

where $\cos^2\eta = (3 + 5p_0)/(6 + 8p_0)$, $\hat{a}_H$ and $\hat{a}_V$ are horizontal and vertical signal annihilation operators. Here p_0 and $p_1 = p_{-1}$ are occupation probabilities of $|b, 0\rangle$

and $|b,\pm1\rangle$, respectively, corresponding to an aligned state with zero orientation. The density operator describes an unpolarized atomic sample $p_0 = p_{\pm1}$, as well as a more general atomic state determined by cycles of the write process prior to signal detection. The atomic excitations correlated with emission of horizontally or vertically polarized signal fields, are described by annihilation operators

$$\hat{A}_H = \frac{\sqrt{2p_0}(i\hat{S}_{0,0} - \sqrt{3}\hat{S}^H_{0,2}) - \sqrt{3p_1}(\hat{S}^H_{1,-1} + \hat{S}^H_{1,1})}{\sqrt{3+5p_0}}, \tag{2}$$

and

$$\hat{A}_V = -\frac{\sqrt{2p_0}\hat{S}^V_{0,2} - \sqrt{p_1}(\hat{S}^V_{1,-1} - \hat{S}^V_{1,1})}{\sqrt{1+p_0}}, \tag{3}$$

respectively, where $\hat{S}^\lambda_{m_b,m_a} \equiv \int dz\sqrt{f(z)}\hat{s}^\lambda_{m_b,m_a}(z)$ and $\hat{S}_{0,0} \equiv \int dz\sqrt{f(z)}\hat{s}_{0,0}(z)$ are single-mode spin waves and $f(z) \equiv \bar{n}(z)/\int dz'\bar{n}(z')$ is the normalized spatial distribution function with $\bar{n}(z)$ the atomic density averaged over the transverse signal field mode [44]. We note that the emission of a horizontally polarized signal photon does not create a clock-type spin-wave excitation, but emission of both horizontally and vertically polarized photons results in a slowly varying spin excitation $S^{H/V}_{1,-1}$. The latter has a Larmor frequency proportional to the anomalous g-factor δg, which is 500 smaller than the Larmor frequencies of the $S^{H/V}_{0,2}$ and $S^{H/V}_{1,1}$ spin waves. In a bias magnetic field $B_0\hat{z}$, the Larmor frequencies for ^{87}Rb are given by $\omega_{m_a,m_b} = (\mu_B B_0/\hbar)[g_a(m_a+m_b) - \delta g m_a] + O(B_0^2)$, where $g_a = -0.5018$ and $g_b = 0.4998$ are Landé factors and $\delta g \equiv g_a + g_b = -0.002$. Since δg is so small the $O(B_0^2)$ contribution to the frequency $\omega_{1,-1}$ is not negligible. The differential change in $\omega_{1,-1}$ is quadratic in magnetic field at $B_0 = 3.2$ G [62].

The spin wave excitations are stored for a time T_s following the detection of the signal field. During this time the spin waves precess in the ambient magnetic field. As the field may vary spatially and temporally across the sample, the magnetic spin waves are dephased by the Zeeman effect. The corresponding dephasing rate is proportional to the spin wave Larmor frequencies and therefore the $S_{0,0}$ and $S^{H/V}_{1,-1}$ spin waves are

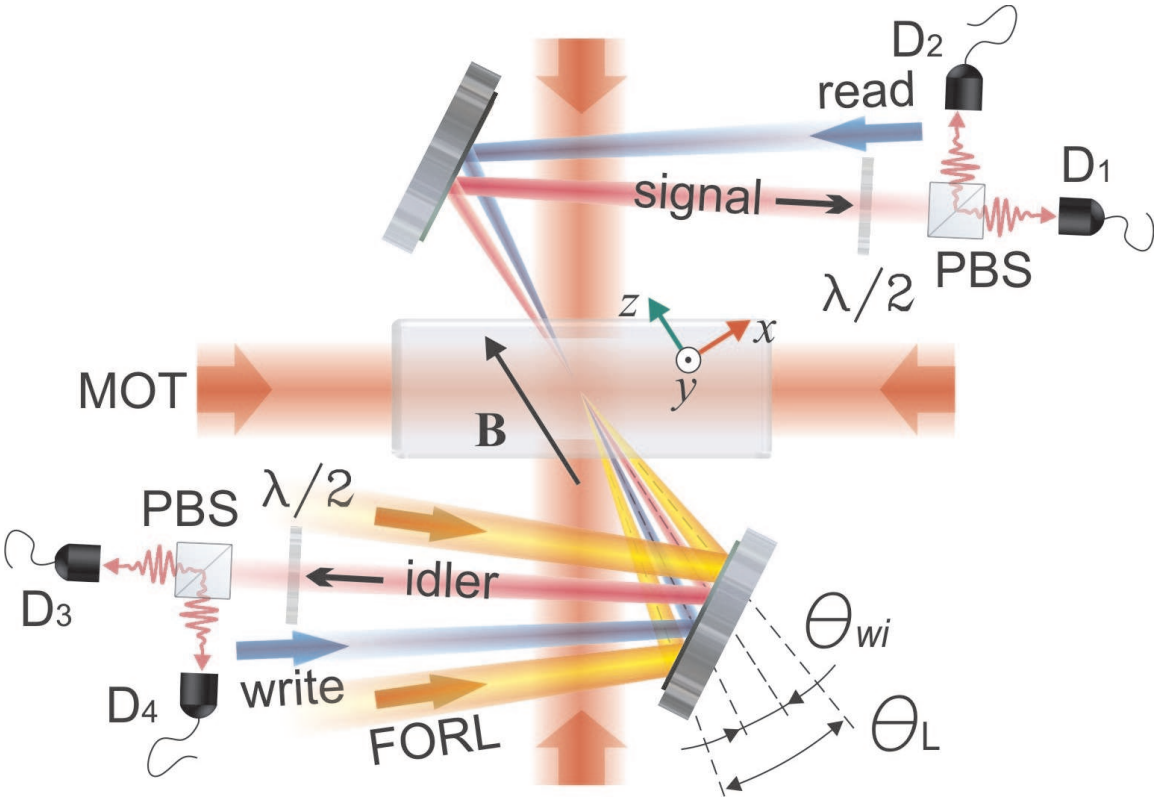

Figure 5: Schematic of optical lattice spin-wave qubit implementation. An atomic sample of about 10^7 ^{87}Rb atoms is loaded from a magneto-optical trap (MOT) in a 1-D far off-resonant optical lattice (FORL) of 25 μm period, formed by interfering two 7W, 1.06 μm beams with an angular separation $\theta_L = 2.5^o$. A bias magnetic field B points in the z direction. The beam waists, $1/e^2$, are 150 μm and 170 μm, respectively, giving a maximum trap depth of 100 μK. The write and read fields share a single spatial mode of waist 370 μm, while the signal and idler mode waist is 110 μm. The write/read and signal/idler modes intersect at the position of the atomic sample at an angle $\theta_{wi} = 0.9^o$. PBS is a polarizing beam splitter, and $\lambda/2$ labels a half-wave plate, D_1 through D_4 are single-photon detectors.

long-lived [44]. Under our experimental conditions the fast decoherence time $t_f \sim 100$ μs while the decoherence times for $S_{0,0}$ and $S^{H/V}_{1,-1}$ are expected to exceed the maximum storage time 3.3 ms employed here.

Following the storage period a read field of Rabi frequency Ω induces Raman conversion of the stored excitations into horizontally and vertically polarized idler fields, $\hat{\varphi}_H$ and $\hat{\varphi}_V$. For the atom-field configuration of Fig. 4 the read-out can be understood in terms of the dark-state polariton mechanism [63]. The local annihilation operators for the horizontally and vertically polarized polaritons are given by, with $\kappa\sqrt{\bar{n}}$ the dipole coupling frequency,

$$\hat{\Psi}_H(z) = \frac{\Omega^*\hat{\varphi}_H + \kappa^*\sqrt{5\bar{n}/6}\left[\sqrt{3p_0/8}\left(\sqrt{3}\hat{s}^H_{0,2} - i\hat{s}_{0,0}\right) + \sqrt{p_1}\left(\hat{s}^H_{1,1} + \hat{s}^H_{1,-1}\right)\right]}{\sqrt{|\Omega|^2 + 5\bar{n}|\kappa|^2\left(2+p_0\right)/12}}, \quad (4)$$

$$\hat{\Psi}_V(z) = \frac{\Omega^*\hat{\varphi}_V + \kappa^*\sqrt{5\bar{n}/6}\left[\sqrt{2p_0}\hat{s}^V_{0,2} + \sqrt{p_1}\left(\hat{s}^V_{1,1} + \hat{s}^V_{1,-1}\right)\right]}{\sqrt{|\Omega|^2 + 5\bar{n}|\kappa|^2\left(1+p_0\right)/6}}. \quad (5)$$

The joint signal-idler detection rates are given by

$$C(\theta_s,\theta_i;T_s) \propto \Big|\cos\eta[\hat{\Upsilon}_H(T_s),\hat{A}^\dagger_H]\sin\theta_s\cos\theta_i - \sin\eta[\hat{\Upsilon}_H(T_s),\hat{A}^\dagger_H]\cos\theta_s\sin\theta_i\Big|^2, \quad (6)$$

where $\hat{\Upsilon}_H(T_s) = \int dz\sqrt{f(z)}\Psi_H(z,T_s)|_{\Omega=0}$, θ_s and θ_i are signal and idler polarization angle settings, respectively, with $\theta_{s,i} = 0$ corresponding to horizontally polarized fields. The commutators quantify the overlap of the written spin waves (Eqs. (2,3)) with the matter-excitation available for read-out (Eqs. (4,5)) and its dependence on the alignment of the initial atomic state. Measurements of these joint detection rates, as a function of T_s, enable us to determine the Bell parameter S and thus to study violation of Bell's inequality $|S| \leq 2$. The commutators in Eq. (6) involve spatial integration of phase factors in which a spatially varying Larmor frequency multiplies T_s. This is the origin of the spin wave dephasing, washing out fast spin waves in a time $T_s \simeq 100$ μs, leaving only the slow spin wave contributions at longer times.

2.2.2 Experimental setup

The main elements of our experiment are shown in Fig. 5. A sample of 10^9 Rb-87 atoms is collected and cooled in a magneto-optical trap for a period of 0.5 s. The trap laser is then detuned 90 MHz below atomic resonance, the quadrupole magnetic field is turned off and the repump laser intensity is lowered for 20 ms, in order to optimize sub-Doppler cooling and loading of the optical lattice. As a result, the lattice contains about 10^7 atoms in the $5S_{1/2}, F = 1$ hyperfine level. The lattice parameters, see caption of Fig.5, result in the oscillation frequencies $3 \cdot 10^3$, 200 and 8 Hz. The transverse temperature of the cloud was measured to be 20 μK.

After loading, we apply a 0.66 G bias magnetic field in the z direction and initiate a write/signal measurement sequence of maximum duration 36 ms. The sequence begins with a 50 ns long vertically polarized incident write pulse of power 1 μW. The pulse is detuned by -20 MHz from the $|b\rangle \rightarrow |c\rangle$ transition. The Raman scattered signal field, on the $|c\rangle \rightarrow |a\rangle$ transition, is collected and passed through a half-wave plate, and a polarizing beam splitter followed by single photon detectors D_1 and D_2. In the absence of a photoelectric detection event registered by either D_1 or D_2 the write pulse is followed by an orthogonally polarized clean pulse, duration 200 ns, power 270 μW, which transfers atomic population back from $|a\rangle$ to $|b\rangle$, and the sequence is repeated at a frequency of 0.66 MHz. A detection event at D_1 or D_2 (with probability 10^{-4}) heralds the excitation of an atomic spin-wave with the desired wave vector and the write/signal measurement sequence is stopped.

2.2.3 Bell inequality violation

The collective atomic excitation is stored for a time $2\pi n/\omega_{1,-1} = 0.54n$ ms for $B_0 =$ 0.66 G, where n is an integer. Then a horizontally polarized read laser pulse (identical to the clean pulse), and counter-propagating with the write pulse, induces Raman scattering, converting the stored spin wave excitation into an idler field emitted on the

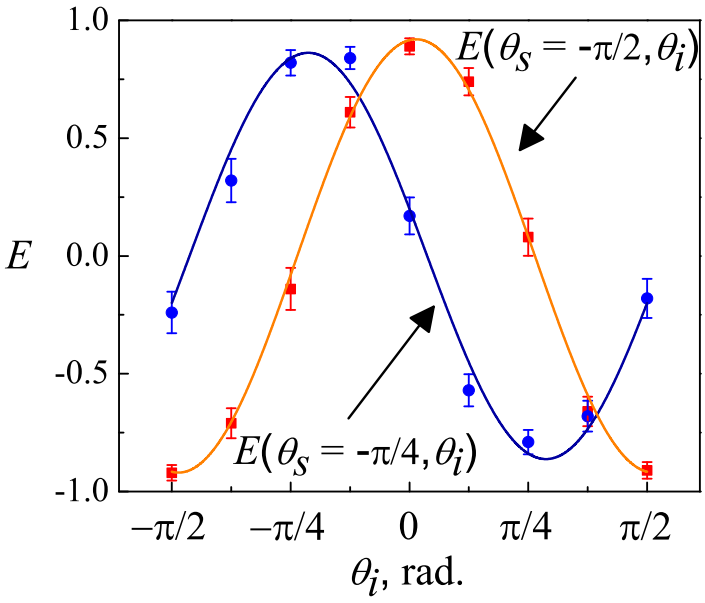

Figure 6: Measured correlation function $E(\theta_s, \theta_i)$ after the first Larmor period of $2\pi/\omega_{1,-1} = 0.54$ ms. The curves are sinusoidal fits to the data.

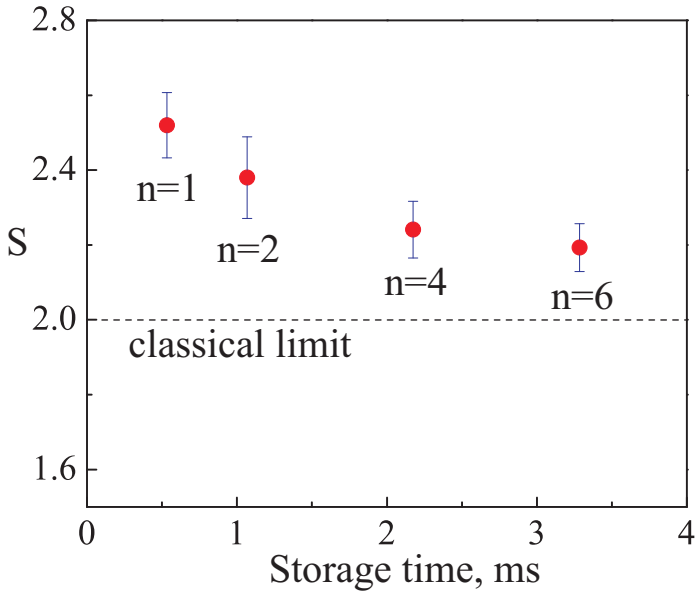

Figure 7: Measured values of the Bell parameter S as a function of storage time, for an integer number $n = 1, 2, 4, 6$ of Larmor periods of 0.54 ms.

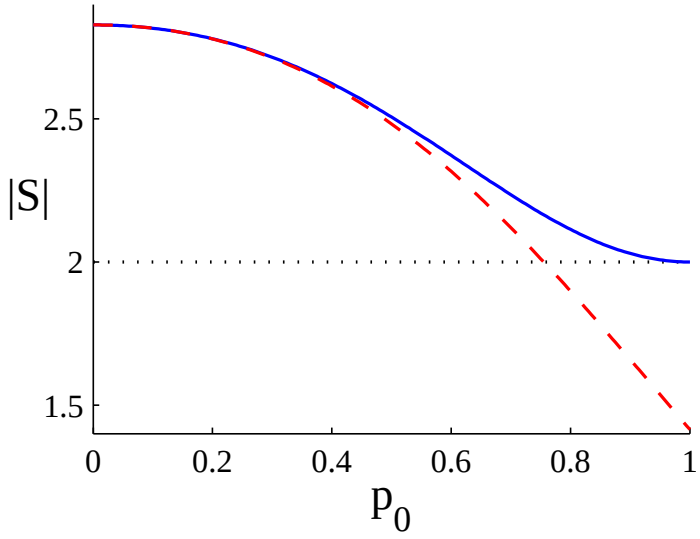

Figure 8: Theoretical values of Bell's parameter as a function of p_0 for the canonical angles used in the experiment (red) and for optimized angles (blue).

$|c\rangle \rightarrow |b\rangle$ transition. The write, read, and detected signal and idler field wavevectors satisfy the phase-matching condition $\mathbf{k}_w + \mathbf{k}_r = \mathbf{k}_s + \mathbf{k}_i$, ensuring high-efficiency read-out of the spin-wave excitation. The idler field is passed through a half-wave plate, followed by a polarizing beam splitter, onto a pair of single photon detectors D_3 and D_4. To account for unequal propagation and detection efficiencies the signal and idler polarizations are rotated by $\pi/2$ every 20 minutes. The idler photodetection probability varied between 0.5% and 0.25% for the data presented in Fig. 7.

The resulting joint signal-idler detection rates $C_{ij}\,(\theta_s, \theta_i)$, $i = 1, 2, j = 3, 4$ exhibit sinusoidal variations as a function of the orientations of the waveplates, in agreement with Eq. (6). We check for Bell inequality violation $|S| \leq 2$ by measuring polarization correlations between signal and idler fields at certain canonical angles, where $S = E(-\pi/2, -\pi/8) + E(-\pi/2, \pi/8) + E(-\pi/4, -\pi/8) - E(-\pi/4, \pi/8)$, here the correlation function $E(\theta_s, \theta_i)$ is given by [64, 65, 66]

$$\frac{C_{13}(\theta_s, \theta_i) + C_{24}(\theta_s, \theta_i) - C_{14}(\theta_s, \theta_i) - C_{23}(\theta_s, \theta_i)}{C_{13}(\theta_s, \theta_i) + C_{24}(\theta_s, \theta_i) + C_{14}(\theta_s, \theta_i) + C_{23}(\theta_s, \theta_i)}.$$

Table 3: Measured correlation function $E(\theta_s, \theta_i)$ and S for 3.3 ms storage time based on 2702 events.

θ_s	θ_i	$E(\theta_s, \theta_i)$
$-\pi/2$	$\pi/8$	0.474 ± 0.033
$-\pi/2$	$-\pi/8$	0.630 ± 0.030
$-\pi/4$	$\pi/8$	0.593 ± 0.031
$-\pi/4$	$-\pi/8$	-0.496 ± 0.034
		$S_{exp} = 2.19 \pm 0.06$

The measured sinusoidal variation of $E(\theta_s, \theta_i)$ as a function of θ_i for fixed θ_s is shown in Fig. 6. In Fig. 7 we show the measured Bell parameter S after $n = 1, 2, 4,$ and 6 Larmor periods: for n=6 (a 3.3 ms storage period) the data are presented in Table 3. The acquisition time varied from 5 hours ($n = 1$) to 32 hours ($n = 6$) for the data points in Fig. 7. As one might expect, $|S|$ decreases, but exceeds two by more than three standard deviations. The rate of decay is consistent with motional dephasing due to differential light shifts, as previously observed [44], while the expected magnetic decoherence rates of the slow coherences are at least an order of magnitude smaller.

From the theoretical analysis presented earlier, Eq. (6), we can calculate the Bell parameter as a function of p_0. For the canonical angles chosen in the experimental measurements we find that $|S|$ is a monotonically decreasing function $\sqrt{2} \leq |S| \leq 2\sqrt{2}$. Rather than give a full analytic expression we plot $|S|$ in Fig. 8 and note that for $p_0 \ll 1$, $|S| = 2\sqrt{2} - \frac{25}{16\sqrt{2}}\left(p_0^2 + \frac{1}{2}p_0^3\right) + O(p_0^4)$. From Fig. 8 the short time data of Fig. 7 is consistent with values of $p_0 \leq 0.6$, including $p_0 = 1/3$ for an unpolarized sample. Numerical calculations of the protocol suggest that p_0 falls from its initial value of 1/3 to a steady state value of 0.15 within the first few milliseconds of the 36 ms write protocol. Our investigations of populations dynamics are reported in Ref. [67].

CHAPTER III

LIGHT-SHIFT COMPENSATED QUANTUM MEMORIES

This chapter is based on Ref. [6, 68, 69, 30].

3.1 Two-photon compensation

3.1.1 Differential light shift

As hyperfine sublevels of the ground state see inhomogeneous trapping potentials, a spatially varying ac Stark shift, proportional to the local light field intensity, is induced, as shown in Fig. 9(a), leading to memory dephasing on the scale of several milliseconds. A technique to compensate the differential ac Stark shift in an optical trap using a laser field tuned between the two ground hyperfine levels has been proposed and demonstrated in a near-resonant Gaussian beam trap [70]. However, this scheme requires spatial matching of the local field intensity profiles of the near-resonant compensating light and the trap. This is difficult to realize for far-off-resonance optical lattices and trap arrays, which necessarily operate at different wavelengths.

In this chapter I describe how the differential lattice Stark shift can be eliminated by employing a two-photon transition. One leg of the transition is driven by the trapping field and the other involves a compensating laser field with a spatially uniform profile. The two-photon transition is detuned by Δ_2 from the $|a\rangle - |e\rangle$ resonance, Fig. 9(b). In this scheme the spatially varying light shifts of the clock states can be made identical with a suitable choice of the compensating field frequency and intensity. As shown below, the compensation condition is approximately $\Omega_c^2 = -4\Delta_2\Delta_{\rm hfs}$, where Ω_c is the compensation field Rabi frequency and $\Delta_{\rm hfs}/(2\pi) = 6.8$ GHz the ground state hyperfine splitting of ^{87}Rb.

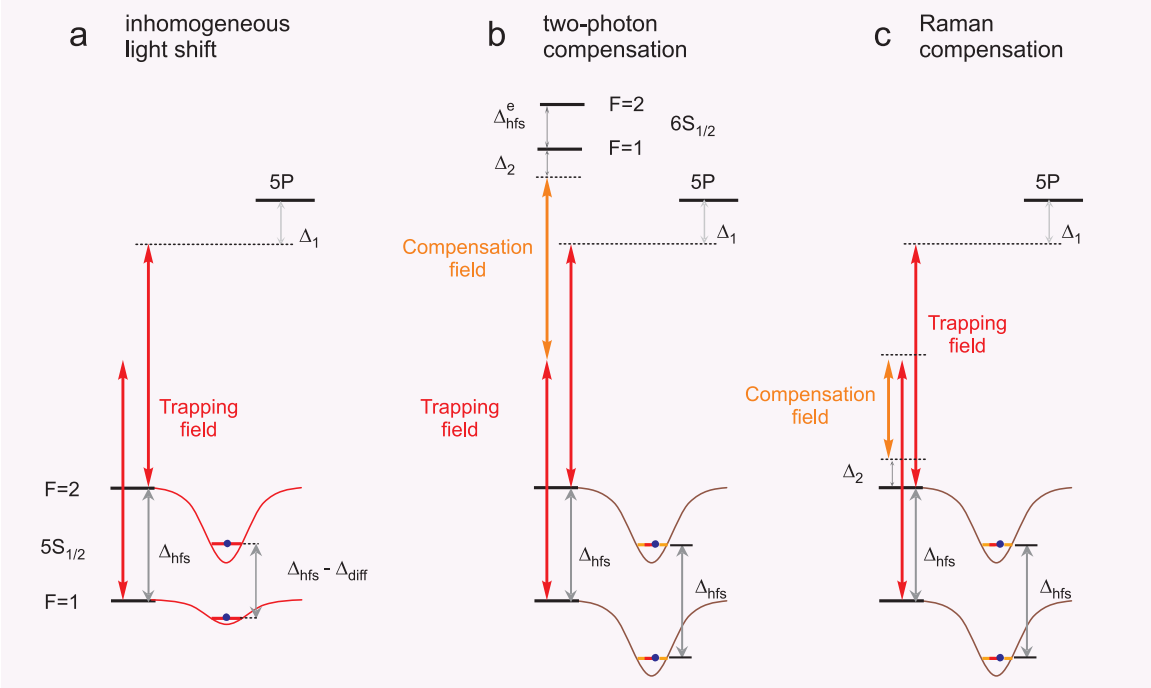

Figure 9: Illustration of the inhomogeneous differential Stark-shift in optically trapped atoms and its compensation with two-photon transitions. (a) The shift occurs because the trapping field has different detunings for the hyperfine levels, resulting in a deeper trap for the higher level. (b) A compensation field of the right frequency and amplitude creates an additional two photon Stark-shift for the lower level, which eliminates the differential Stark-shift. (c) Two-photon compensation in Raman configuration.

3.1.2 Compensation principles

In an optical trap the ground state hyperfine levels have different detunings, leading to an inhomogeneous differential Stark-shift $\Delta_{\rm diff}(\mathbf{r}) = \frac{\Delta_{\rm hfs}}{\Delta_1}\frac{\mathrm{U}(\mathbf{r})}{\hbar}$, where $\mathrm{U}(\mathbf{r}) = \frac{\hbar\Omega_{\rm t}^2(\mathbf{r})}{4\Delta_1}$ is the trapping potential, and $\Omega_{\rm t}(\mathbf{r})$ is the Rabi frequency of the trapping field (Fig. 9(a)). At trap depths and temperatures on the order of 40 μK this light shift limits the memory lifetime to $\tau \sim 1/\overline{\Delta_{\rm diff}(\mathbf{r})}$ ~10 ms (averaging over the atomic density). In this work, the differential Stark shift is suppressed by a compensation field of Rabi frequency $\Omega_{\rm c}$, which produces two-photon light shifts of different values for the two hyperfine levels ($F = 1,2$): $\delta_{\rm c}^{(\rm F)}(\mathbf{r}) = (\frac{\Omega_{\rm c}\Omega_{\rm t}(\mathbf{r})}{2\Delta_1})^2/(4\Delta_2^{(\rm F)})$ (Fig. 9(b)). For our conditions of hyperfine splittings and detunings, $\delta_{\rm c}^{(2)}$ is negligible, and for simplicity we account for only $\delta_{\rm c}^{(1)}$, omitting the superscript. In the presence of the compensating field the differential Stark shift changes to

$$\Delta_{\rm diff}^{'}(\mathbf{r}) = \Delta_{\rm diff}(\mathbf{r}) + \delta_{\rm c}(\mathbf{r}) = \frac{\mathrm{U}(\mathbf{r})}{\hbar\Delta_1}(\Delta_{\rm hfs} + \frac{\Omega_{\rm c}^2}{4\Delta_2}), \tag{7}$$

which vanishes when $\Omega_{\rm c}^2 = -4\Delta_2\Delta_{\rm hfs}$; for a given compensation field intensity, there is a detuning which eliminates the inhomogeneous differential light shift. In practice, $\Omega_{\rm c}$ is not perfectly homogeneous, leaving an average differential light shift $\overline{\Delta_{\rm diff}^{'}} = \frac{1}{2\tau}(\frac{w_{\rm a}}{w_{\rm c}})^2/(1 + (\frac{w_{\rm a}}{w_{\rm t}})^2)$, where w_a is the radius of the atomic sample, and $w_{\rm c}, w_{\rm t}$ are the waists of the Gaussian compensation and trapping fields, respectively. Since the lifetime enhancement scales as $(\frac{w_{\rm c}}{w_{\rm a}})^2$, compensation can be obtained with reasonable beam waists. The compensation comes at the expense of two-photon scattering, which limits the lifetime. The rate of scattering $R \sim \Delta_{\rm diff}\frac{\Gamma_e}{\Delta_2}$ provided $\Delta_2 \lesssim [\Delta_{\rm hfs} - \Delta_{\rm hfs}^e]/2$. Hence, the maximum value of the lifetime enhancement is of the order $(\Delta_{\rm hfs} - \Delta_{\rm hfs}^e)/(2\Gamma_e)$; Here $\Gamma_{\rm e}$ is the natural linewidth of the level $|e\rangle$. For our case of $|e\rangle = |6S_{1/2}F = 1\rangle$, the maximum enhancement is $\sim 10^3$.

The enhancement factor can in principle be increased by choosing a smaller Γ_e (e.g., by employing a Rydberg level). Alternatively, for a circularly-polarized optical

lattice, the two-photon transition could begin and terminate on the ground clock states (forming a Λ-scheme, Fig. 9(c)). In this case the compensation field would be a frequency-shifted (by $\Delta_{\rm hfs} \pm \Delta_{\rm 2ph} \approx 2\pi \times 6.8$ GHz) component of the trapping laser field. Since $|e\rangle$ is a ground clock state, $\Gamma_e = 0$ and the lifetime enhancement is expected to be limited by inhomogeneity of the compensating field across the atomic cloud. Population transfer between the clock states is negligible when $(\Omega_{\rm 2ph}/\Delta_2)^2 << 1$, where $\Omega_{\rm 2ph}$ is the effective two-photon Rabi frequency.

3.1.3 Experiment

We load ^{87}Rb atoms into a magneto-optical trap (MOT) from a background vapor. After compression and precooling the atoms are transferred to a one dimensional optical lattice resulting in an approximately cigar shaped cloud of $\sim 10^7$ atoms with $1/e^2$ waists of 130 μm and 840 μm (Fig. 10). The lattice is formed by interfering two linearly polarized 1064 nm beams intersecting at an angle of 9.6° in the horizontal plane (6.3 μm period). The beams have waists of $\sim$200 μm and their total power is varied between 8 W and 14.6 W. After loading, a bias magnetic field is applied along the major axis of the trap and atoms are prepared in the $|5^2S_{1/2}$ F = 1;m = 0$\rangle$ state by means of optical pumping.

The write, read, signal, and idler fields are arranged in a non-collinear phase-matched geometry, resulting in a stored spin wave grating of 50 μm period. The atoms are prepared in the $|b, m = 0\rangle$ ground state by optical pumping. The compensating beam has wavelength 931 nm and a Gaussian beam profile with waist size 0.46 mm and power 498(15) mW, stabilized by current feedback to the tapered laser amplifier. While the lattice laser is drifting at the level of $\sim$ 1 GHz, the two-photon detuning is stabilized to the value $\Delta_2 = -2\pi \times 235$ MHz from the $|a\rangle \rightarrow |e\rangle$ transition via the frequency locking to a Doppler-free atomic fluorescence signal from a heated vapor cell (Appendix A).

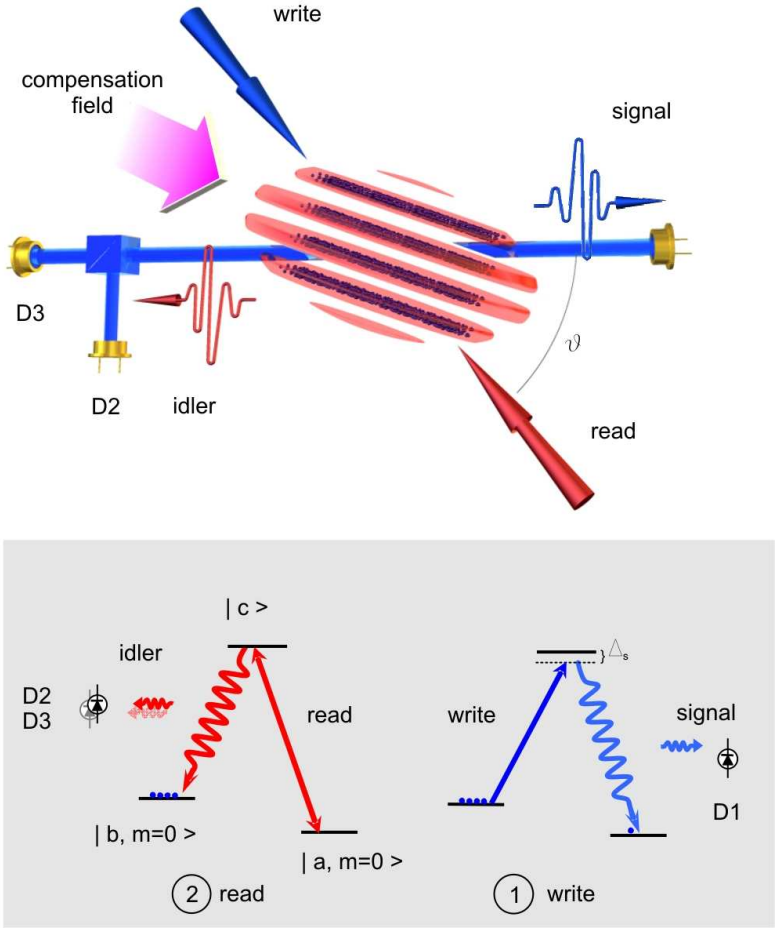

Figure 10: Long-lived quantum memory based on the first-order magnetically insensitive hyperfine coherences in sub-Doppler cooled ^{87}Rb atoms, confined in a 6 μm period 1D lattice with compensated differential Stark-shift. A weak write laser pulse, red detuned from the $b \leftrightarrow c$ transition generates pairs of atomic spin wave excitations and write signal field photons by Raman scattering. Signal detection at D1 initiates a controlled storage period after which a read laser pulse, resonant to the $a \leftrightarrow c$ transition converts the stored spin-wave into an idler field by backward Raman scattering. The idler is directed to a beam splitter, step 5, followed by detectors D2 and D3, where photoelectric correlations are determined from the record of detection events. The Gaussian spot size of the signal/idler mode is 110 μm. The coherence time of the atomic excitations is enhanced by means of a laser field, which compensates the differential lattice ac Stark-shift.

We first test and optimize the performance of the light-shift-compensated memory by observing storage and retrieval of classical coherent light, as a function of optical lattice potential depth. It is achieved by coupling the light (backwards) into the signal field fiber, Fig. 10, while the read light is used in the role of the control field. This geometry ensures that the stored spin waves are of the same 50 μm period and of similar spatial envelope as for the single excitations created via the DLCZ protocol. The retrieved coherent idler field (average photon number per pulse $\langle n \rangle \simeq 10^3$) is directed onto a linear avalanche photodetector (in lieu of single-photon detectors D2 and D3). The storage and retrieval efficiency ϵ is defined as the ratio of the measured pulse energy with storage and retrieval, to that of a directly transmitted sample with no atoms. As such, it is by fiat normalized by the passive transmission and detection losses.

With an intense laser light source the data integration times are considerably shorter, and the tolerable background noise level is much higher than in the single photon regime. By comparing the measured lifetime in traps of various depths we observe a factor of approximately 10 lifetime enhancement; see the comparison data for a 48 μK trap in Fig. 11. The maximum memory lifetime of 165 ms is observed for the shallowest, $U_0 = 33$ μK, trap. Longer lifetimes could be readily observed using shallower traps at the cost of reduced retrieval efficiency associated with fewer trapped atoms. The enhancement factor is limited by spontaneous emission from level $|e\rangle$ and alignment and inhomogeneity of the compensation field across the atomic sample. These contributions are largely determined by the power of the compensation laser diode amplifier system, so that the storage time could be further increased with a more intense light source.

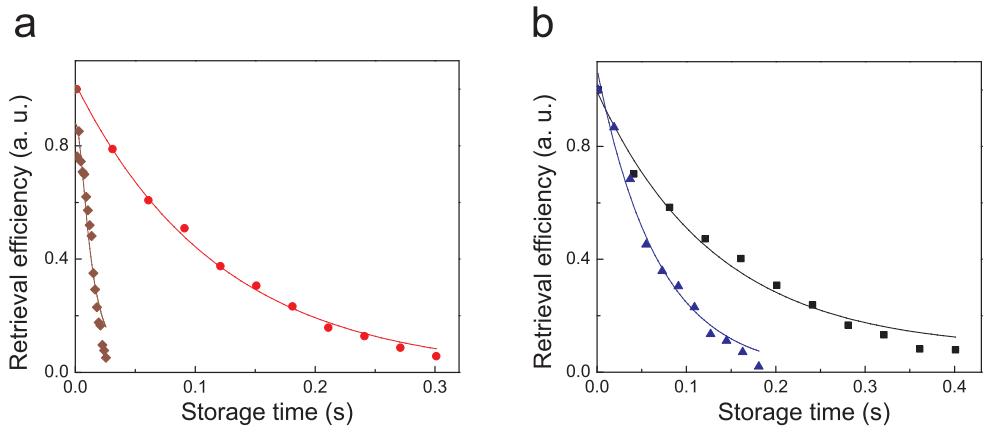

Figure 11: Retrieval efficiencies for classical light. The solid lines are fits of the form e^{-T/T_c} for lattice with compensation, and $(1+(T/Tc)^2)^{-3/2}$ without one. (a) At U_0=48 μK the lifetime T_c increases from 12 ms without compensation (diamonds) to 120 ms with compensation (circles), giving retrieval efficiencies 3.8% and 3.1%, respectively, for zero storage time. (b) The longest lifetime T_c = 165 ms is observed at U_0=33 μK with 1.6% efficiency (squares). The maximum efficiency of 4.0% is measured at U_0=62 μK with T_c = 68 ms (triangles). The efficiencies quoted for classical light storage are intrinsic, i.e., normalized by the transmission and detection losses.

3.1.4 Quantum correlations

Having verified the long-term coherence of the memory using classical light storage, we implement single photon storage using the experimental setup shown in Fig. 10. We perform single photon generation, storage, and retrieval based on the Duan-Lukin-Cirac-Zoller protocol. We first confirm that the compensation field technique leads to enhanced memory times in the quantum regime, that is the ac Stark shift induced dephasing that limited previous quantum memories is suppressed without the addition of measurable background noise. Employing the same trap depth of 50 μK used in the classical light storage shown in Fig. 11(a), (determined by the need to maintain sufficient retrieval efficiency) we note a ten-fold increase in the measured quantum memory time, from 9.5 ms to 95 ms upon application of the compensation field, Fig. 11(b). We note that both of these lifetimes are shorter than corresponding

values found with classical light. This can be attributed to a combination of a 10% uncertainty in the day-to-day trap depth calibration and an inferred difference in the mode structure of the retrieved excitations. The measured retrieval efficiencies are considerably higher than in Ref. [44] as a much tighter optical lattice is employed here.

Nonclassical behaviour of the memory and the signal field can be characterized by performing joint photoelectric detection measurements on the signal and retrieved idler fields. Specifically, we measure the α-parameter of Grangier *et al.* [60]. The protocol involves a sequence of trials, each trial begins with a *write* pulse and terminates with a *clean* pulse which resets the atomic state, until the signal detector, D1, registers a photoelectric detection event. At this point, the sequence is terminated, and the prepared spin wave is stored for the time T_s, after which time a *read* pulse converts the excitation into an idler field, which is directed onto a beamsplitter followed by photodetectors D2 and D3 (Fig. 10).

The *measured* retrieval efficiency η refers to photoelectric detection probabilities per *read* pulse, determined by the sum of probabilities $p_2 + p_3$ to detect photoelectric events at D2 and D3, respectively. The measured passive losses from the atomic sample to the detector in the idler channel produce an efficiency factor of $0.25 \pm 10\%$. *Intrinsic* efficiencies η_{int} and ϵ_{int} are therefore greater than η and ϵ by a factor of 4, respectively, as shown in Table 4. The uncertainties given are based on the statistics of photoelectron counting events. We have verified that all the measured idler efficiencies are independent of p_1, so that they have negligible background contributions.

α is determined from the measured set of joint photoelectric detection probabilities on the three detectors, D1-3, Fig. 10. The value $\alpha = 1$ delineates regimes of classical (uncorrelated) ($\alpha \geq 1$) and quantum ($0 \leq \alpha < 1$) electromagnetic fields. The limiting case, $\alpha = 0$, implies perfect pairwise signal field-memory correlations such as the weakly excited two-mode squeezed vacuum state [71], or the single-photon state of the

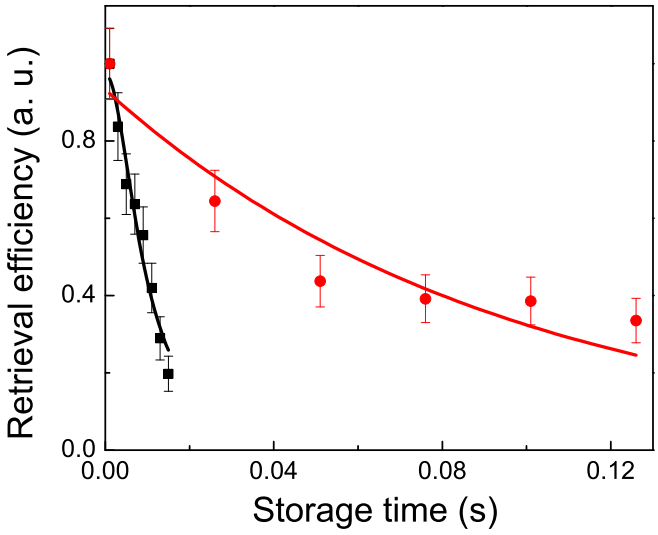

Figure 12: Efficiencies for single photon retrieval as a function of the storage period (T). The solid lines are fits of the form e^{-T/T_c} for lattice with compensation, and $(1+(T/Tc)^2)^{-3/2}$ without one. At the trap depth of 48 μK the lifetime T_c increases from 9 ms without compensation (squares) to 95 ms with compensation (circles), giving intrinsic retrieval efficiencies, for zero storage time, $\eta_{int} = 23\%$ and $\eta_{int} = 16\%$, respectively. The efficiencies are largely limited by spatial matching of the signal/idler mode with the lattice-confined atomic cloud. Error bars represent ± 1 standard deviation based on photoelectron counting statistics.

idler field conditioned upon a detection event at D1. The results after storage periods of 60 and 100 ms are shown in Table 4, along with the corresponding measured and intrinsic (normalized by optical losses) retrieval efficiencies. This may be compared with the longest previously measured quantum memory lifetime of 6 ms; that is the longest storage time a non-classical value of α has been measured [44].

3.2 Magnetic compensation

3.2.1 Introduction

The previous section describes how laser induced compensation was used to achieve light storage and retrieval in a 1-D optical lattice for lifetime of ~ 0.2 seconds [6].

Table 4: Measured values of α (see text), measured efficiency η and intrinsic efficiency η_{int}. Error bars represent ± 1 standard deviation based on photoelectron counting statistics, calculated from the mean values divided by the square root of the number of triple coincidences measured with detectors D1, D2 and D3.

T, ms	α	η	η_{int}
60	0.00 ± 0.07	1.9%	7%
100	0.18 ± 0.12	1.2%	5%

This section presents the first measurements of increased clock coherence times using the magic magnetic field technique for light shift compensation, proposed and spectroscopically demonstrated in Ref. [29]. We achieve coherent light storage and retrieval in the atomic sample of $\sim 10^7$ rubidium atoms confined in a 1-D optical lattice at a temperature of ~ 10 μK, with lifetime of 0.32 seconds, bettering previous results achieved via laser compensation [6] and in a shallow-lattice Mott insulator [25] by about 30%. The storage and retrieval efficiency of 3.4% (at a near-zero storage time of 1 ms) is comparable to that of Ref. [6], but is more than an order of magnitude higher than in the Mott insulator work [25]. We also observe long storage times, albeit with ten times lower efficiency, employing the $|F = 2, m = \pm 1\rangle \leftrightarrow |F = 1, -m\rangle$ hyperfine coherences (we will employ the shorthand $\pm 1/\mp 1$). By comparing results for the three distinct coherences, we establish residual magnetic sensitivity of the approach as a major limiting factor on the observed storage lifetimes, and identify differential vector and rank-2 tensor ac Stark contributions to the measured magnetic field values, and discuss the physical mechanisms that give rise to these different contributions.

3.2.2 Magic magnetic field

The ac-Stark shift can be described by an operator $U = \sum_{L=0,1,2} U^{[L]}$, with scalar, vector and (rank-2) tensor parts each proportional to the light intensity. In a circularly polarized lattice with the magnetic field directed along the propagation/quantization

direction, both the Zeeman interaction H^Z and U couple only hyperfine states with the same m. Since the ground level hyperfine splitting is large compared to H_Z and U, we may compute the level shifts using degenerate perturbation theory, giving, for $m = \pm 1$, the differential shift $\hbar\delta_m$ associated with the energy difference between the states $|F = 2, m = \pm 1\rangle$ and $|F = 1, -m\rangle$:

$$\begin{aligned}\hbar\delta_m \quad &\simeq \langle 2m|H_Z + U^{[0]} + U^{[1]} + U^{[2]}|2m\rangle - \\ &\langle 1-m|H_Z + U^{[0]} + U^{[1]} + U^{[2]}|1-m\rangle + \\ &\frac{\langle 2m|H^Z + U^{[1]}|1m\rangle\langle 1m|H^Z + U^{[1]}|2m\rangle}{\hbar\Delta^g_{hfs}} + \\ &\frac{\langle 1-m|H^Z + U^{[1]}|2-m\rangle\langle 2-m|H^Z + U^{[1]}|1-m\rangle}{\hbar\Delta^g_{hfs}},\end{aligned}$$

where we have ignored the small tensor contribution in the second-order term, and used the fact that the scalar shift does not couple the $F = 1$ and 2 states by symmetry.

Suppressing the term linear in light intensity largely removes the dephasing due to the optical lattice. This occurs at the field value

$$\mu B_0^{(\pm)} = \frac{4}{3}\frac{\hbar\Delta}{4\alpha_{12}^{[1]}}\big[\sqrt{\frac{5}{3}}(\alpha_2^{[0]} - \alpha_1^{[0]}) \pm \frac{\sqrt{5}}{2}(\alpha_1^{[1]} + \frac{1}{\sqrt{3}}\alpha_2^{[1]}) - \frac{1}{2}\sqrt{\frac{5}{21}}(\alpha_2^{[2]} + \sqrt{\frac{7}{5}}\alpha_1^{[2]})\big]. \quad (8)$$

A similar calculation for the clock coherence results in the corresponding field value

$$\mu B_0^{(0)} = \frac{\hbar\Delta}{4\alpha_{12}^{[1]}}\big[\sqrt{\frac{5}{3}}(\alpha_2^{[0]} - \alpha_1^{[0]}) - \sqrt{\frac{5}{21}}(\alpha_2^{[2]} - \sqrt{\frac{7}{5}}\alpha_1^{[2]})\big]. \quad (9)$$

The diagonal tensor polarizabilities $\alpha_F^{[p]}$ for $F = 1, 2$ correspond to α_p of Ref. [72] in which the ground-state energy is that of the hyperfine level F, whereas $\alpha_{12}^{[p]}$ is an off-diagonal generalization associated with the Stark coupling between the hyperfine ground levels and is similar to that discussed in Ref. [73]. In Eqs. 1 and 2 the scalar contribution dominates the measured magnetic field values. However, suitable combinations of the latter enable us to extract the vector and rank-2 tensor contributions, as discussed later.

3.2.3 Experiment

We load ^{87}Rb atoms into a magneto-optical trap (MOT) from a background vapor. After compression and precooling the sample is transferred to a one dimensional optical lattice resulting in an approximately cigar shaped cloud of $\sim 10^7$ atoms with $1/e^2$ waists of 130 μm and 840 μm, respectively. The lattice is formed by interfering two circularly polarized 1063.8 nm (in vacuum) beams intersecting at an angle of 9.6° in the horizontal plane. The beams have waists of ~ 200 μm and their total power is varied between 8 W and 14.6 W.

The probe and control fields are tuned to corresponding D_1-resonance lines $|a\rangle \leftrightarrow |c\rangle$ and $|b\rangle \leftrightarrow |c\rangle$, respectively, where $\{|a,b\rangle\}$ correspond to $\{5S_{1/2}, F = 2, 1\}$ and $\{|c\rangle\}$ represents $\{5P_{1/2}, F = 2\}$. The probe and control beams co-propagate at a small angle of 0.9°, and are positioned in the horizontal plane symmetrically with respect to the lattice and magnetic field direction, cf Refs.[44, 69]. The beam waists are 110 and 270 μm, respectively. The non-zero angle results in a phase grating imprinted on the atoms whose spatial profile is preserved by the lattice.

Three different polarization configurations of the probe and control fields are employed, each corresponding to excitation of a different long-lived hyperfine coherence: lin$\perp$lin for clock coherence, $\sigma^{\pm}/\sigma^{\mp}$ for $\mp 1/\pm 1$ coherences. After loading, a bias magnetic field is applied along the major axis of the trap and atoms are either prepared in the $5^2S_{1/2}, F = 1, m = 0$ state by means of optical pumping when clock coherence is addressed, or left unpolarized when $\pm 1/\mp 1$ coherences are used.

The probe pulse is adiabatically converted into the respective spin wave that is first-order insensitive to ambient magnetic fields. The probe field has a full width at half maximum (fwhm) of 60 ns and peak power of 10 nW. The control field, also used for retrieval, has fwhm of 330 ns and peak power 90 μW. After a given storage period the control field retrieves a signal on the probe transition. The latter is coupled to a single mode fiber and directed onto an avalanche photo-detector, the voltage output

of which is digitized and recorded. We measure the retrieval efficiency, defined as the ratio of the energies of the retrieved and incident probe pulses after a given storage time. Magnetic field strength is calibrated by measurements of the Larmor precession frequencies of the stored spin-waves in an unpolarized sample of atoms (no optical pumping) [50, 49]. The lattice is linearly polarized during the calibration to exclude the contribution of vector lattice light shift to the Larmor frequency.

3.2.4 Measurements of magic field values and lifetimes

In order to determine B_0, we maximize the retrieved pulse energy while tuning the magnetic field strength, as shown in Fig. 13. The data are fitted with the function $\exp(-\gamma(B - B_0)^2)$, γ being an adjustable parameter, resulting in $B_0^{(0)}$=4.24(1) G, $B_0^{(+)}$=5.42(1) G, and $B_0^{(-)}$=5.99(2) G, respectively, where the 0.01 G uncertainty is the combined statistical and field calibration error.

Accounting for the measured degree of circular polarization $A = 0.991(2)$ of the lattice beams [73][1] , the value of the magnetic field in an ideal circularly-polarized lattice collinear with the magnetic field would be $B_0^{(0)}$=4.20(1) G, while Ref. [73] predicts the value of $B_0^{(0)} = 4.38$ G, for our 1063.8 nm lattice. The disagreement deserves further investigation.

The similarly corrected values of $B_0^{(+)}$ and $B_0^{(-)}$, for perfect circular polarizations, would be 5.37(1) G and 5.93(2) G, respectively. Their (normalized) difference $2[B_0^{(-)} - B_0^{(+)}]/[B_0^{(-)} + B_0^{(+)}] = 0.099(3)$ is proportional to the differential vector shift, see Eq.(1) and is consistent with an estimated value of 0.11 when only the 5S and 5P levels are included in the calculation of the ac Stark shifts. A non-zero value of the quantity $[(3/8)(B_0^{(-)} + B_0^{(+)}) - B_0^{(0)}]/B_0^{(0)} = 0.008(3)$ reveals ac Stark shifts associated with the rank-2 tensor, and is consistent with the value of 0.009 estimated by considering only the 5S and 5P levels.

[1]Parameter $A \equiv \sqrt{1-\epsilon^2}$, where ellipticity ϵ is defined as in Ref. [74]

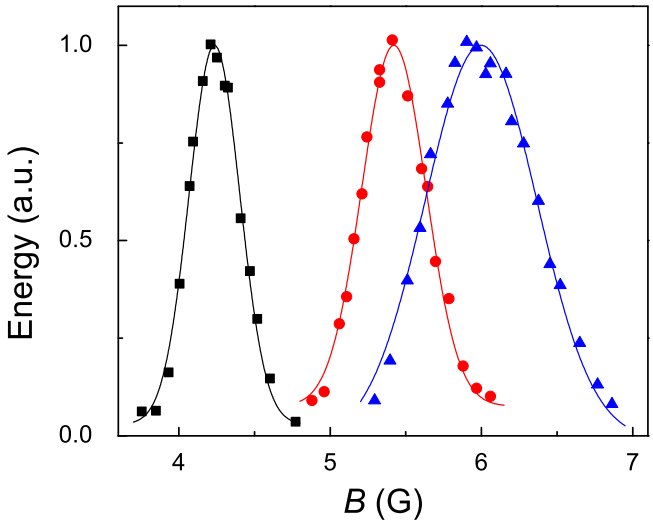

Figure 13: Retrieved pulse energy as a function of the magnetic field, for 64 μK deep lattice. Squares, for lin$\perp$lin polarizations and $m = 0$ optically pumped sample, circles and triangles for the $\sigma^{\pm}/\sigma^{\mp}$ polarizations, unpolarized sample. Light is stored and retrieved after 0.5, 0.3 and 0.2 s, respectively. Solid curves are Gaussian fits, see text.

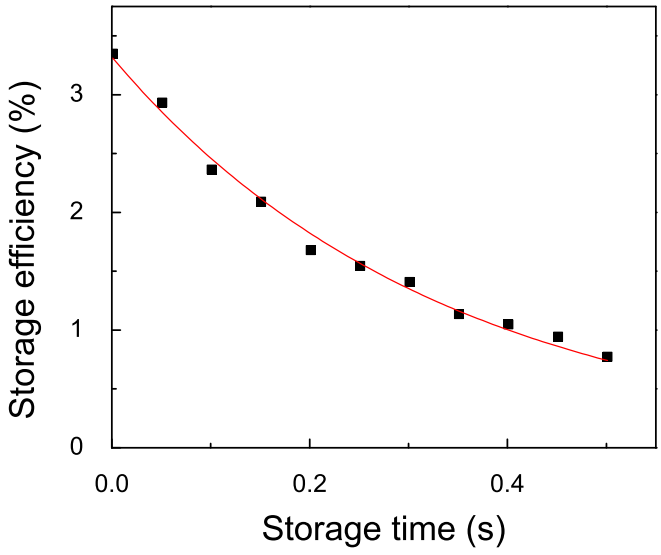

Figure 14: Retrieval efficiency vs storage time in a 48 μK deep lattice at $B = 4.2$ G. An exponential fit provides lifetime of 0.32(1) second. See text for details.

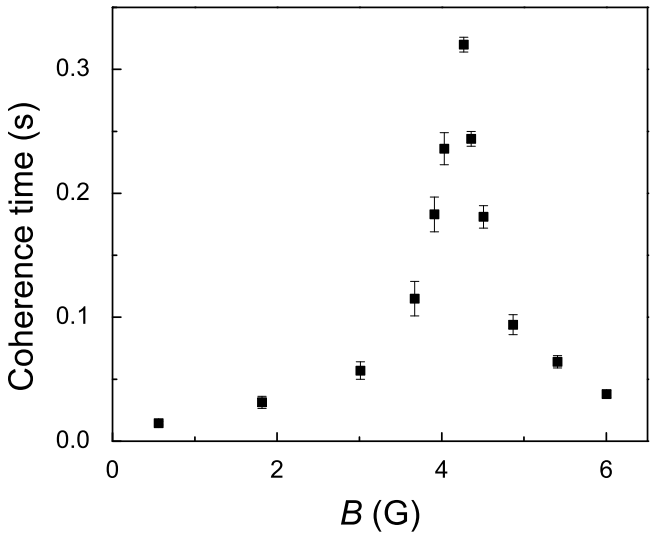

Figure 15: 1/e lifetime determined via the storage and retrieval protocol as a function of the magnetic field in a 64 μK deep lattice.

The decay of the retrieved signal is well described by an exponential function of storage time, Fig. 14. The 1/e storage lifetimes τ versus applied magnetic field data are shown in Fig. 15. No significant change in lifetime is observed when the lattice trap depth is varied, as shown in Fig. 16. The other lifetimes were $\tau_+ = 0.43(2)$ s and $\tau_- = 0.10(1)$ s. These can be explained by a combination of the 1 s lifetime of the atoms in the lattice and of the concomitant effective magnetic moments μ', of the coherences, $\mu' \equiv dE/dB$. The lifetime of a coherence τ in a gradient of the ambient magnetic field B' is expected to be inversely proportional to μ': $\tau^{-1} = 2\pi\mu' B' l$, where l is the length of the atomic sample, e.g., see Methods section of Ref. [44]. After excluding the atomic loss contribution to the measured storage lifetime via $1/\tau_{c,\pm} = 1\tau^m_{c,\pm} + 1/T$, the residual lifetime $\tau^m_{c,\pm} \equiv T\tau_{c,\pm}/(T - \tau_{c,\pm})$ is displayed in Fig. 17.

In conclusion, we have achieved a combination of high efficiency and exceptionally long storage time for coherent light pulses in an ac Stark compensated optical

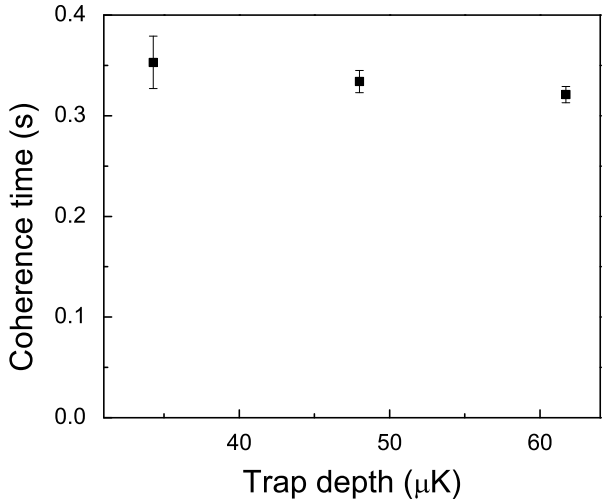

Figure 16: The 1/e lifetime of light storage and retrieval protocol vs trap depth. Memory lifetime is no longer limited by Stark shifts but magnetic decoherence of the clock states and atomic losses.

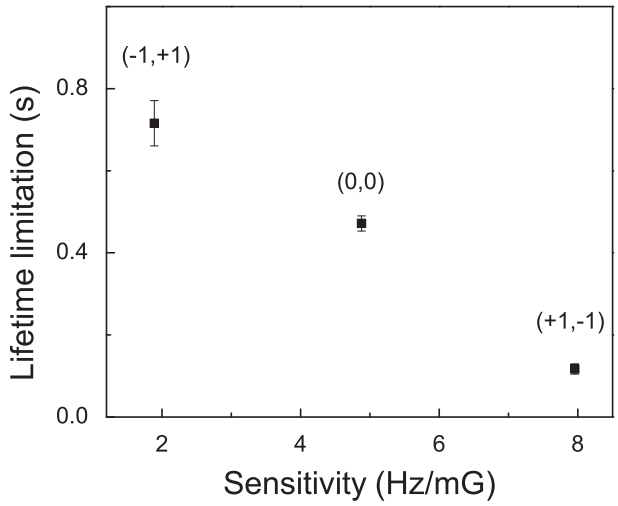

Figure 17: $T\tau_{c,\pm}/(T-\tau_{c,\pm})$ as a function of the effective magnetic field moment $\mu' \equiv dE/dB$, for the three long-lived coherences, each at its respective magic field value $B_0^{\pm,c}$, in a 64 μK deep trap.

lattice. The measured value of the magic magnetic field $B_0 = 4.20(1)$ G for the clock coherence disagrees with the theoretically predicted value of 4.38 G [73]. We measure long light storage lifetimes at field values 5.37(1) G and 5.93(2) G for the $\pm 1/\mp 1$ coherences, revealing small differential vector and rank-2 tensor light shifts. The measured lifetimes of light storage for the three coherences, of 0.32 s, 0.43 s, and 0.1 s, respectively, are consistent with dephasing in an ambient magnetic field. Similar lifetimes for singly-excited spin waves are demonstrated in the next chapter using this technique.

3.3 Telecom wavelength interface

3.3.1 Introduction

Future quantum information processing systems will rely on the ability to generate, distribute and control elementary entanglement processes across continental distances. Besides offering fundamentally more secure ways to communicate, quantum networks may provide the structure for distributed quantum computation. Large-scale quantum networks necessarily require mitigation of exponential photon transmission losses, by using compatible quantum memory elements. Compatibility involves storing and retrieving quantum information and transmitting the latter optically, in the case of fiber-based networks, in the telecom wavelength range where absorption is minimized [48]. Unfortunately, typical atomic ground-state electronic transitions suitable for quantum information applications lie outside the telecom window [42, 75, 3, 44, 76, 54, 77, 52, 78, 79]. The entanglement distribution rate of a network also depends critically on the quantum memory lifetime of the storage elements; memory lifetimes of a second or longer may be desirable [18, 19, 20, 21, 22]. The combined attributes of telecom wavelength light and a long-lived quantum memory are therefore essential for fiber-based quantum networks [48]. We demonstrated quantum correlations of a long-lived memory described in the previous chapter with a

telecom field for 11 ms storage time in Ref. [6]. Two-photon Stark shift compensation was used to achieve long (~ 0.1 s) memory lifetime.

In this chapter I present measurements of entanglement between an atomic spin-wave memory qubit and a telecom field qubit, at a storage time of 10 ms. As in Ref. [6], high-efficiency, low-noise wavelength conversion between NIR and telecom fields in an optically-thick, cold Rb gas is at the core of our experimental protocol. The memory qubit employs two spatially distinct spin-waves, both based on the $m = 0 \leftrightarrow 0$ clock transition between hyperfine ground levels. The qubit spin-wave, pinned by an optical lattice to reduce motional dephasing, is lifetime-enhanced by mixing the clock states using a bias magnetic field to offset inhomogeneous, differential ac-Stark shifts [29, 68]. Our Bell inequality violation measurements indicate the memory qubit is entangled with the NIR qubit for as long as 0.1 s, a 30-fold improvement on the results of Ref. [69].

3.3.2 Memory qubit

I now describe a light-shift-compensated memory qubit, shown in the left panel of Fig. 18. A magneto-optical trap (MOT) captures ^{87}Rb atoms from a background vapor. After compression and cooling the atoms are transferred to a one dimensional optical lattice formed by interfering two circularly polarized 1064 nm beams intersecting at an angle of 9.6° in the horizontal plane (a 6.3 μm lattice period). The waists of the lattice beams are ≈ 0.2 mm and their total power is typically 12 W. Trap depth $U_0 = 56$ μK, trap frequencies $(\omega_x/(2\pi), \omega_y/(2\pi), \omega_z/(2\pi)) = (8100,116,10)$ Hz. The cigar shaped atomic cloud has $1/e^2$ waists of 0.15 mm and 1 mm, respectively, and contains about 10^7 atoms. After loading, the atoms are prepared in the $|+\rangle \equiv |5^2S_{1/2}, F = 2, m = 0\rangle$ state by means of optical pumping. The magnetic field is set to the "magic" value (4.2 G for our 1064 nm wavelength lattice [68]) to equalize the ac-Stark shifts of the clock states.

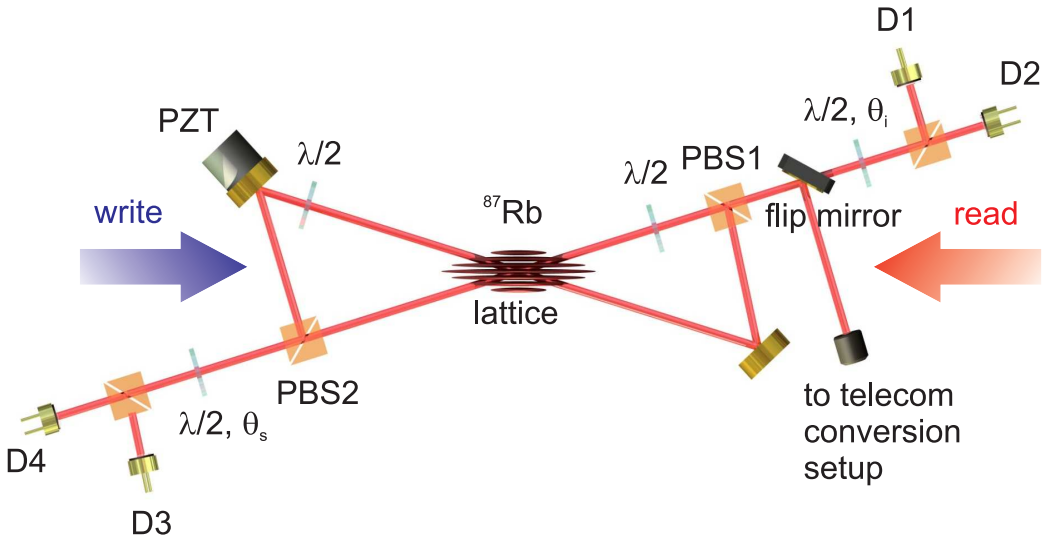

Figure 18: Stark shift compensated memory qubit. A write laser generates spin-waves in atomic ^{87}Rb, confined in a 1-D lattice with magnetically-compensated clock transition light shifts. The experimental protocol is based on a sequence of write/clean pulses, terminated by photodetection of the signal field at D1 or D2 [2, 3]. After a storage period, the stored spin-wave qubit is converted by the read laser to idler field qubit and polarization measurement of the latter is performed.

Raman scattering of a weak linearly polarized *write* laser field (270 μm mode waist) transfers a fraction of atomic population into the $|-\rangle \equiv |5^2S_{1/2}, F = 1, m = 0\rangle$ clock state generating a signal field offset in frequency from the *write* field by 6.8 GHz, the ^{87}Rb ground-level hyperfine splitting. The memory qubit is based on two spatially distinct spin-waves [42, 76]. The interferometric arrangement for the associated signal and idler field modes is shown in Fig. 18. Two Gaussian modes of the signal field centered at angles $\pm 0.9^\circ$ to the *write* field wave-vector $\mathbf{k_w}$ direction are combined on a polarizing beamsplitter (PBS1), and directed to either the polarization measurement setup involving detectors D1 and D2 for spin-wave memory/NIR field entanglement analysis, or, via an optical fiber, to the wavelength conversion setup to generate memory/telecom field entanglement. The interferometric path length difference is stabilized so that the signal-idler polarization state at the output of PBS1 and PBS2 has the form $\propto (|H\rangle_s|H\rangle_i + |V\rangle_s|V\rangle_i)$. An auxiliary laser at 766 nm (not shown), intensity-stabilized and frequency-locked to the potassium D_2 line, is used for that purpose. The signal field photoelectric detection probability per experimental trial is in the range $10^{-4}-10^{-3}$ and can be varied by adjusting the *write* field power/detuning.

The detection of the signal photon implies a momentum change $\hbar(\mathbf{k_w} - \mathbf{k_s})$ of the atoms, where $\mathbf{k_s}$ is the signal field wavevector. An atom at position $\mathbf{r}_\mu$ contributes to the spin-wave excitation with a phase factor $e^{-i(\mathbf{k_w}-\mathbf{k_s})\cdot\mathbf{r}_\mu}$; the atom experiences additional phase modulation due to the local value of the differential ac-Stark shift. The collective atomic excitation, imprinted with this phase grating, is the *write* spin wave. The spin wave coherence is essential for efficient coupling to a single spatial electromagnetic field mode in the memory retrieval stage.

The retrieval, or *read* process, is performed after a defined storage period. A *read* field pulse converts the stored spin-wave excitations into an idler field by Raman scattering, Fig. 18. The idler emission is collected in the two Gaussian spatial modes of the detected signal field, but with opposite propagation directions ($\mathbf{k_i} \approx -\mathbf{k_s}$). The

two idler modes are combined on a polarization beamsplitter (PBS2) and directed to detectors D3 and D4 for polarization analysis.

We have previously observed quantum memory lifetime (1/e) of 0.3 s for a single spin-wave aligned such that the vector $\mathbf{k_w} - \mathbf{k_s}$ is directed along the axis of our 1-D lattice [68]. In the arrangement shown in Fig. 18, the vectors $\mathbf{k_w} - \mathbf{k_{s_j}}$ for each of the two qubit spin-waves, $j = 1, 2$, are at angles $\phi \approx \pm 0.5^\circ$ to the lattice axis (x-axis). We have measured the efficiency of light storage and retrieval as a function of storage time to characterize the coherence properties of the two spin waves. Storage of a classical field is achieved by counterpropagating the light in the signal field fiber, while the *read* light is used in the role of control field. In this geometry the stored spin waves are of the same 50 μm period and have a similar spatial envelope as the single excitations created via the DLCZ protocol. The spin-wave period is much longer than that of the lattice, resulting in strong suppression of motional dephasing. We observe that the storage lifetime is rather sensitive to the alignment of the control and signal fields relative to the optical lattice and to the size of the lattice beams. Even when the interferometer is optimally aligned, the observed storage lifetime of ≈ 0.2 s is shorter than the ≈ 0.3 s reported in Ref. [68]. The time-dependence of the retrieval efficiency exhibits deviations from the near exponential decay observed in Ref. [68]. We attribute these observations to atomic motion along the z-axis, which, due to the non-zero value of ϕ, partially dephases the spin-wave coherence.

3.3.3 Quantum correlations with memory qubit

The polarization states of both the signal and idler fields are measured using a polarizing beam splitter and two single photon detectors, D1, D2 for the signal and D3, D4 for the idler (additional technical details are given in Ref. [69]). We denote the joint signal-idler detection rates between detector Dn, $n = 1, 2$ and detector Dm, $m = 3, 4$ by $C_{nm}(\theta_s, \theta_i)$. Here θ_s and θ_i are the angles through which the polarization

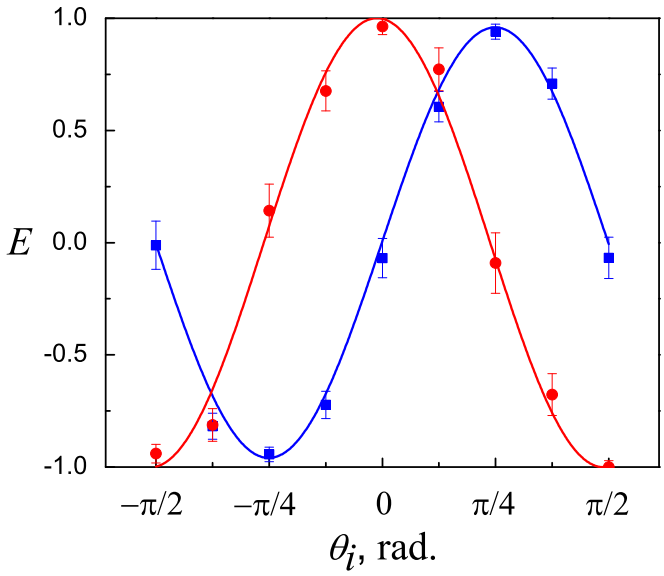

Figure 19: Measured values of the correlation function $E(\theta_s, \theta_i)$ as a function of θ_i for 1 ms storage. Circles are for $\theta_s = 0$, squares are for $\theta_s = \pi/4$. The curves are sinusoidal fits to the data.

is rotated by the respective half-waveplates. The rates $C_{ij}\,(\theta_s, \theta_i)$, $i = 1, 2, j = 3, 4$ exhibit sinusoidal variations as a function of the waveplates' orientations. In order to account for unequal efficiencies of the detectors (D1, D2) and (D3, D4), each correlation measurement includes flipping the polarization of both signal and idler fields by $\pi/2$ within the data set. We check for Bell's inequality violation $|S| \leq 2$ by measuring polarization correlations between signal and idler fields at certain canonical angles, where $S = E(\pi/4, \pi/8) + E(0, \pi/8) + E(0, -\pi/8) - E(\pi/4, -\pi/8)$; here the correlation function $E(\theta_s, \theta_i)$ is given by [65, 66]

$$\frac{C_{13}(\theta_s, \theta_i) + C_{24}(\theta_s, \theta_i) - C_{14}(\theta_s, \theta_i) - C_{23}(\theta_s, \theta_i)}{C_{13}(\theta_s, \theta_i) + C_{24}(\theta_s, \theta_i) + C_{14}(\theta_s, \theta_i) + C_{23}(\theta_s, \theta_i)}.$$

The measured sinusoidal variation of $E(\theta_s, \theta_i)$ as a function of θ_i for fixed θ_s is shown in Fig. 19. In Table 5 we list the values of E and the Bell parameter S for two values of storage time: 1 ms and 0.1 s. The measured idler photodetection probabilities for the data in Table 5 are 1.7% at 0.1 s and 4% at 1 ms. Normalized by

the passive transmission and detection losses (0.25), the intrinsic atomic excitation retrieval efficiency after 0.1 s storage is 7% (16% at 1 ms). We observe different behavior of the retrieval efficiencies as a function of storage time for coherent light and the DLCZ protocol. This could be caused by differences in the spatial mode structure of the retrieved excitations, as we have observed previously [6].

3.3.4 Telecom-memory entanglement

To convert the signal photons produced by the *write* process into light of telecom wavelength we employ the diamond configuration of atomic levels shown in the inset to Fig. 20 [48, 80, 81]. A cigar-shaped ($\varnothing$ ∼2 mm, L ∼6 mm) sample of ^{87}Rb gas is prepared, in level $|a\rangle$ with optical depth ∼ 150, in an extended dark magneto-optical trap (EDMOT). Additional details are given in Ref. [6].

A polarizing beamsplitter separates the H- and V- components of the signal field and the latter is delayed by an optical fiber (step 1). In step 2, the write signal and pump fields generate the telecom signal ($e \rightarrow d$ transition), which is directed through a 100 m standard telecommunication fiber back to the atomic sample. In step 3 the telecom signal is upconverted to NIR signal ($a \leftrightarrow c$ transition). After its two polarization components are temporally overlapped (step 4) using the same interferometric arrangement used to separate the incoming NIR signal, a polarization measurement is performed. High-efficiency detection is achieved by the Si single photon detectors, D1′ and D2′. The inset shows the Λ-type atomic levels used for the DLCZ scheme (left) and the cascade configurations used for wavelength conversion (right): $|a\rangle = |5S_{1/2}\ F = 1\rangle$, $|b\rangle = |5S_{1/2}\ F = 2\rangle$, $|c\rangle = |5P_{1/2}\ F = 2\rangle$, $|d\rangle = |5P_{3/2}\ F = 2\rangle$, $|e\rangle = |6S_{1/2}\ F = 1\rangle$, $\Delta_{\rm s} = -2\pi \times 17$ MHz, $\Delta_{\rm I} = 2\pi \times 41$ MHz, $\Delta_{\rm II} = 2\pi \times 6$ MHz.

We have previously demonstrated high- efficiency, low-noise telecom wavelength conversion for single-photon light fields [6]. However, the high (up to 65%) efficiency of frequency conversion is only observed for light that is copolarized with the telecom

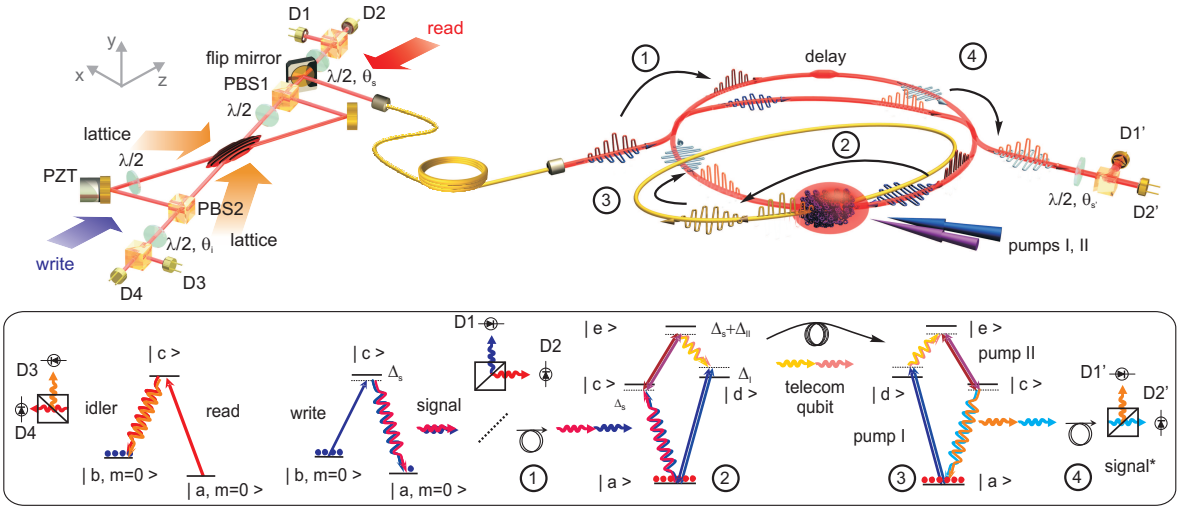

Figure 20: Joint experimental setup and temporal sequence of experiment (steps 1 through 4, see text for details).

Table 5: Measured correlation function $E(\theta_s, \theta_i)$ and S for 1 ms and 100 ms storage time. These are based on 582 events and 1001 events, respectively.

		$E(\theta_s, \theta_i)$	
θ_s	θ_i	1 ms	0.1 s
$\pi/4$	$-\pi/8$	-0.78 ± 0.05	-0.65 ± 0.05
$\pi/4$	$\pi/8$	0.71 ± 0.07	0.67 ± 0.05
0	$-\pi/8$	0.75 ± 0.05	0.66 ± 0.05
0	$\pi/8$	0.66 ± 0.06	0.68 ± 0.05
		$S = 2.90 \pm 0.12$	$S = 2.66 \pm 0.09$

pump. The orthogonal polarization component of the signal field is largely absorbed in the atomic gas. Here we achieve polarization-stable wavelength conversion by splitting the two polarization components of the optical field and delaying the (vertically polarized) V-component by 235 ns (Fig. 20). By switching the polarization of both pump fields to orthogonal settings while the V-component interacts with the atoms we achieve high transparency and high (54%) conversion efficiency for both (horizontally polarized) H- and V- components. The conversion efficiency is lower than the 65% observed for a single polarization component, as a result of the limited power available for pump II and the denser atomic sample used to compensate for

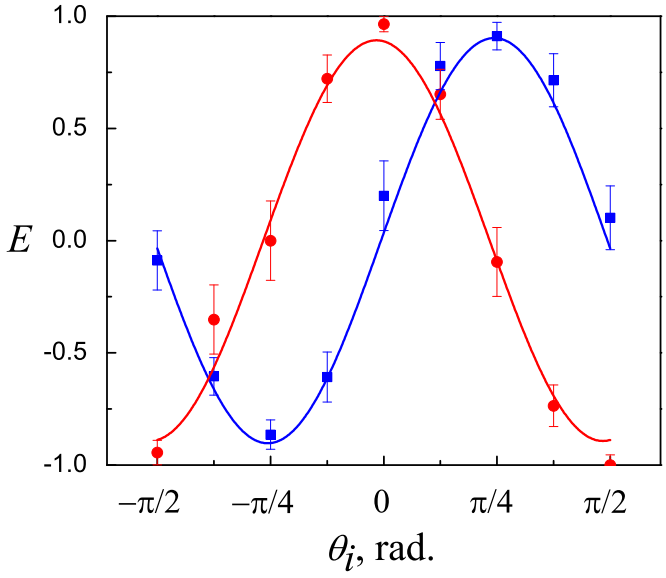

Figure 21: Measured correlation function $E(\theta_s, \theta_i)$ when 795 nm signal field is first converted to telecom wavelength, passed through 100 m telecom fiber, and converted back to 795 nm field, for 1 μs storage. Circles are for $\theta_s = 0$, squares are for $\theta_s = \pi/4$.The curves are sinusoidal fits to the data.

the undesirable effects of hyperfine optical pumping.

The level of dark counts of commercially available InGaAs/InP single photon detectors for telecom wavelengths is too high for our purposes. Instead, we employ a reverse wavelength conversion sequence, from 1367 nm to 795 nm, Fig. 20. The H- and V- components of the regenerated NIR signal field are subsequently recombined. A half-wave plate, a polarizing beam splitter and two Si single photon detectors D1′ and D2′ complete the measurement of the polarization state of the telecom signal field qubit. The combined transmission measured for the NIR signal qubit from the input of the signal field fiber to detectors D1′ and D2′ is 7.5(5)%, with a factor 0.25 contribution from passive optical elements and fiber coupling losses (0.8 for both telecom and NIR fields). The interferometric configuration for the signal field sketched in the right panel of Fig. 20 is designed to cancel out phase fluctuations occurring

Table 6: Measured correlation function $E(\theta_s, \theta_i)$ and S when 795 nm signal field is first converted to telecom wavelength, passed through 100 m telecom fiber, and converted back to 795 nm field. Storage times are 1 μs and 10 ms, based on 986 and 667 events, respectively.

		$E(\theta_s, \theta_i)$	
θ_s	θ_i	1 μs	10 ms
$\pi/4$	$-\pi/8$	-0.54 ± 0.05	-0.61 ± 0.06
$\pi/4$	$\pi/8$	0.65 ± 0.05	0.72 ± 0.06
0	$-\pi/8$	0.78 ± 0.04	0.75 ± 0.05
0	$\pi/8$	0.58 ± 0.05	0.56 ± 0.07
		$S = 2.55 \pm 0.10$	$S = 2.64 \pm 0.12$

on a time scale slower than 1 μs, so that active stabilization of the interferometer is not required. The ellipticity of the signal field, acquired due to birefringence of the optical fibers, is removed by adjusting the phase difference between the H- and V- components of the pump II pulses employed for the upconversion. With coherent light input the polarization state is preserved after transmission and conversion with a power contrast of greater than 100 to 1. We have not observed a noticeable drift of the polarization fringes on a timescale of two days, for either coherent laser or signal field inputs to the wavelength conversion set-up.

The measured sinusoidal variation of $E(\theta_s, \theta_i)$ as a function of θ_i for fixed θ_s is shown in Fig. 21, for a short period of 1 μs. In Table 6 we give the measured values of E and the Bell parameter S for 1 μs and for 10 ms storage; longer storage times were not employed due to the prohibitively long data acquisition time required. The measured idler photodetection probabilities for the data in Table 6 are 5% at 1 μs and 2.8% at 10 ms. The data was taken with larger lattice beams (0.26 mm waist size instead of 0.2 mm for the data without wavelength conversion) resulting in a revival behavior of the retrieval efficiency in the 30-100 ms region; we attribute this to atomic motion along the long axis of the trap.

In summary, we have confirmed preservation of memory/light entanglement through

two stages of telecom wavelength conversion, for 10 ms storage. We have also observed entanglement of a spin-wave produced in a 1-D optical lattice and a NIR light field for a 0.1 s storage time. The storage time is limited by atom motion along the principal trap axis, and could be further increased by confining atoms in 2-D or 3-D lattice geometries.

3.4 Light storage on the scale of a minute

To overcome the limitations of the memory lifetime due to trap losses resulting from collisions with room-temperature background atoms we have constructed a differentially pumped vacuum system. The new setup consists of a $2D^+$-MOT based cold atom source and a science chamber with a pressure in the range of $\sim 10^{-11}$ Torr (details are given in the Appendix B). This section describes an experiment in which we achieved a 16 s $1/e$ lifetime of coherent light pulses stored in a Stark-shift compensated optical lattice. The extended lifetime was observed after applying a refocusing microwave pulse sequence on the clock transition used for storage.

3.4.1 Experimental setup

The essential elements of the experimental setup are shown in Fig. 22. A cigar-shaped optically dense sample of cold ^{87}Rb atoms is prepared in an optical lattice. Atomic number loss is a major limitation on the lifetime of light storage using atoms confined in an optical lattice [68]. In this work we use a double chamber system to achieve efficient cooling and loading of atoms into the lattice while keeping the vacuum pressure at a $\sim 10^{-11}$ Torr level. After the loading the sample of $\sim 10^7$ atoms is trapped in the lattice. The cloud has longitudinal and transverse waists of 260 and 70 μm, respectively. To avoid collisional losses the atoms are optically pumped into the lower hyperfine level $(5S_{1/2}, F = 1)$ right after the loading. In the first 5 seconds, the atoms undergo a fast two-body collisional decay. After evaporation, the atom number undergoes one-body decay due to collisions with the background atoms,

giving a lifetime of 169(14) seconds. It is the longest for rubidium atoms in an optical dipole trap to our knowledge.

The relevant atomic levels are shown in the inset to Fig. 22: $|a\rangle \equiv |5S_{1/2}, F = 1\rangle$, $|b\rangle \equiv |5S_{1/2}, F = 2\rangle$, and $|c\rangle \equiv |5P_{1/2}, F = 1\rangle$. The probe Ω_p and control Ω_c fields are resonant with the corresponding transitions, $|a\rangle \leftrightarrow |c\rangle$ and $|b\rangle \leftrightarrow |c\rangle$. The probe and control beams propagate in the horizontal plane approximately along the magnetic field direction, intersecting at the center of the atomic sample at an angle 1.3°. The beam waists are 50 and 200 μm, respectively. The probe field has a fwhm of 82 ns and a peak power of 130 nW. The control field has a fwhm of 1040 ns and a peak power of 160 μW.

3.4.2 Measurements of magic field values and light-storage lifetimes

Magic magnetic field is used here for light-shift compensation similarly to the experiments described earlier in this chapter. To determine the magic values, we measure the retrieved pulse energy with a different magnetic field value, Fig. 23(a) (inset). We use a Ramsey sequence of two $\pi/2$-pulses to measure the quadratic magnetic shift of the clock transition to calibrate the value of the magnetic field. The decay of the retrieved signal with storage time for the three coherences is shown in Fig. 23(b), with the data fit by exponential functions with $1/e$ lifetimes of 4.8(1), 2.5(1), and 6.9(4) s for the (0,0), (1,-1), and (-1,1) coherences, respectively. The longer lifetimes observed for the coherences (Fig. 23(a)) with lower effective magnetic moments μ' ($\mu' \equiv dE/dB$, where E is the energy of the corresponding hyperfine transition) are indicative of residual decoherence caused by gradients or fluctuations of external magnetic fields.

3.4.3 Dynamic decoupling

To extend the coherence time of the light storage on the clock transition imposed by magnetic dephasing we apply a composite refocusing pulse sequence on the ground

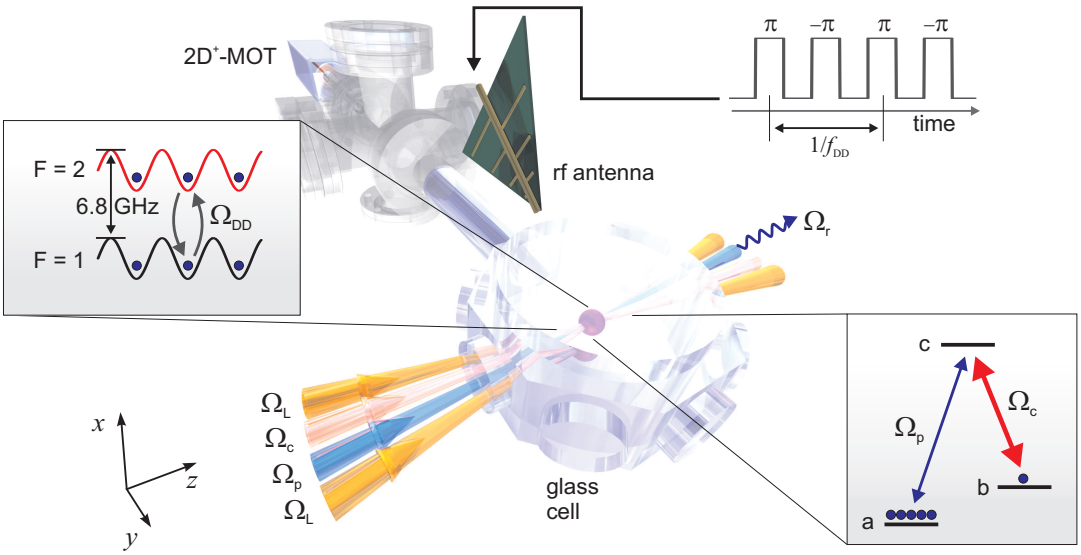

Figure 22: Essential elements of the experimental setup. A dense sample of cold ^{87}Rb atoms is prepared in a 1D optical lattice. Atomic levels used in the experiment are shown in the inset. A probe pulse Ω_p (peak power 130 nW, full width at half-maximum 82 ns) resonant with the $|a\rangle \leftrightarrow |b\rangle$ transition is converted into a spin wave by an adiabatically switching off the control field Ω_c. After a controllable storage period the spin wave is retrieved into a phase-matched direction by turning the probe field back on. The clock and the $(m_{F=1}, m_{F=2}) = (\pm 1, \mp 1)$ coherences are used to reduce sensitivity to the magnetic shifts. The polarization configurations of the probe and control fields are lin$\perp$lin for clock coherence and $\sigma^{\pm}/\sigma^{\mp}$ for the $(\mp 1, \pm 1)$ coherences. After loading, a bias magnetic field is applied along the major axis of the trap and atoms are either prepared in the $5S_{1/2}, F = 1, m = 0$ state by means of optical pumping when clock coherence is addressed, or left unpolarized when $(\pm 1, \mp 1)$ coherences are used. A 3.2 μm optical lattice prevents motional dephasing of the spin wave. The differential ac-Stark shift produced by the lattice is compensated by setting the bias magnetic field to the magic value. The extended spin-wave lifetimes are observed after applying a dynamic decoupling sequence of the microwave π pulses on the clock transition. A differential vacuum setup with a 2D$^+$-MOT cold-atom source allows us to achieve the long trap lifetimes in the experimental section.

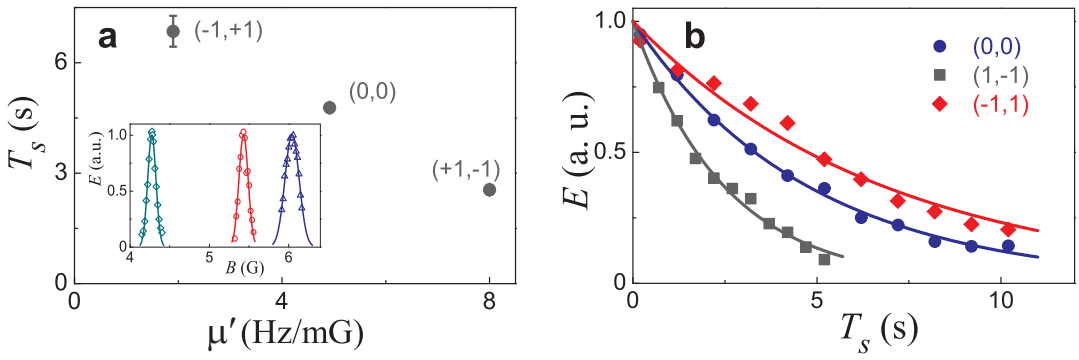

Figure 23: Measurements of magic field values and coherence lifetimes. a) Measured light-storage lifetimes vs sensitivity to the magnetic field for the three coherences. Longer lifetimes are observed for coherences with lower magnetic sensitivity, suggesting residual magnetic dephasing. Error bars represent uncertainties from the exponential fits. The inset shows retrieved pulse energy as a function of the magnetic field. The pulse is retrieved after 5, 7, and 2 s for (0,0), (-1,1), and (1,-1) coherences, respectively. The Gaussian fits yield corresponding magic field values $B^{(0)} = 4.27$, $B^{(-)} = 5.43$, and $B^{(0)} = 6.04$ G. b) Retrieved pulse energy as a function of storage time. The three long-lived coherences are used: (0,0) (circles), (-1,1) (diamonds), and (1,-1) (squares). When using clock coherence atoms were prepared in $m = 0$, otherwise left unpolarized. The solid lines are exponential fits to the data. The extracted $1/e$ lifetimes are 4.8(1), 6.9(4), and 2.5(1) s for the clock, (-1,1) (diamonds), and (1,-1) transitions, respectively.

level microwave transition. Dynamic decoupling (DD) pulse sequences have been studied in great detail in the context of reducing the decoherence induced by external perturbations on the two level system [82, 83, 84, 85, 86]. We apply the Carr-Purcell-Meiboom-Gill decoupling sequence [87] consisting of a train of resonant population-inverting microwave π-pulses on the clock transition. The phase of the microwave field is alternated by 180° for two adjacent pulses to reduce the influence of pulse imperfections. The DD sequence suppresses decoherence that is slow compared to the decoupling frequency $f_{DD} = 1/T_{DD}$, where $T_{DD}/2$ is the time interval between two consecutive pulses). For perfect 180° rotations the lifetime is generally expected to increase for higher f_{DD} [85, 86]. The measured values of extended lifetimes are shown in Fig. 24(a). The maximum $1/e$ lifetime of 16 s is measured for $f_{DD} = 60$ Hz (Fig. 24(a,b)). Shorter lifetimes are observed for higher f_{DD}. This is attributed to accumulation of rotation errors with increased number of pulses. Another limitation to the maximum observed lifetime is determined by atomic losses. With DD sequence applied all the atoms effectively spend half of the time in the relatively short-lived $|5S_{1/2}, F = 2, m_F = 0\rangle$ state. The measured lifetime of the atoms in the trap when DD sequence is applied is 20 s (Fig. 25).

In conclusion, we demonstrated light storage with a high efficiency and a several-seconds lifetime in a cold atomic gas confined in a differential ac Stark shift free optical lattice. With a dynamic decoupling sequence of microwave pulses applied on the ground-state transition we observed a light storage lifetime of 16 s, the longest achieved to our knowledge.

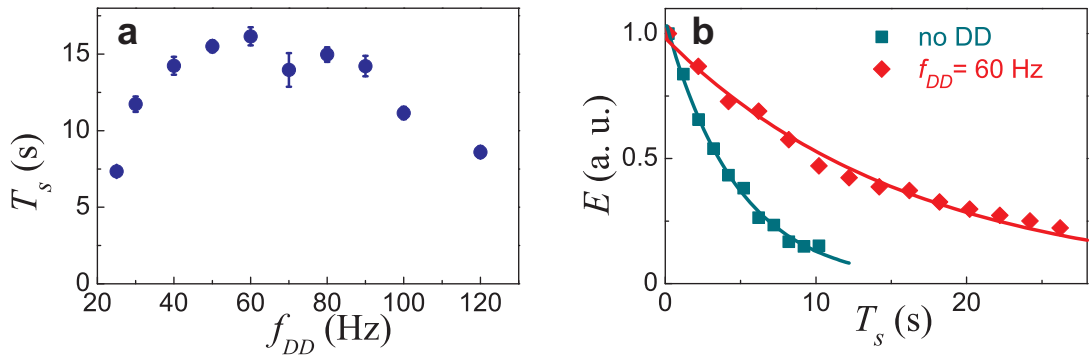

Figure 24: Light storage on the clock transition with dynamic decoupling. a) Lifetime as a function of the applied DD sequence frequency f_{DD}. The longest lifetime of 16 s is observed for $f_{DD} = 60$ Hz. Higher f_{DD} result in lower lifetimes attributed to the accumulation of pulse errors. b) Retrieved pulse energy as a function of storage time with (diamonds) and without (squares) DD sequence applied. The solid curves are exponential fits.

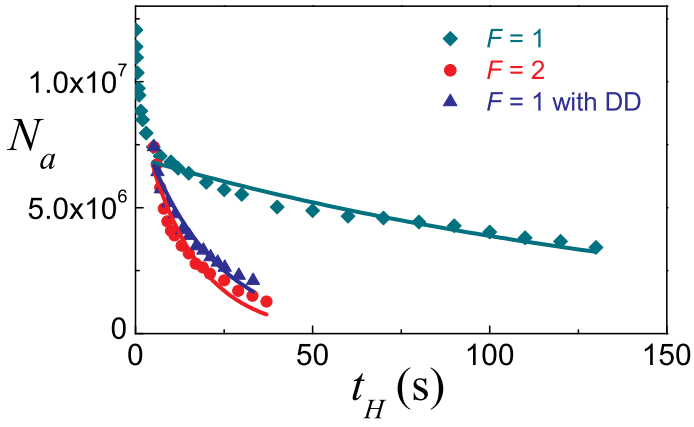

Figure 25: Number of trapped atoms as a function of the holding time. Atoms are prepared in $5S_{1/2}, F = 1$ (diamonds), $5S_{1/2}, F = 2$ (circles), and $5S_{1/2}, F = 1$ with DD sequence applied afterwards (triangles). Starting from 5 s the data are fit with exponents. The extracted lifetimes are 169(14), 15(1), and 20(1) s for atoms in $F = 1$, $F = 2$, and $F = 1$ with DD correspondingly.

CHAPTER IV

STRONGLY INTERACTING RYDBERG EXCITATIONS

This chapter is based on Ref. [16, 88].

4.1 Introduction

4.1.1 Rydberg atoms as a powerful platform

The realization of model systems of many particles with precisely controlled and widely tunable interactions is of considerable interest to improving our understanding of many-body quantum physics. Cold atomic gases have become a fruitful platform for such studies as they facilitate experiments under well-understood conditions [89, 4]. The interaction strength between Rydberg-level atoms can vary enormously depending on the principal quantum number n of the atomic level. An important manifestation of Rydberg-level interactions is the excitation blockade, where an atom promoted to a Rydberg level shifts the energy levels of nearby atoms, suppressing their excitation. Previously, the excitation blockade has been used to prepare entangled states of two isolated atoms [32, 33] and has also been observed in atomic gases [34, 35, 36, 37, 38, 39, 40, 41]. However, controlled creation and manipulation of collective quantum excitations would open the door to investigations of interacting bosonic and fermionic fields, simulations of engineered quantum systems, and generation of complex entangled states of matter and light [8, 9, 10, 11, 12, 13, 14, 15, 16]. Encoding of quantum information into symmetrized many-atom quantum states, or spin waves, is particularly attractive as discrimination against various types of noise is built into the manipulation and measurement protocols [19, 42, 43]. Notably, atomic spin waves can be efficiently mapped onto light fields, making such systems naturally suited for distribution of quantum information among remote locations.

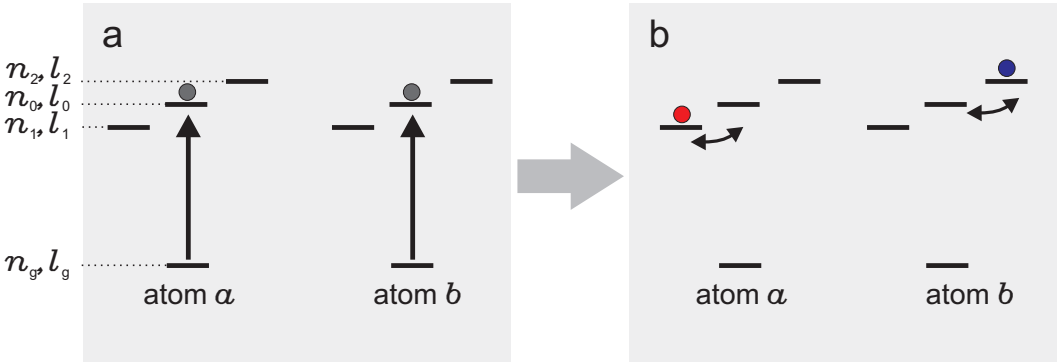

Figure 26: Illustration of the Förster resonance. a) Ground state atoms are excited into a Rydberg state $|n_0, l_0\rangle$. b) Virtual scattering processes couple initial two-atom state to two-atom states of equivalent energy, giving rise to dipole-dipole interactions.

4.1.2 Interactions between Rydberg atoms

The origin of strong interactions between Rydberg atoms is in the so-called Förster resonances [90]. The basic idea is as follows. Let us consider two atoms, a and b, separated by a distance R and excited into a Rydberg state with principal and angular quantum numbers n_0 and l_0 (Fig. 26(a)). The state of the two atoms can be written as a product $|n_0, l_0\rangle_a |n_0, l_0\rangle_b$. Let us now assume that the atoms have other Rydberg levels $|n_1, l_1\rangle$ and $|n_2, l_2\rangle$, such that the sum of their energies is equal to twice the $|n_0, l_0\rangle$ energy: $E_{n_1,l_1} + E_{n_2,l_2} = 2E_{n_0,l_0}$. In this case the initial two-atom state is energetically equivalent to two-atom states $|n_1, l_1\rangle_a |n_2, l_2\rangle_b$ and $|n_2, l_2\rangle_a |n_1, l_1\rangle_b$. This is the condition for a Förster resonance. Because of the energetic degeneracy there are virtual scattering processes which take the atom pair from the initial state into the coupled states (Fig. 26(b)). The eigenstates of the system turn out to be superpositions of the states of different parity, and therefore they possess non-vanishing dipole moments. The dipole-dipole interaction between Rydberg atoms lifts degeneracy and shifts the states that could be coupled to the ground state by the amounts $\pm C_3/R^3$ (not taking in the account angular part of the wave function) [5]. Here C_3 is $e^2 \langle r \rangle_{n_0,l_0}^{n_1,l_1} \langle r \rangle_{n_0,l_0}^{n_2,l_2}$,

where e is electron charge and $\langle r \rangle_{n_0,l_0}^{n_{1,2},l_{1,2}}$ are radial matrix elements. This means that two atom Rydberg states will be spectroscopically separated from the bare atomic resonance and cannot be excited with a laser tuned to the single-atom resonance. Instead the laser will excite a symmetric superposition state $|\Psi\rangle = |n_0, l_0\rangle_a |g, l\rangle_b + |g, l\rangle_a |n_0, l_0\rangle_b$, in which one of the atoms in in the Rydberg state and the other one is in the ground state. This phenomenon is called the Rydberg blockade and has been studied extensively both theoretically and experimentally [5].

In reality the energy degeneracy for two-atom states is not perfect and there is a finite energy difference $\delta E = E_{n_1,l_1} + E_{n_2,l_2} - 2E_{n_0,l_0}$, called the energy defect. As a result, atom-atom interaction energy V changes its behavior from the dipole-dipole ($1/R^3$) to the van der Waals ($1/R^6$) at a distance at which it becomes comparable to the energy defect δE [5]. Interaction energy dependence on the distance between the atoms may be expressed analytically as follows:

$$V = \frac{\delta E}{2} - sign(\delta E)\sqrt{\frac{\delta E^2}{4} + \frac{C_3^2}{R^6} D_\phi}, \tag{10}$$

where D_ϕ are van der Waals eigenvalues, typically between 0 and 1 [5].

An accurate calculation of the interaction energy requires summation over other collision channels $|n_0, l_0\rangle_a |n_0, l_0\rangle_b \rightarrow |n_i, l_i\rangle_a |n_j, l_j\rangle_b$, satisfying dipole selection rules, accounting for angular dependence of interaction strength, external field, and Zeeman states [5, 91], but Eq.(10) provides a useful order-of-magnitude estimate.

The basic arguments for a two-atom blockade are transferable to a many-atom case [8]. For a collection of N atoms, where $N >> 1$, multiply excited (with more then one Rydberg atom) states are spectroscopically separated from the singly-excited states. In this case the excited state with only one Rydberg atom takes the form of a symmetrized many-atom quantum state, or spin wave, similar to that produced in the DLCZ protocol. Therefore these states share the same advantage of collectively enhanced (by $\sqrt{N}$) coupling strength to a light mode. The great advantage is that

while in the DLCZ protocol such states are produced with very low probability, such production can be done with probability of 1 using Rydberg interactions, at least in theory.

4.1.3 Dephasing vs blockade

When the atomic sample is too large compared to the effective range of atom-atom interactions, or the spectral profile of the excitation light is too wide compared to the energy gap between singly- and multiply-excited states, the Rydberg blockade breaks down. To be more precise, the probability of having a doubly excited state scales as $p_{doub} \sim \frac{1}{4\pi(\overline{\kappa}T)^2}$ [8], where $\hbar\overline{\kappa} = C_3/R^3$ (for the atomic pair that is furthest apart) is the energy gap between the singly excited states and multiply excited states, and T is the excitation duration for a Fourier-transform-limited pulse. More recent work indicates that requirements for the Rydberg blockade in a mesoscopic sample may be even stricter [92].

As an alternative mechanism to the blockade approach, dephasing of multiple spin waves was proposed in [16]. This mechanism does not require a Rydberg blockade at any point and is easiest to understand without taking the blockade into account, although in a real experiment both of the mechanisms are likely to contribute. An approach to creating single spin waves is shown in Fig. 27. The protocol starts with the excitation to a Rydberg level. Since there is no blockade, the number of excited atoms follows a Poissonian distribution. The optimal efficiency of the protocol is achieved when on average one atom is excited. The excitation step is followed by the interaction (dephasing) period of duration ΔT. Multiply excited spin waves will accumulate random phase shifts due to atom-atom interactions and will not be retrieved into the phase-matched direction during the readout stage. Therefore, only the vacuum and the singly-excited spin wave will be transformed into a light field emerging from the ensemble in a phase-matched direction. A phase shift acquired by

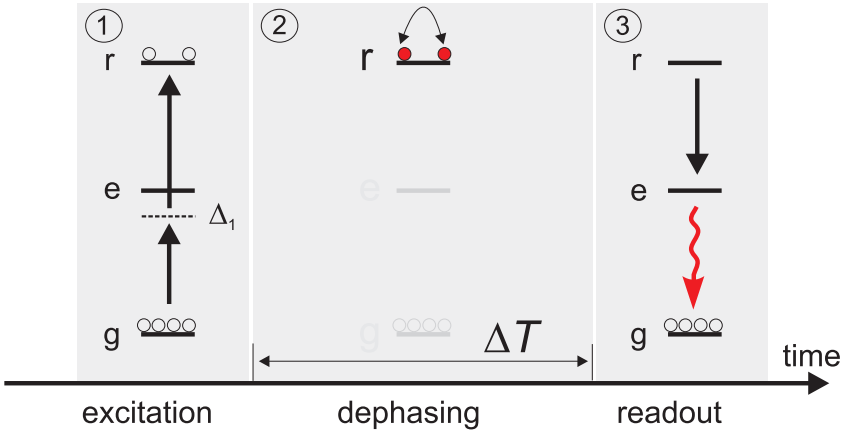

Figure 27: Time sequence for the dephasing protocol and relevant energy levels. Atoms are prepared in the ground state $|g\rangle$ and two-photon excited into the Rydberg level $|r\rangle$ with one-photon detuning Δ_1 from the intermediate state $|e\rangle$. An excitation stage is followed by the dephasing and readout stages.

an atomic pair (μ, ν) is $\varphi_{\mu,\nu} = V^{\mu,\nu}(R_{\mu,\nu})\Delta T$, where $V^{\mu,\nu}$ is the interaction energy at a distance $R_{\mu,\nu}$ between atoms. For a coherent spin-wave state truncated at two excitations the second-order autocorrelation function of the retrieved field is [16]

$$g^{(2)} = 4g^{(2)}(0)\frac{|\frac{1}{N^2}\sum_{\mu=1}^{N}\sum_{\nu\neq\mu}e^{i\varphi_{\mu\nu}}|^2}{[1+\frac{1}{N^3}\sum_{\mu=1}^{N}|\sum_{\nu\neq\mu}e^{i\varphi_{\mu\nu}}|^2]^2}, \tag{11}$$

where summation is over all possible atom pair combinations and $g^{(2)}(0) = e/4$ is a corresponding value of $g^{(2)}$ for a truncated coherent state.

4.2 Observation of strongly interacting Rydberg excitations of a cold atomic gas

4.2.1 Atomic sample preparation

The small size of the atomic ensemble is a prerequisite for complete suppression of multiply excited spin waves. The ensemble should also have sufficiently large optical depth to couple the atomic spin wave to the retrieved light field. To create such a

small and dense ensemble, we load laser-cooled ^{87}Rb atoms into a one-dimensional optical lattice. A ^{87}Rb magneto-optical trap is loaded from background vapor for 70 ms. During the 25 ms post-cooling stage, detuning of the cooling light is increased, repumper intensity is decreased, and the optical lattice is turned on. The lattice is formed by a retro-reflected (782 nm wavelength) light beam with Gaussian $1/e^2$ waists of $w_y = 15$ μm and $w_z = 55$ μm along the y- and z-dimensions, respectively, Fig. 28(a). The initial lattice beam power is 10 mW, which is lowered to 6 mW during the post-cooling stage. The geometry of the lattice and of the excitation beams is chosen such that the ensemble volume is determined by the $w_e = 9$ μm waists of the excitation beams in two dimensions (x and z) and the 15 μm lattice waist in the third (y). The peak atom density $\rho_0 \approx 3 \times 10^{11}$ cm^{-3} is inferred from the fluorescence imaging of the trapped sample. Atoms are prepared in the $|5s_{1/2}, F = 2, m_F = 0\rangle$ state by optical pumping in a magnetic bias field $B_0 = 4.3$ G applied along the z axis.

4.2.2 Rydberg excitation and readout

After preparation, the lattice is turned off with an acousto-optical modulator (AOM) in order to avoid differential light shifts, and a 2.5 μs long experimental cycle is repeated for a period of 200 μs, limited by thermal expansion of the $T \simeq 10$ μK atomic cloud, with a 1 μs optical pumping period repeated after every five cycles. The overall repetition rate of the experiment is 8.3 Hz. A $\tau_e = 200$ ns long period of two-photon excitation by nearly counter-propagating linearly polarized along the z-axis 795 nm (Ω_1) and 475 nm (Ω_2) laser fields tuned near the two-photon $|5s_{1/2}, F = 2\rangle \leftrightarrow |ns_{1/2}\rangle$ resonance creates an optical-frequency spin wave between the ground and the Rydberg levels (Fig. 28(b)).

The 795 nm resonant light used for the lower leg of the two-photon transition is derived from an extended cavity diode laser (ECDL) locked to a rubidium absorption line. Light at 475 nm light is produced by frequency-doubling of power amplified 950

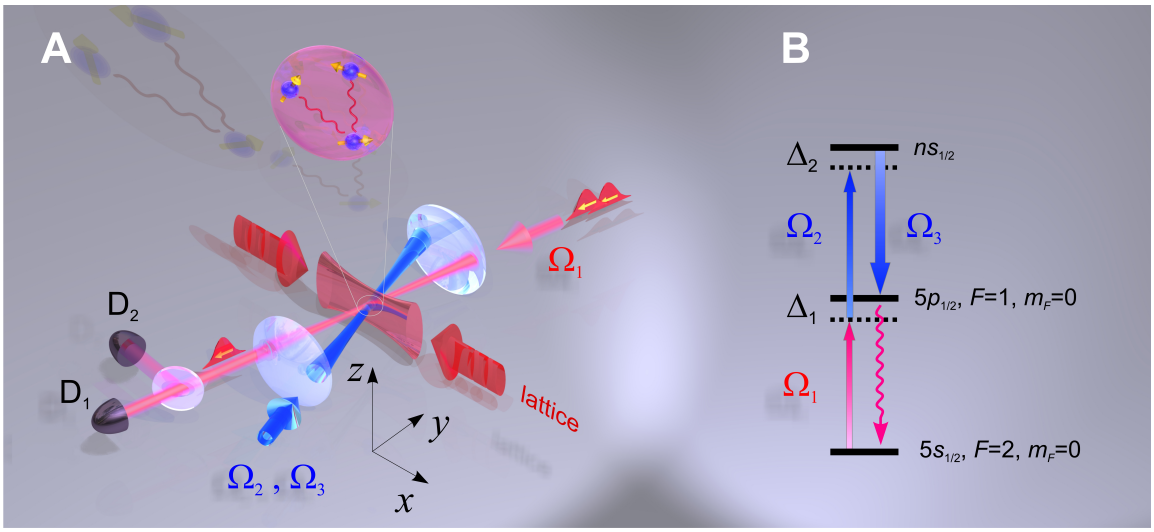

Figure 28: a) A cold dense sample of atomic ^{87}Rb is prepared in a 1-D optical lattice. The lattice is turned off for the experimental sequence, in which nearly counter-propagating 475 nm (Ω_1) and 795 nm (Ω_2) light fields excite a spin wave between the ground $|5s_{1/2}\rangle$ and a Rydberg $|ns_{1/2}\rangle$ level. After a variable delay, a read-out pulse of 475 nm light (Ω_3) converts the Rydberg spin wave into a light field. A Hanbury Brown-Twiss setup of a beamsplitter BS followed by two detectors D_1 and D_2 is used to measure the second-order intensity correlation function $g^{(2)}(0)$ of the idler field. b) Relevant ^{87}Rb energy levels. Electronic, hyperfine, and Zeeman quantum numbers are shown. The detuning from the intermediate $|5p_{1/2}\rangle$ level is $\Delta_1 = -40$ MHz; the detuning Δ_2 is varied for the data in Fig. 29(a), otherwise it is fixed at the two-photon resonance $|5s_{1/2}, F = 2\rangle \leftrightarrow |ns_{1/2}, m = \pm 1/2\rangle$ between the ground level and one of the Zeeman sub-levels of the Rydberg level ($|\Delta_2| \approx 6$ MHz).

nm ECDL light which is frequency-locked to a reference cavity (Appendix C). The length of the reference cavity is actively stabilized with 780 nm ECDL light which is locked to a rubidium line. The frequency of the 475 nm transition to Rydberg levels is calculated using quantum defect values of Ref. [93]. A transition is found by scanning the 475 nm light frequency across a resonance and measuring photoelectric detection probability for the retrieved field. Initial coarse laser tuning is done using a wavemeter. Since Ω_2 and Ω_3 fields are propagating in the same spatial mode, the retrieved field is phase-matched into the original field mode Ω_1, which is coupled into a single mode fiber followed by a 50/50 fiber beamsplitter and a pair of single-photon detectors D_1 and D_2. To prevent damage to single photon detectors by the excitation field, a gating AOM is used at the fiber beamsplitter input port.

After a controlled storage period T_s, a 475 nm retrieval field (Ω_3) resonant with the $|ns\rangle \leftrightarrow |5p_{1/2}\rangle$ transition illuminates atoms for a 1 μs period. This read-out laser pulse converts the spin wave into the retrieved field, which is coupled into a single-mode fiber followed by a beam-splitter and a pair of single-photon detectors D_1 and D_2. Statistics of the retrieved spin wave is inferred from the distribution of the photoelectric detection events.

4.2.3 Experimental data

The sum of the photoelectric detection event probabilities at the two detectors, $P = p_1 + p_2$, is shown in Fig. 29(a) as a function of the two-photon detuning Δ_2 from level $|90s_{1/2}\rangle$. The two peaks correspond to $m = \pm 1/2$ Zeeman sub-levels split by the bias field B_0; the width of the peaks, $\gamma \approx 2\pi \times 5$ MHz, is likely determined by the spectral widths of the excitation laser pulses. In Fig. 29(b), the time-resolved photoelectric detection probability P is shown for values of n between 50 and 102. With a $\sim n^{-3/2}$ scaling of the dipole matrix element, and hence, of the Rabi frequency Ω_3 for the $|5p_{1/2}\rangle \leftrightarrow |ns_{1/2}\rangle$ transition, the retrieved field duration increases with n for a fixed

power (18 mW) of the 475 nm read-out field.

In Fig. 29(c), P is shown as a function of the two-photon excitation pulse area $\theta \equiv \Omega\tau_e$ for $n = 74, 81$, and 90, where the peak two-photon Rabi frequency is $\Omega \simeq (\Omega_1\Omega_2)/(2\Delta_1)$ in the limit $\Omega_{1,2} \ll \Delta_1$. The duration of the excitation pulse τ_e is kept at 200 ns in this work; pulse area θ is varied by changing the intensity of the Ω_1 and Ω_2 fields. In the case of strong excitation blockade, collective Rabi oscillations occur even for inhomogeneous atom-light coupling [94]. Technical sources of dephasing, such as laser linewidth, ac Stark shifts, and atom number fluctuations, are expected to reduce P to half of its maximum value as θ is increased. In contrast, in Fig. 29(c), we observe a decay of P to zero, with no revivals. These observations are consistent with dephasing of multiply-excited spin waves [16]. The data for n=90 are fit with a function $\zeta\mathcal{P}\theta^2\exp(-\mathcal{P}\theta^2)$, where $\zeta = 0.060(1)$ and $\mathcal{P} = 51(1)$ are adjustable parameters. The choice of the fit function is suggested by a model with Poisson spin-wave excitation statistics [16, 95]. Within the model, ζ corresponds to the overall measured retrieval and detection efficiency for the spin-wave excitation, while the maximum photoelectric detection probability is $P_m = \zeta/e$.

It is instructive to compare the strongly interacting regime to the ideal limit of a non-interacting ensemble, where each atom undergoes a Rabi oscillation between the ground level $|5s_{1/2}\rangle$ and the Rydberg level $|ns_{1/2}\rangle$ with the position-dependent two-photon Rabi frequency $\Omega(\mathbf{r})$. Atoms in a sufficiently low-n Rydberg level may be used to approximate this ideal situation. In Fig. 29(d), $P/\mathcal{T}$ is displayed as a function of θ both for high- and low-n Rydberg levels. The retrieved field is attenuated (for low-n) by a factor $1/\mathcal{T}$ to prevent saturation of the single-photon detectors D1 and D2. The weakly interacting (low-n) regime is represented by measurements with levels $|19s_{1/2}\rangle$ and $|21s_{1/2}\rangle$ ($\mathcal{T}_{19,21} = 0.05$). The data for n=19 and n=21 in Fig. 29(d) are fitted with the function $f(\theta) = \left(2/w_0^2\int_0^\infty \sin(\theta e^{-2r^2/w_0^2})e^{-r^2/w_0^2}rdr\right)^2$ which describes amplitude averaging of the sinusoidal Rabi oscillation over the Gaussian transverse

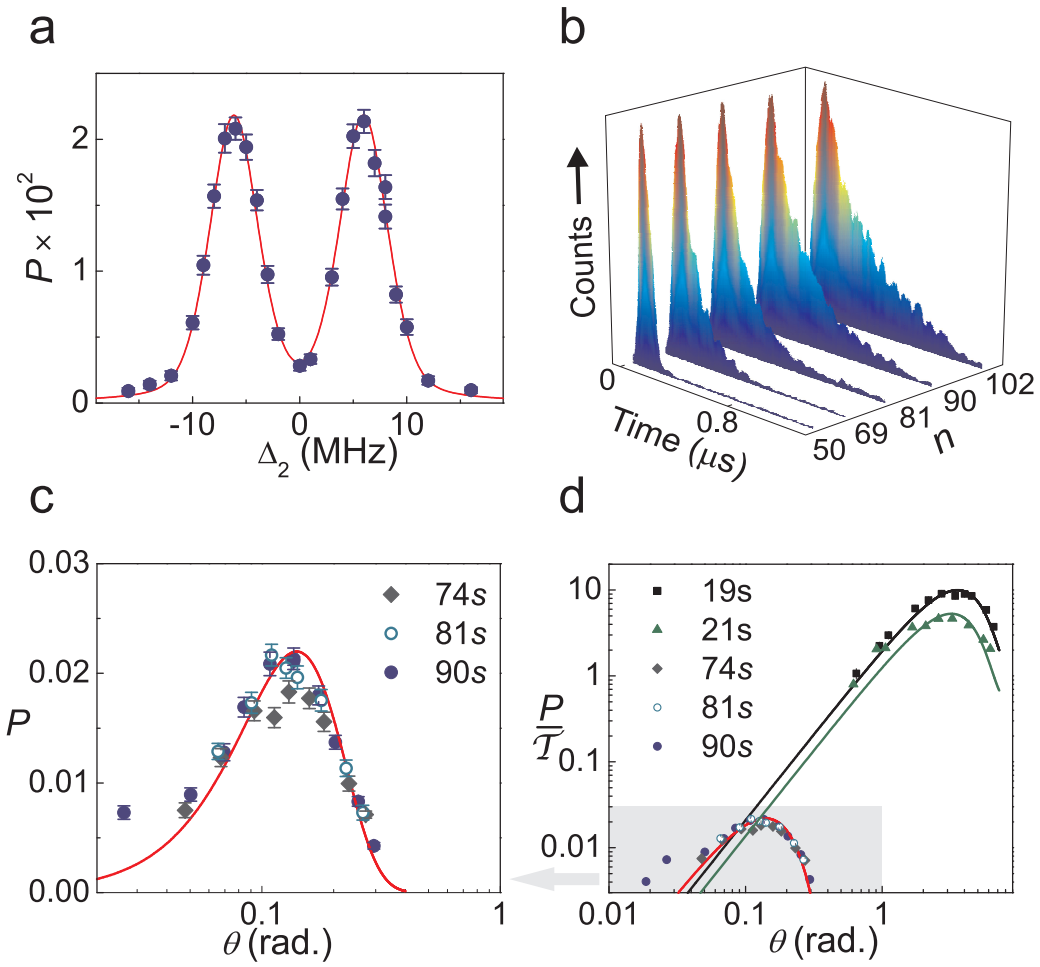

Figure 29: a) Probability P of photoelectric detection event per trial as a function of two-photon detuning Δ_2 shows the $m = \pm 1/2$ Zeeman components of level $|90s_{1/2}\rangle$ split by the bias field B_0. The solid curve is a pseudo-Voigt fit. b) Normalized temporal profiles of the retrieved field for upper levels $|ns_{1/2}\rangle$ for n between 50 and 102, with a fixed power of the retrieval field Ω_3. c) P as a function of (single-atom) two-photon excitation pulse area θ for $T_s = 0.4$ μs: solid circles for $|90s\rangle$, open circles for $|81s_{1/2}\rangle$, and diamonds for $|74s_{1/2}\rangle$ upper level. The solid curve is a fit of the form $\zeta\mathcal{P}\theta^2 \exp(-\mathcal{P}\theta^2)$ to the $|90s_{1/2}\rangle$ data. d) $P/\mathcal{T}$ as a function of θ, results plotted in (c) are shown together with additional data for levels $|19s_{1/2}\rangle$ and $|21s_{1/2}\rangle$. The data for n=19 and n=21 are taken with the retrieved field attenuated by a factor $1/\mathcal{T}_{19,20}$ =20 to avoid detector saturation, whereas for n=74,81, and 90 no attenuation is used ($\mathcal{T}_{74,81,90}$ =1). The n=19 and n=21 data are fitted with a function accounting for averaging of sinusoidal oscillations of the retrievable spin-wave amplitude across the Gaussian transverse spatial profiles of $\Omega_{1,2}(\mathbf{r})$ (*26*). Error bars represent ± one standard deviation ($\sqrt{M}$) for M photoelectric counting events.

profiles of excitation beams with waists w_0, where r is the radial distance from the mode center. The second multiplier in the integral, e^{-r^2/w_0^2}, accounts for the finite size of the retrieved mode of the same waist. Atomic interactions, laser linewidths and finite sample size are not included in this model.

The maximum photoelectric detection probability P_m and the corresponding pulse area θ_m are lower for $n = 21$ than for $n = 19$, indicative of interaction-induced excitation suppression. Results for $n = 74, 81, 90$ ($\mathcal{T}_{74,81,90} = 1$) suggest that for such high n, both P_m and θ_m approach asymptotic values. This would be expected if only a single retrievable excitation is generated in the entire ensemble. In this picture, the effective number of atoms $\mathcal{N}$ in the ensemble is proportional to the ratio of $P_m/\mathcal{T}$ for n=19 and n=90, giving $\mathcal{N} \simeq 5 \times 10^2$. Collectively-enhanced coupling of the driving laser fields to the singly-excited spin wave implies $\mathcal{N} \sim (\theta_m(n = 19)/\theta_m(n = 90))^2 \simeq 6 \times 10^2$. In the absence of data for $n < 19$, these values should be considered as low-end estimates of $\mathcal{N}$.

4.2.4 Quantum statistics

The single-photon character of the retrieved field is explicitly confirmed by cross-correlating the photoelectric counting events at detectors D_1 and D_2 as a function of time delay, shown for upper level $|102s_{1/2}\rangle$ in inset to Fig. 30. Every experimental trial data acquisition is triggered and photoelectric events on detectors D_1 and D_2 are recorded within a gated time interval determined by the length of the retrieved pulse. Photoelectric detection probabilities for both detectors are calculated as $p_{1,2} = N_{1,2}/N_0$, where $N_{1,2}$ are numbers of recorded events and N_0 is the number of received triggers. Photoelectric detection probability for double coincidences is calculated as N_{12}/N, where N_{12} is a total number of simultaneous clicks on both detectors for a given experimental trial. The second order intensity correlation function at zero delay is given by $g^2(0) = p_{12}/(p_1 p_2)$.

The observed coincidences around zero time delay are strongly suppressed, providing evidence for the quantum nature of the emitted light. We further investigate the transition to the regime of strongly interacting spin waves by measuring the second-order intensity correlation function at zero delay $g^{(2)}(0)$ as a function of effective principal quantum number $n^* = n - \delta_s$ (Fig. 30). Here, $\delta_s = 3.13$ is the s-wave quantum defect for Rb. As n^* is increased, interaction-induced suppression of spin waves with more than one Rydberg atom sets in, with the transition to the single retrievable excitation regime occurring for $n \sim 60 - 70$. The transition is associated with the interaction strength scaling as n^4/R^3 in the dipole-dipole regime for $R \lesssim R_c$ and as n^{11}/R^6 in the van der Waals regime for $R \gtrsim R_c$. Here R_c is the critical inter-atom distance [5]. For $n \lesssim 60$, van der Waals interactions are relevant because $R_c \lesssim 3$ μm is sufficiently smaller than the ~ 10 μm sample size. In contrast, for $n \sim 100$, dipole-dipole interactions become operational as $R_c \simeq 10$ μm. For Rydberg levels with principal quantum numbers $n < 40$ (Fig. 31), multiple photon events are not suppressed and, as expected, measured $g^2(0)$ is consistent with unity. As an additional check of the detection procedure, employing classical light pulses within the same experimental sequence resulted in $g^2(0) = 0.99(2)$.

High quality single-photon statistics are observed for $n \gtrsim 90$. For an ideal single-photon source, $g^2(0)$ would be non-zero only due to background counts on $D_{1,2}$. The measured background photoelectric count probability is $P_B = 2.5 \times 10^{-4}$ for the 0.74 μs detection window, with $P_D = 0.55 P_B$ resulting from detector dark counts, and the remainder caused by various scattered light sources. The measured value of $g^{(2)}(0) = 0.040(14)$ for level $|102s_{1/2}\rangle$ is consistent with a lower bound of $g^{(2)}_{bg} = 0.025(1)$ due to background counts. A dearth of excess coincidences indicates a strong suppression of spin waves with more than one excitation. Both excitation blockade and spin-wave dephasing can contribute to suppression of two-photon events. As a step to separating the roles of the two mechanisms, we employ $|nd_{3/2}\rangle$ upper levels for

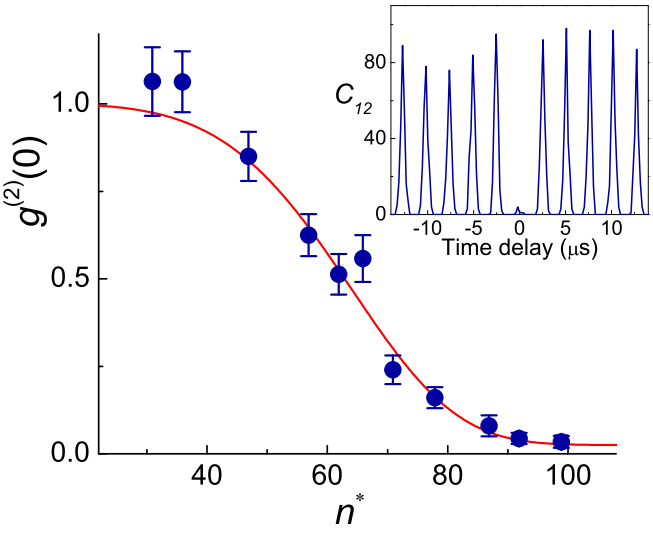

Figure 30: Measured second-order intensity correlation function at zero time delay $g^{(2)}(0)$ as a function of the effective principal quantum number $n^* = n - \delta_s$ of the upper level $|ns_{1/2}\rangle$ for $T_s \simeq 0.3$ μs. For $n^* > 70$, the data is taken at θ_m, whereas for $n^* \lesssim 70$ the values of θ are chosen to keep P between 0.02 and 0.03 (cf. Fig. 29(d)). The solid line is a fit of the form $g^{(2)}(0) = (1 - g^{(2)}_{bg}) \exp(-(n^*/n^*_0)^\alpha) + g^{(2)}_{bg}$, with best-fit values $\alpha = 4.7(4)$ and $n^*_0 = 67(1)$. The inset shows cross-correlated coincidence counts C_{12} as a function of time delay for upper level $|102s_{1/2}\rangle$. Error bars represent $\pm$ one standard deviation ($\sqrt{M}$) for M photoelectric counting events.

which the excitation blockade is expected to break down due to a pronounced angular dependence of interactions between atom pairs [5]. The observed strong suppression of two-photon events ($g^{(2)}(0) = 0.066(38)$ for level $|88d_{3/2}\rangle$ and $g^{(2)}(0) = 0.075(26)$ for level $|100d_{3/2}\rangle$) suggests a significant role of spin-wave dephasing in our experiment.

The measured probability of photoelectric detection per trial P was $2-3\%$ for the data in Fig. 30. When normalized by the 0.52 measured optical transmission from the sample to the detectors (transmission through a glass vacuum chamber (0.92), gating AOM diffraction efficiency (0.77), and fiber coupling efficiency (0.73)) and 0.55 single-photon detector efficiency, $P_m(n = 90) = 2.8\%$ corresponds to $\epsilon \approx 0.10$ single photon generation efficiency. This is limited by several experimental imperfections.

The retrieval field Ω_3 has the same spatial mode as the excitation field Ω_2. Higher available laser power and a larger spatial mode for Ω_3 are expected to increase ϵ. A smaller sample should lead to a pronounced excitation blockade, while a medium-to-low finesse cavity may increase spin wave retrieval efficiency. As it is, the single photon source has lower $g^{(2)}(0)$, higher P, and is more than three orders of magnitude faster than a deterministic single photon source [44] based on the DLCZ protocol [19].

4.2.5 Coherence properties of Rydberg spin waves

To evaluate coherence properties of the created optical spin-wave excitations, the retrieved signal is measured as a function of storage time T_s. For this data, an extended 5 μs-long timing sequence is used. For $n = 90$, the signal is shown in Fig. 31(a). The observed $1/e$ coherence time $\tau_{90} = 2.5(1)$ μs is consistent with the decoherence expected from atomic motion which smears the phase grating imprinted on the atoms during the excitation. The period of the spin wave formed by counter-propagating Ω_1 and Ω_2 fields is $\Lambda \simeq 1$ μm. The expected motional coherence time is $\tau \simeq \Lambda/(2\pi v) \simeq 5$ μs, where $v = (k_B T/M)^{1/2} \simeq 3$ cm/s is the atomic velocity, k_B is Boltzmann's constant, $T = 10$ μK is the atomic temperature, and M is the mass of ^{87}Rb. In principle, there may be additional sources of decoherence for highly excited Rydberg levels, such as stray electric fields. To test this, a similar measurement is performed for $n = 34$ (Fig. 31(b)). The excitation level is kept low to preclude influence of interactions of multiply-excited spin waves. The somewhat higher value of the observed coherence time $\tau_{34} = 3.0(1)$ μs may indicate a possible contribution to τ_{90} of Rydberg atom interactions with other atoms or external electric fields. However, atomic motion appears to provide the dominant contribution to the observed decoherence, also confirmed by lower values of τ in measurements with higher sample temperatures. In the future, it should be possible to reduce motional dephasing by further cooling. One may also utilize multi-photon excitation to produce larger period spin waves which

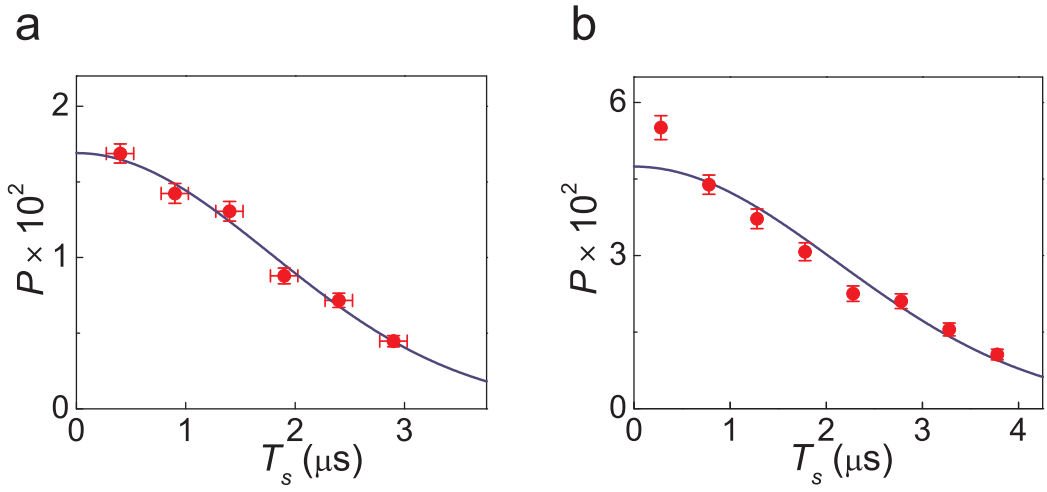

Figure 31: Photoelectric detection probability P as a function of the storage time T_s. a) For upper level $|90s_{1/2}\rangle$; b) for upper level $|34s_{1/2}\rangle$. Experimental data showing decay are fitted with a Gaussian function $\exp(-T_s^2/\tau^2)$, with best-fit values $\tau_{90} = 2.5(1)$ μs and $\tau_{34} = 3.0(1)$ μs. The vertical error bars represent $\pm$ one standard deviation ($\sqrt{M}$) for M photoelectric counting events. The horizontal error bars represent the lengths of the retrieved light pulses.

are less susceptible to atomic motion [16], or pin the spin wave in a magic-wavelength (for the ground-Rydberg transition) optical lattice [96].

The function $g^{(2)}(0)$ is expected to decrease with T_s as atom-atom interactions lead to the dephasing of multiply-excited spin waves. The data for $n = 60$ shown in Fig. 32 indeed suggest such a decrease.

We have shown that strong Rydberg-level interactions can be used for fast preparation of single quantum excitations of a cold atomic gas. Using two different spin waves within the same ensemble, each driven by an independent single-photon field Ω_1, a photon-photon quantum gate can be realized. This work can be extended to the creation of several entangled spin waves [16]. This would also allow investigation of interacting fermionic and bosonic collective excitations [11]. Entangled spin waves may also be mapped either onto long-lived atomic coherences or light fields, opening possibilities for scalable remote entanglement distribution [13, 16].

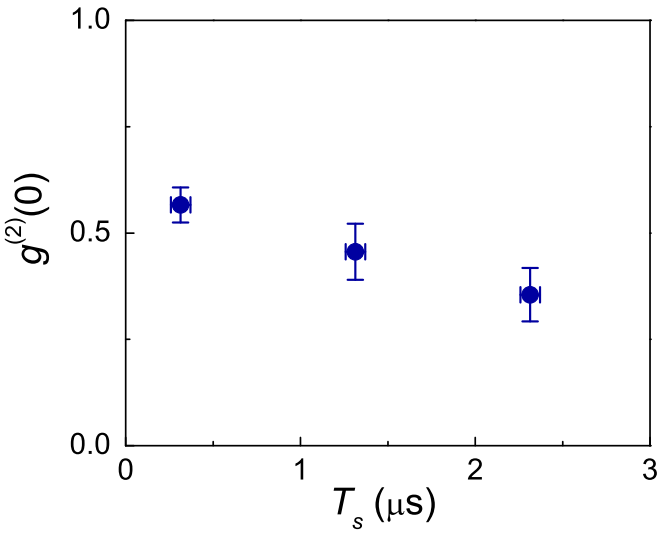

Figure 32: Second-order intensity correlation function $g^{(2)}(0)$ for $n = 60$ as a function of the storage period T_s. The vertical error bars represent $\pm$ one standard deviation ($\sqrt{M}$) for M photoelectric counting events. The horizontal error bars represent the lengths of the retrieved light pulses.

4.3 Microwave dressing of Rydberg atoms

4.3.1 Single photon generation

At a crossover distance $R_c \approx (\frac{C_3\sqrt{D_\varphi}}{\delta E})^{1/3}$ interaction energy changes it's behavior from dipole-dipole to much more rapidly decaying van der Waals. The interaction range may be increased by creating induced dipole moments resulting from mixing of opposite parity states (for example s and p orbitals) with microwave fields [16]. Microwave transitions typically have frequencies in a conveniently accessible range from a few to a few tens of GHz and very sizable dipole moments, such that microwave manipulations can easily be done on tens-of-ns timescales with not much power required. The idea is illustrated in Fig. 33 with timing sequence shown in Fig. 34. It is similar to dephasing protocol described earlier. First step is excitation of the coherent spin wave in $|ns\rangle$ state with one excitation on average. After the spin wave is excited a $\pi/2$ microwave resonant pulse creates superposition $1/\sqrt{2}(|ns\rangle + |np\rangle)$.

Two atom states, symmetric and antisymmetric superpositions $|s\rangle|p\rangle + |p\rangle|s\rangle$ and $|s\rangle|p\rangle - |p\rangle|s\rangle$ (Fig. 33), are a subject to strong resonant dipole-dipole interactions, which do not change their dependence to $1/R^6$ at any point. Multiply excited spin waves are allowed to dephase during time interval ΔT, after which restoring $3\pi/2$ microwave pulse brings population back to $|ns\rangle$ state. During the final step the spin wave excitation is converted to light by an optical readout pulse. For a coherent spin-wave state truncated beyond two excitations the expression (11) for the retrieved field second order autocorrelation function becomes

$$g^{(2)} = 4g^{(2)}(0)\frac{|\frac{1}{N^2}\sum_{\mu=1}^{N}\sum_{\nu\neq\mu} e^{i\varphi_{\mu\nu}}\cos\left(\frac{\varphi_{\mu\nu}}{2}\right)|^2}{[1+\frac{1}{N^3}\sum_{\mu=1}^{N}|\sum_{\nu\neq\mu} e^{i\varphi_{\mu\nu}}\cos\left(\frac{\varphi_{\mu\nu}}{2}\right)|^2]^2}. \quad (12)$$

This expression differs from (11) by cosine multipliers, which result from microwave dressing. After summation over all the atoms the random phase multipliers $e^{i\varphi_{\mu\nu}}\cos\left(\frac{\varphi_{\mu\nu}}{2}\right)$ average not to zero but to 1/2, and $g^{(2)}$ approaches its asymptotic value of $g^{(2)}(0)16/25$ [16]. The results of a simulation from Ref. [16] are shown in Fig. 35. The $g^{(2)}$ value may be further reduced by repeating the microwave sequence with other adjacent p levels as shown in the inset to Fig. 35.

4.3.2 Spin-wave entangling gate

For $n >> 1$, the dipole coupling between Rydberg levels ns and $n'p$ decays rapidly as the energy difference increases: for example, for $n = 100$ the interaction strength between adjacent $100s$ and $99p_j$ or $100p_j$ orbitals is 100 times larger than that for $100s$ and $98p_j$ or $101p_j$ [5, 97]. Therefore independent weakly interacting spin waves may be created in levels ns and $n's$ with sufficiently different n and n'. In addition, these single spin waves may also be transported through the Rydberg spectrum by using single-particle microwave π pulses: the phase matching condition is not affected provided the Rydberg transition wavelength is much larger than the ensemble size.

A protocol to entangle two independent spin waves a and b in levels n and $n' = n+1$

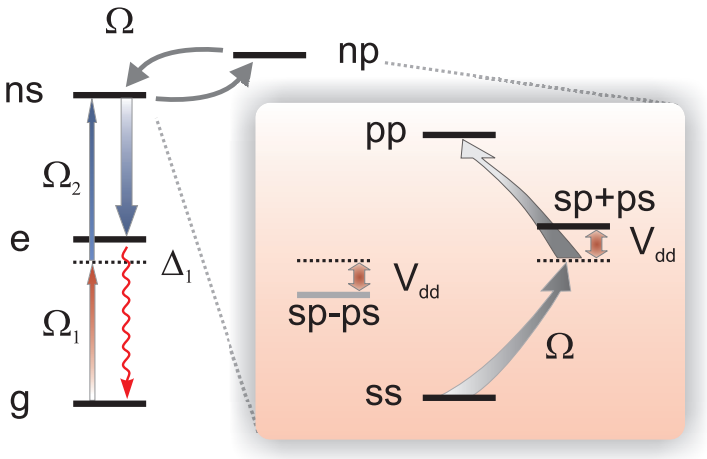

Figure 33: Ground level atoms are two-photon excited to a Rydberg s level, which is then mixed with a p orbital by applying a microwave pulse of Rabi frequency Ω. The inset shows the effect of dipole-dipole interaction and microwave dressing of an atom pair. The atomic spin wave is retrieved from the Rydberg state with a π pulse resonant to a low-lying excited state.

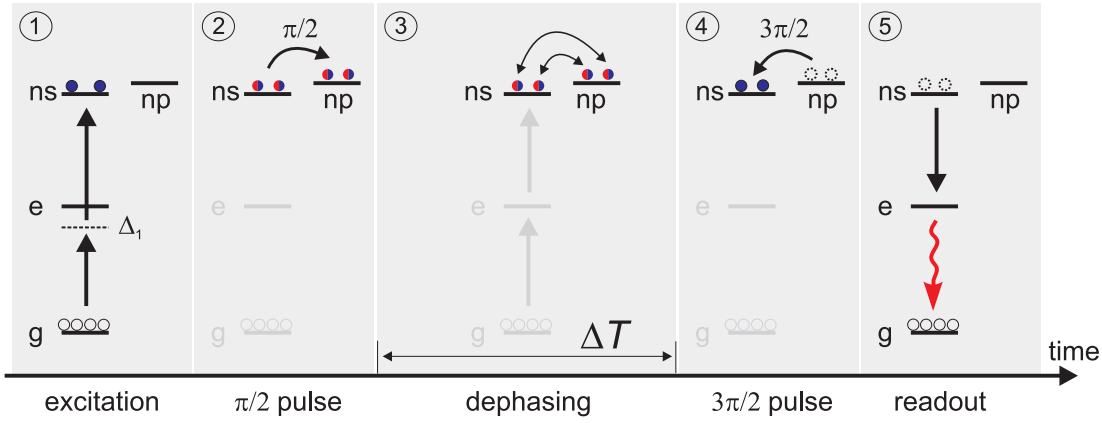

Figure 34: Timing sequence of the microwave dephasing protocol. Steps 1 though 5: 1) excitation to a Rydberg level $|ns\rangle$; 2) $|ns\rangle$ and $|np\rangle$ levels are mixed with a resonant $\pi/2$ microwave pulse; 3) interaction (dephasing) period; 4) $3\pi/2$ microwave pulse returns population to the $|ns\rangle$ state; 5) spin wave is readout with a resonant optical pulse.

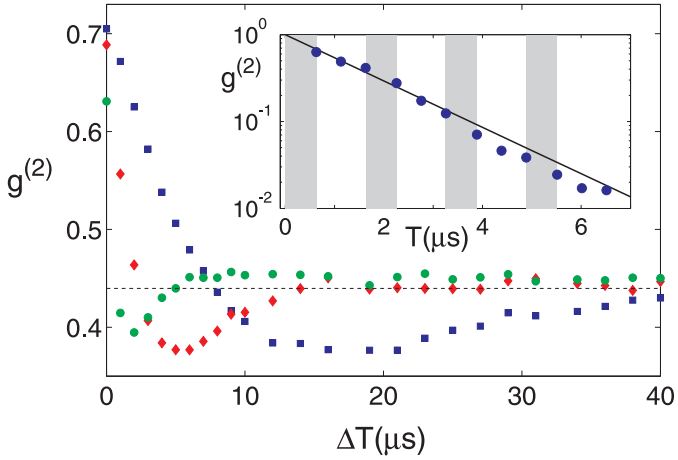

Figure 35: Decay of the correlation function $g^{(2)}$ in the phase-matched mode versus interaction time ΔT for a single Ramsey 2π-pulse cycle in the strong dressing limit for atoms excited into s states with principal quantum numbers 60 (blue squares), 79 (red diamonds), and 100 (green circles). Black dashed line represents the asymptotic limit $g^{(2)}(0)16/25$. Inset: effect of repeated cycles for $n = 100$ with microwave Ramsey sequence repeated with levels $100p_{1/2}$, $99p_{1/2}$, $100p_{3/2}$, and $99p_{3/2}$. Dark regions correspond to the duration of each 2π microwave pulse cycle.

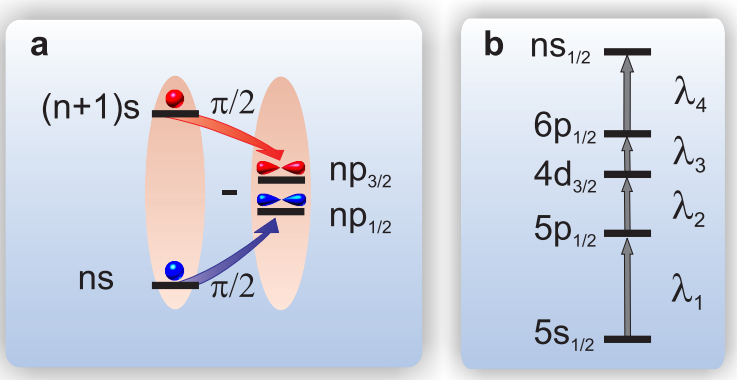

Figure 36: a) Atomic levels involved in entanglement of two spin-wave excitations via a protocol described in the text. b) Four-photon excitation of Rydberg spin waves in atomic Rb, with $(\lambda_1, \lambda_2, \lambda_3, \lambda_4)$=(795,1475,2294,1005)nm. Collinear and off-axis geometries lead to spin waves of period 50 μm, and ∞, respectively.

is sketched in Fig. 36(a). A pair of fast $\pi/2$ pulses couple $|ns\rangle$ and $|(n+1)s\rangle$ levels to $|np_{1/2}\rangle$ and $|np_{3/2}\rangle$ respectively, creating a superposition state $(|ns\rangle + |np_{1/2}\rangle)_a(|(n+1)s\rangle + |np_{3/2}\rangle)_b$. Cross terms $|ns\rangle_a|np_{3/2}\rangle_b$ and $|np_{1/2}\rangle_a|(n+1)s\rangle_b$ will dephase as they are subject to resonant dipole-dipole interactions. The resulting entangled state will be $\Psi = |ns\rangle_a|(n+1)s\rangle_b + |np_{1/2}\rangle_a|np_{3/2}\rangle_b$. The state $|\Psi\rangle$ may be mapped onto long-lived ground state coherences [32, 33] or optically retrieved, via s or d states, resulting in entangled polarization or time-bin qubits. Entangled pairs of long-lived qubits, or the atom-light qubit pair, can be used as building blocks in larger entangled systems, for example, in entanglement purification protocols [19, 20, 21].

4.3.3 Excitation of motion-insensitive spin waves

The motional dephasing of optical ground-Rydberg coherences has been a serious problem in exploiting Rydberg atom interactions [32, 33]. While atom trapping would in principle alleviate this effect, so far no effective Rydberg atom confinement schemes have been demonstrated, although there are promising works in that direction [98, 96]. For a cold magneto-optical trap of Rb the average atomic velocity $v \sim 0.1$ m/s, while the spin-wave grating period for two-photon excitation is only $\Lambda \sim 1$ μm, giving a

coherence time $\Lambda/(2\pi v) \sim 2$ μs. In order to overcome this limitation, we propose the four-photon excitation scheme shown in Fig. 36(b) for atomic Rb. In this case the four wave vector mismatch can be made equal to zero and the corresponding spin-wave period diverges, thereby eliminating motional decoherence. Since all the transitions involved possess strong dipole moments, the Rabi frequency can easily exceed several MHz with available laser powers. The advantage of the proposed scheme is that is can be used in collinear excitation geometry, which offers optical alignment simplicity, to produce large period (50 μm) spin waves. Alternatively one could use three-photon excitation scheme, but it would require large angles between excitation beams and more complex alignment.

CHAPTER V

EMERGENCE OF LONG-RANGE CORRELATIONS IN A COLD ATOMIC GAS

This chapter is based on Ref. [99].

5.1 Introduction

The interactions between atoms can be switched on and off using laser fields tuned to the frequency between the Rydberg level and the ground level. In an ensemble of atoms, such coherent driving generates collective Rydberg spin waves. Spin waves can be mapped onto light using quantum state transfer techniques. Subsequent photoelectric detection of the light permits one to extract their properties [63, 42, 16, 95, 100]. Crystals composed of many such spin waves can be generated dynamically by an adiabatic sweep of laser detuning through the so-called Rydberg stair-case, with the number of excited atoms determined by the sweep parameters [101, 102]. Recently, Ates and Lesanovsky have shown that an atomic gas undergoing continuous-wave, on-resonance Rydberg excitation develops long-range correlations arising from the interplay of atomic interactions and dynamic spin-wave generation [103]. In this work, a Rydberg spin wave is optically excited in a quasi-one-dimensional atomic sample of Rb atoms. By spatially selective conversion of the spin wave into a light field, we demonstrate that Rydberg-level interactions create long-range correlations of collective atomic excitations.

5.2 Experiment

5.2.1 Experimental setup

As a first step towards realizing such long-range order, and ultimately, crystallization, here I describe our observations of spontaneous localization of Rydberg spin waves excited in an ultra-cold atomic gas. A sample of ^{87}Rb atoms of peak density $\rho_0 \simeq 10^{12}$ cm^{-3} is prepared in an optical lattice (loading procedure is described in previous chapter). The lattice is shut off, and an ensemble is driven in two-photon resonance between the ground $|g\rangle = |5s_{1/2}\rangle$ and a Rydberg $|r\rangle = |102s_{1/2}\rangle$ level with a laser excitation pulse of duration $\tau = 200$ ns, see Fig. 37(a). The transverse size (Gaussian waists $w_x \approx w_y \simeq 6$ μm) of the Rydberg excitation region is determined by the overlap of the atomic sample and two-photon excitation laser fields Ω_1 (795 nm) and Ω_2 (475 nm), which are nearly-counterpropagating and parallel to z and linearly polarized along x. The longitudinal size (waist w_z variable between 10 and 60 μm) is determined by the sample size along z. The number of atoms N involved in the excitation is therefore $(1-5)\times 10^3$. The values of Ω_1 and Ω_2 are chosen such that the multi-atom pulse excitation area $\theta \equiv \sqrt{N}\Omega\tau \sim 1$, where $\Omega = \Omega_1\Omega_2/\Delta$ is the single-atom, two-photon Rabi frequency, and Δ is the laser detuning from the intermediate level $|e\rangle = |5p_{1/2}\rangle$. Since w_x and w_y are smaller than the effective atomic interaction range, quasi-1D spin waves can be realized for $w_z > w_x, w_y$. In the limit of instantaneous excitation ($\tau \to 0$), the spin-wave can be described by a coherent state $|\Psi_0\rangle = \sum_{\alpha=0}^{N} c_\alpha |\alpha\rangle$, where $|\alpha\rangle$ is the phased Dicke state containing α excitations [16]. For finite values of τ, Rydberg-level interactions suppress excitation of nearby atoms, resulting in reduction of amplitudes c_α for $\alpha \geq 2$.

5.2.2 Spin-wave evolution and readout

The collective multi-atom state evolves during the ensuing storage period of duration T_s. For T_s shorter than the motional dephasing time the spin-wave evolution is

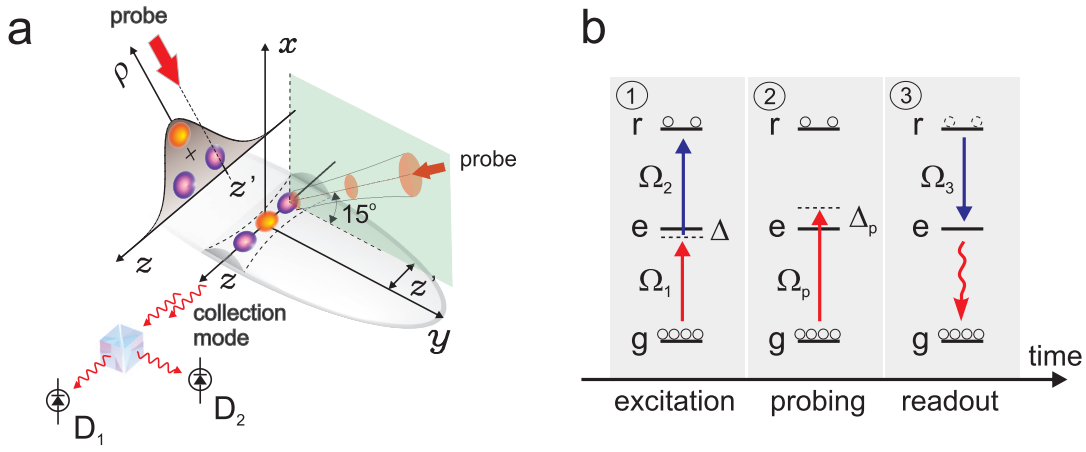

Figure 37: Essential elements of the setup. a) Experimental geometry: an atomic sample of temperature $T \simeq 10$ μK is produced in an optical lattice formed by a retro-reflected 782 nm laser beam propagating along the y-axis. The quantization axis is defined by a 4.3 G bias magnetic field along the x-axis. Localized spin waves are formed in the sample as a result of Rydberg excitation blockade and spin-wave dephasing. The spatial structure is revealed by scanning a focused waist of the probe beam along the $z-$axis of the two-photon excitation region. Either a single (orange) or double (blue) excitation is formed in an approximately Gaussian density profile ρ of the atomic sample. The probe beam destroys the phase-matched spin waves in a spatially-selective manner, affecting the statistics of the retrieved field. The latter is measured by a Hanbury Brown-Twiss type setup consisting of a beamsplitter and two single-photon detectors D_1 and D_2. b) Experimental sequence of spin-wave creation, probing, and retrieval.

dominated by the interactions of Rydberg atoms. As a result, the coherently excited sample undergoes an interaction-induced transition to a set of localized spin waves, each one containing no more than a single excitation. This may be viewed as spin-wave antibunching, in which the probability to have excitations in two different regions of the sample is suppressed for nearby regions.

The interaction is described by the following Hamiltonian:

$$\hat{H} = \sum_{\mu>\nu} \hbar \Delta_{\mu\nu} \hat{\sigma}_{\mu}^{rr} \otimes \hat{\sigma}_{\nu}^{rr},$$

with atomic operators for the atom μ defined as $\hat{\sigma}_{\mu}^{ab} = |a\rangle_{\mu}\langle b|$, where $a, b \in [g, r]$ with $|g\rangle_{\mu}$ being the atomic ground state and $|r\rangle_{\mu}$ being the addressed Rydberg level. The interaction-induced detuning $\Delta_{\mu\nu}$ is calculated using a single channel model [5]

$$\Delta_{\mu\nu} = \delta/2 - \sqrt{\delta^2/4 + (C_3/R_{\mu\nu}^3)^2},$$

where δ and C_3 are, respectively, the energy defect and the product of the dipole transition matrix elements for the strongest scattering channel from the excited Rydberg level to the neighboring Rydberg manifolds. $R_{\mu\nu}$ is the interatomic distance.

The spin wave is converted into a retrieved light field by a 1 μs long read-out field Ω_3 (475 nm), in resonance with the $|102s\rangle \leftrightarrow |5p_{1/2}\rangle$ transition. The retrieved field is coupled into a single mode fiber followed by a beam splitter and a pair of single-photon detectors D_1 and D_2. 840 ns-long detection time interval is determined by the length of the retrieved pulse. Both the excitation blockade and spin-wave dephasing should be reflected in the second-order intensity correlation function of the retrieved field at zero delay, $g^{(2)}(0)$, which is extracted from the statistics of the photoelectric detection events.

For a sufficiently small sample, the combination of excitation blockade and interaction-induced dephasing can completely suppress amplitudes for two and more excitations if the retrievable spin wave, realizing a source of single photons, for which the probability to detect more than one photoelectric detection event per pulse is strongly

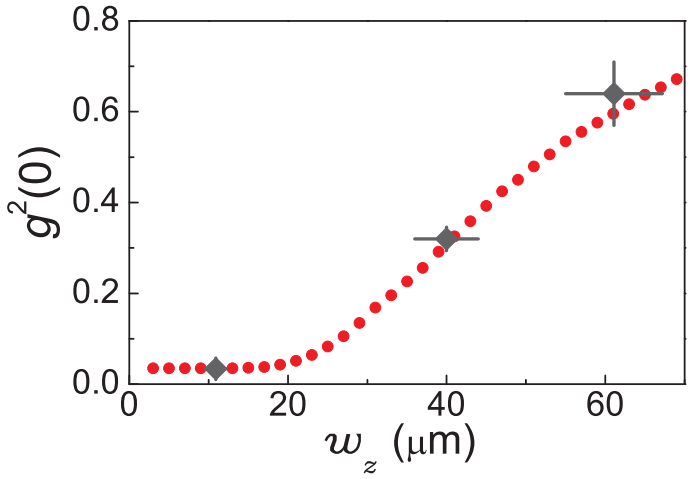

Figure 38: Second-order intensity correlation function $g^{(2)}(0)$ as a function of the sample length. Vertical error bars represent ± one standard deviation ($\sqrt{M}$) for M photoelectric counting events, while horizontal error bars represent the uncertainty in w_z. The filled circles are results of numerical simulations for transverse sample waists $w'_{x,y}$ =6.4 μm, with an additional contribution accounting for experimental dark detector counts and scattered light

suppressed, i.e., $g^{(2)}(0) \to 0$ [88]. The atoms perform the role of a quantum filter: after the (weak) coherent state of light is mapped onto atoms, Rydberg interactions remove from the spin-wave wavefunction, and hence from the wavefunction of the retrieved field, the components with more than one excitation (photon), while the vacuum and single-photon components pass through.

The $1/R^6$ scaling of the interaction strength in the van der Waals regime results in well-defined interaction volumes within the atomic sample. In this case, emergence of a spatial pattern of retrievable spin-waves is expected. The higher measured values of $g^{(2)}(0)$ for longer samples, Fig. 38, reflect the increase of the average number of surviving excitations.

5.2.3 Spatially selective readout

To look into the spatial structure of the spin wave, we illuminate it with a near-resonant 795 nm probe laser field Ω_p for 150 ns during the 0.5 μs time interval between

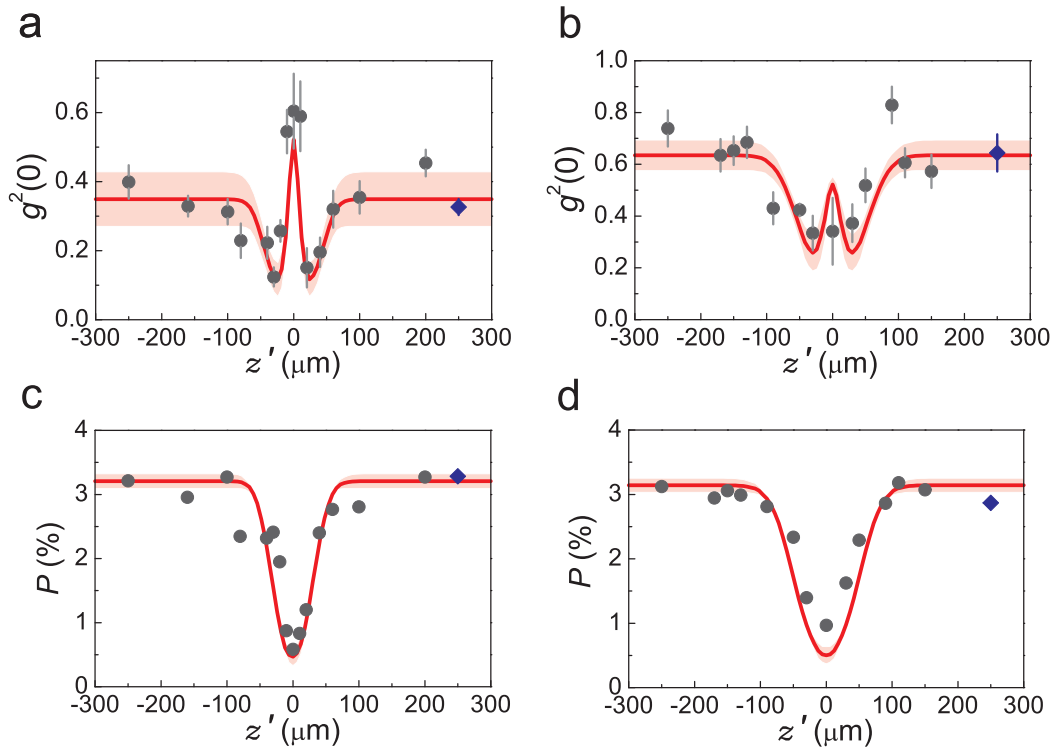

Figure 39: $g^{(2)}(0)$ (top panels) and probability of photoelectric detection for the retrieved field (bottom panels). Left panels are for $w_z = 42$ μm, right panels for $w_z = 64$ μm, with these values extracted by the fluorescence imaging of the atomic cloud. The solid curves are based on computer simulations with $w'_z = 42$ μm for left panels, and $w'_z = 64$ μm for right panels. The shaded regions are for a range of w'_z of 38 to 46 μm, and 58 to 70 μm for the left and right panels, respectively, while the results are only weakly sensitive to variation of w'_x and w'_y. Discrepancies that are larger than statistical uncertainties represented by error bars are attributed to the drift in optical alignment.

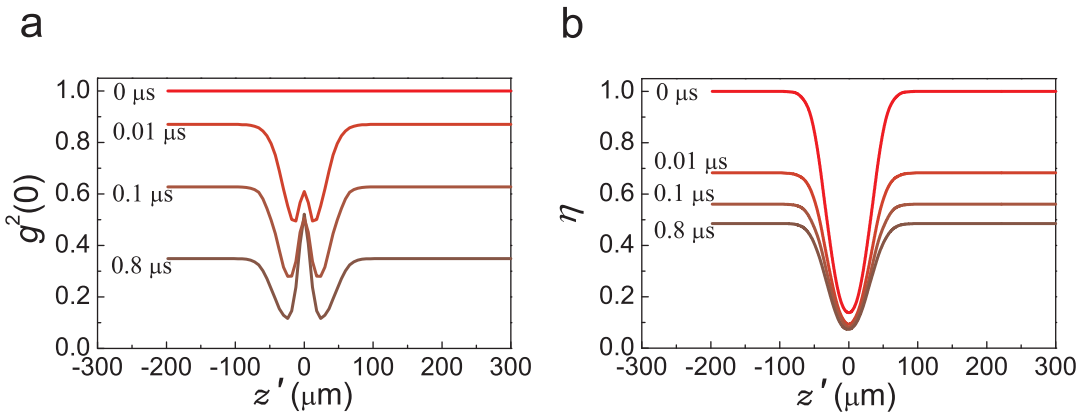

Figure 40: Numerical simulation of time-evolution of retrievable spin-wave excitations. a) Intensity correlation function at zero delay, $g^{(2)}(0)$. b) Intensity of the retrieved signal, η, both as a function of the probe beam position along the z-axis, for storage periods T_s up to 0.8 μs, with $w'_{x,y}$ =8 μm, and w'_z =42 μm.

the Rydberg excitation and readout stages, Fig. 37(b). The beam, focused down to a ≈ 10 μm waist ($1/e^2$ intensity) at the position of the sample, produces local dephasing of the spin wave via the associated inhomogeneous light shifts and spontaneous emission. The retrieved signal in this case corresponds to the spin-wave content of the part of the sample unaffected by the probe beam. By scanning the position of the probe beam z', it is, therefore, possible to reveal spatial spin-wave correlations. The scanning of the z-position of the probe beam is accomplished by moving the entire optical assembly, including a fiber which delivers light, on an automated translational stage.

Measured correlation functions and efficiencies are shown in Fig. 39. When the beam is sufficiently far from the sample so as not to affect it ($|z'| \geq 0.2$ mm), the measured values are consistent with those for no probe beam (the blue diamond in each panel). As the beam position starts approaching the sample (on the slope of efficiency curve), a notable decrease in $g^{(2)}(0)$ and efficiency is observed. In this case, the effective size of the sample is decreased and only one excitation is retrieved, as

evidenced by the low measured $g^{(2)}(0)$ values. When the beam is positioned in the center of the shorter ensemble (Fig. 39(a,c)), a prominent maximum in $g^{(2)}(0)$ is observed due to stronger suppression of singly-excited spin waves than of doubly-excited spin waves. The data clearly show high sensitivity of our technique, with the observed values of $g^2(0)$ varying by more than a factor of five when the probe beam is moved by ~ 30 μm. For the longer ensemble (Fig. 39(b,d)), the center peak is not as pronounced in the simulation, as a result of a higher average number of excitations, and is not evident beyond the statistical uncertainties of the data. The probe is detuned by $\Delta_p = +200$ MHz from the $5s_{1/2}, F = 2 \leftrightarrow 5p_{1/2}, F = 2$ transition and its power is 10 μW and 40 μW for the data presented in Fig. 39(a,c) and Fig. 39(b,d) respectively.

5.2.4 Influence of background counts

Here we consider the role of background photoelectric detection events in our experiment. In the ideal situation of linear mapping between the spin wave and the retrieved optical field, the measured value of the second order intensity correlation function at zero time for the retrieved field $g_i^{(2)}(0)$ would directly provide the value of the corresponding spin-wave correlation function, independent of the finite efficiencies for the mapping, field transmission, and photoelectric detection. In practice, however, background light and detector dark counts contribute to the the photoelectric detection probabilities, so that the measured value $g^{(2)}(0)$ will differ from the ideal quantity $g_i^{(2)}(0)$. Modeling the background in terms of a coherent field with average photon number B, we find that

$$g^{(2)}(0) = 1 + (g_i^{(2)}(0) - 1)(1 - \frac{B}{P})^2. \tag{13}$$

We vary the probability P of a photoelectric detection event by changing RF power of the gating AOM, Fig. 41(a). No probe beam is employed in these measurements.

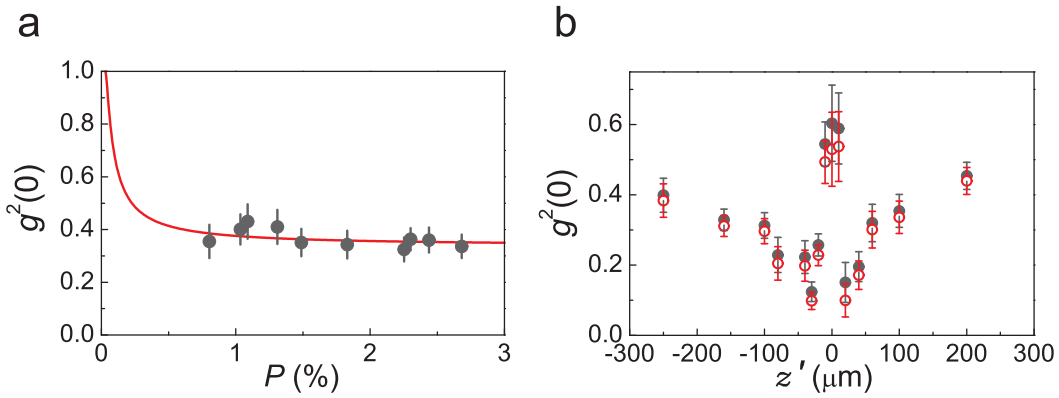

Figure 41: Influence of losses on $g^{(2)}(0)$. a) $g^{(2)}(0)$ as a function of photoelectric detection probability P that is varied by inserting partially transmitting optical filters into the retrieved field mode. The solid line is based on Eq. (13). b) $g^{(2)}(0)$ as a function of the probe beam position along the atomic sample z'. Filled circles (black) are for the case without subtraction of background counts (as in Fig. 39 of the main text) and open circles (red) are for the inferred values of $g^{(2)}(0)$ that would have been measured instead if there were no background counts.

The data show that over the dynamic range of our experiment the measured value of $g^{(2)}(0)$ is not significantly affected by linear losses. To further assess the influence of the background counts onto the observed spatial function data, in Fig. 41(b) we display both $g^{(2)}(0)$ and the inferred quantity $g_i^{(2)}(0)$. The latter values are somewhat lower when the probe beam is near the center of the sample, with the same functional dependence.

5.2.5 Numerical simulations

We performed numerical modeling of our experiment using 100 atoms randomly sampled according to a Gaussian density with transverse waists $w'_x = w'_y$ and longitudinal waist w'_z. We employ the Hamiltonian described below in the frozen-gas approximation. The second-order correlation function $g^2(0)$ computed using Eq. (14) of the next subsection is shown in Fig. 38 (dotted line) and agrees well with the measured values.

We simulate the action of the probe beam theoretically by transferring the atoms located in the part of the ensemble illuminated, into a state that is not retrieved via the optical read pulse. This selective transfer results in a modification of Eq. (14): the sums in the absolute value, both in the numerator and denominator, run only over N_A "retrievable" atoms and the single excitation probability is changed accordingly, $P_1 \rightarrow P_1(N_A/N)^2$. The theoretical results (the solid curves in Fig. 39) are in in good agreement with the experimental data, with the main features of the data being captured in the simulation. The computed retrieved signal exhibits a dip centered at $z' \approx 0$, i.e., with the probe beam focused onto the middle of the sample. As the probe beam is moved across the sample, $g^2(0)$ is decreasing, with the minimum values achieved when the beam is centered roughly on one of the halves of the sample. On the other hand, when the probe beam in focused into the middle of the sample, $g^2(0)$ is increased again and it reaches a peak whose value depends on the probe beam waist. We note that the good agreement between experiment and the theory is achieved even though our simulation does not account for the dynamical effects of the excitation blockade. This suggests that in our measurements dephasing of Rydberg spin waves is likely the dominant mechanism responsible for the observed long-range correlations.

5.2.6 Theoretical model

We employ the following Hamiltonian to model our system: $\hat{H} = \sum_\mu \hbar(\omega_g \hat{\sigma}_\mu^{gg} + \omega_r \hat{\sigma}_\mu^{rr}) + \sum_\mu \hbar(\Omega e^{-i\omega_L t}\hat{\sigma}_\mu^{rg} + h.c.) + \sum_{\mu>\nu} \hbar\Delta_{\mu\nu}\hat{\sigma}_\mu^{rr} \otimes \hat{\sigma}_\nu^{rr}$. The atomic operators for the atom μ are defined as $\hat{\sigma}_\mu^{ab} = |a\rangle_\mu\langle b|$, where $a, b \in [g, r]$ with $|g\rangle_\mu$ being the atomic ground state and $|r\rangle_\mu$ being the addressed Rydberg level. The two-photon excitation is modeled using the effective Rabi frequency $\Omega = \Omega_1\Omega_2/\Delta$ and the effective laser excitation frequency $\omega_L = \omega_1 + \omega_2$ obtained by adiabatically removing the intermediate excited state. The matrix elements in C_3 are calculated with a semiclassical approach.

This model results in a $1/R^3$ interaction strength at short distances which acquires the van der Waals $1/R^6$ dependence over distances $R > (C_3/\delta)^{1/3} \simeq 8\mu$m which correspond to the majority of the ensemble.

The driving laser fields are coupled to a spin wave whose creation operator is $\hat{S}^\dagger = 1/\sqrt{N}\sum_\mu e^{-i\vec{k}_0\cdot\vec{r}_\mu}\hat{\sigma}_\mu^{rg}$. The spin wave is characterized by its wavevector $\vec{k}_0 = \vec{k}_1 + \vec{k}_2$ defined by the excitation lasers: in the read process, this wavevector sets the phase matching condition that selects the retrieved excitations [16, 95]. The 2nd-order correlation function for the retrieved field at zero delay is defined as: $g^{(2)}(0) = \langle\hat{S}^\dagger\hat{S}^\dagger\hat{S}\hat{S}\rangle/\langle\hat{S}^\dagger\hat{S}\rangle^2$. Given an initial distribution of probability P_n at time $T = 0$ for the spin-wave Fock states, we find a correlation function, after a storage time T_s, [16]

$$g^{(2)} = \frac{\sum_{n\geq 2}\frac{P_n n(n-1)}{N^{n+2}}\sum_{\mu_1..\mu_{n-2}}\left|\sum_{\nu_1,\nu_2}e^{i\phi_{\mu_1\cdots\mu_{n-2}\nu_1\nu_2}}\right|^2}{\left[P_1 + \sum_{n\geq 2}\frac{P_n n}{N^{n+1}}\sum_{\mu_1..\mu_{n-1}}\left|\sum_\nu e^{i\phi_{\mu_1\cdots\mu_{n-1}\nu}}\right|^2\right]^2}. \tag{14}$$

The formula is valid for a distribution P_n that is peaked on a small number of excitations, $\langle n\rangle \ll N$.

5.3 Conclusion

In future it may be possible to observe the time evolution of the spin waves by achieving longer coherence times or/and higher temporal resolution of the excitation-probe-retrieval sequence. As an example, we show the computed second-order correlation function $g^2(0)$ and the intensity of the retrieved signal $\eta = \langle\hat{S}^\dagger\hat{S}\rangle$, normalized by its value when no probe beam is employed in Fig. 40 (a) and (b), respectively, for varying values of spin-wave storage time T_s. Both $g^2(0)$ and η decrease with T_s reflecting the growth of the Rydberg interaction volume. The peak of $g^2(0)$ at $z' \approx 0$ becomes prominent at $T_s \simeq 0.8$ μs when the spin-waves with more than two excitations have mostly dephased.

We have demonstrated emergence of spontaneous localization of collective atomic excitations in a strongly interacting atomic gas. Our work is performed in the regime

$\sqrt{N}\Omega\tau \sim 1$, whereas analysis of Ref. [103], predicting atom density correlations extending over lengths that are multiples of the Rydberg blockade radius, was done in the limit $\sqrt{N}\Omega\tau \gg 1$. In our measurements, the retrieved signal decays to zero in this limit [88], likely due to a combination of an inhomogeneous distribution of atom-light couplings and of finite laser linewidths. In the future, these limitations can be addressed, and the range of atomic correlations increased, by using a smaller atomic sample and employing lasers with narrower linewidths. Moreover, it is likely that the spin-wave coherence is considerably more sensitive than a single-atom coherence to these broadening mechanisms. Therefore, imaging techniques of the type described in Refs. [104, 105] may be advantageous for observing longer-range correlations and eventually large two- and three-dimensional Rydberg crystals. Such studies should bear on topics such as relaxation phenomena, translational symmetry breaking, and phase transitions in strongly-correlated liquid crystal, nematic, and supersolid systems.

CHAPTER VI

OBSERVATION OF COHERENT MANY-BODY RABI OSCILLATIONS

This chapter is based on Ref. [106]

6.1 Introduction

6.1.1 Collective Rabi oscillations

A two-level quantum system coherently driven by a resonant electromagnetic field oscillates sinusoidally between the two levels at frequency Ω which is proportional to the field amplitude [107]. This phenomenon, known as the Rabi oscillation, has been at the heart of atomic, molecular and optical physics since the seminal work of its namesake and coauthors [108]. Notably, Rabi oscillations in isolated single atoms or dilute gases form the basis for metrological applications such as atomic clocks and precision measurements of physical constants [109]. Both inhomogeneous distribution of coupling strength to the field and interactions between individual atoms reduce the visibility of the oscillation and may even suppress it completely. A remarkable transformation takes place in the limit where only a single excitation can be present in the sample due to either initial conditions or atomic interactions: there arises a collective, many-body Rabi oscillation at a frequency $\sqrt{N}\Omega$ involving all $N \gg 1$ atoms in the sample [110]. This is true even for inhomogeneous atom-field coupling distributions, where single-atom Rabi oscillations may be invisible. When one of the two levels is a strongly interacting Rydberg level, many-body Rabi oscillations emerge as a consequence of the Rydberg excitation blockade. In a seminal work Lukin and coauthors outlined an approach to quantum information processing based on this

effect [8]. In this chapter I present initial observations of coherent many-body Rabi oscillations between the ground level and a Rydberg level using several hundred cold rubidium atoms. The strongly pronounced oscillations indicate a nearly complete excitation blockade of the entire mesoscopic ensemble by a single excited atom. The results pave the way towards quantum computation and simulation using ensembles of atoms.

6.1.2 Rydberg blockade

A two-level quantum system coherently driven by a quasi-resonant electromagnetic field is one of the centerpieces of modern quantum physics [107, 109]. A wide array of two-level systems have been realized, with atoms, molecules, nuclei, and Josephson junctions being some of the prominent settings. More than half a century ago Dicke recognized that an atomic ensemble coupled to an electromagnetic field cannot always be treated as a collection of independent atoms [111]. His ground-breaking work gave rise to a rich field of collective atom-field interactions [112].

A key prediction of Dicke's theory is that under certain conditions atom-field coupling is enhanced by a factor $\sim \sqrt{N}$ when compared to one atom. Collectively-enhanced atom-field coupling has since been observed in a variety of settings involving either the emission or absorption of radiation. A coherent multi-atom Rabi oscillation at a frequency $\sqrt{N}\Omega$ is a particularly dramatic manifestation of quantum mechanics at work on mesoscopic scales, where an entire ensemble exhibits the dynamical behavior of a single two-level system. In 2001, Lukin *et al.* proposed to realize many-body Rabi oscillations in ensembles of atoms driven by a laser tuned to a Rydberg level and outlined protocols to realize scalable quantum gates for quantum computation and simulation and to generate highly entangled collective states for metrology beyond the standard quantum limit.

When an atom is promoted into a Rydberg level with principal quantum number

n, the valence electron is in an orbit that is $\sim n^2$ larger than that of the ground-level atom. The atomic dipole moment is correspondingly larger, so that the dipole-dipole interaction of two atoms is increased by $\sim n^4$ [113]. For $n \simeq 100$ the interactions are sufficiently strong that for two atoms separated by a distance ~ 10 μm the associated energy shift may prevent the second atom from being excited. The excitation blockade gives rise to an oscillation between the collective ground state $|G\rangle \equiv \prod_{i=1}^{N} |g\rangle_i$ and the state $|R\rangle \equiv 1/\sqrt{N} \sum_{i=1}^{N} |g\rangle_1 ... |r\rangle_i ... |g\rangle_N$ in which one of the N atoms is in the Rydberg level $|r\rangle$, with frequency $\sqrt{N}\Omega$ [8, 112, 114, 115, 94]. The average number $\langle N\rangle_r$ of atoms in level $|r\rangle$ is given by:

$$\langle N\rangle_r = \sin^2(\sqrt{N}\Omega t). \tag{15}$$

The result holds for an inhomogeneous distribution of atom-light coupling Ω_i with a modification $\sqrt{N}\Omega \rightarrow \sqrt{\sum_{i=1}^{N} \Omega_i^2}$ and $|R\rangle \rightarrow (1/\sqrt{\sum_{i=1}^{N} \Omega_i^2}) \sum_{i=1}^{N} \Omega_i |g\rangle_1 ... |r\rangle_i ... |g\rangle_N$. For two atoms the Rydberg blockade and the accompanying $\sqrt{2}$ enhancement of the Rabi oscillation frequency have been observed by Urban *et al.* [32] and Gaetan *et al.* [33]. Over the past decade there have been numerous studies of the many-atom Rydberg blockade, however none of them, without exception, demonstrated either a blockade by a single atom or the many-body Rabi flopping [5, 34, 35, 36, 37, 38, 116, 88].

6.2 Experiment

Here I describe observations of many-body Rabi oscillations of a mesoscopic ($a \simeq 15$ μm) ensemble of rubidium atoms in the regime of the Rydberg excitation blockade by just one atom. In order to achieve this, the interaction strength $\Delta E_B \equiv \Delta_{ij}(a)$ between a pair of atoms at a distance equal to the ensemble size a must be greater than the spectral width $\delta\omega$ of the exciting laser field. The duration of coherent atom-light interaction is limited to $\lesssim 2$ μs by the finite coherence time of the ground-Rydberg transition caused by atomic motion [88]. Therefore, we choose a high-lying Rydberg

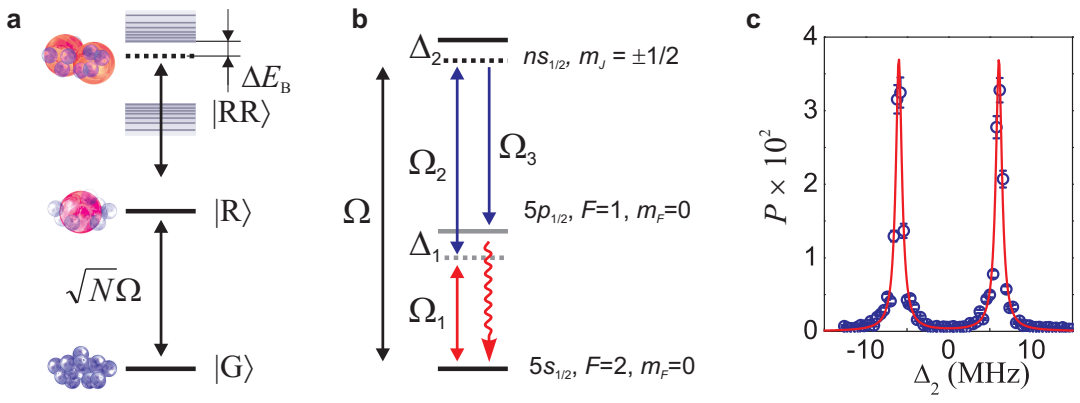

Figure 42: Rydberg excitation of an atomic ensemble. a) Illustration of the excitation blockade of more than one Rydberg atom in the ensemble. The coherent laser driving couples the collective ground state $|G\rangle$ and the state with one Rydberg atom $|R\rangle$ with Rabi frequency $\sqrt{N}\Omega$. The doubly excited states $|RR\rangle$ are shifted in energy out of laser resonance by the strong atomic interactions. b) Single-atom energy levels for ^{87}Rb. Electronic, hyperfine, and Zeeman quantum numbers are shown. The detuning from the intermediate $|5p_{1/2}\rangle$ level is $\Delta_1 = -40$ MHz. c) Probability P of photoelectric detection event per trial as a function of two-photon detuning Δ_2 for level $|102s_{1/2}\rangle$. It shows the two $m_j = \pm 1/2$ Zeeman components split by the bias magnetic field. The solid curve is a sum of two Lorentzian functions fit with the 0.9 MHz widths (fwhm) of the peaks determined by the 1 μs excitation duration.

level $|r\rangle = |102s_{1/2}\rangle$, for which $\Delta E_B \gtrsim 5$ MHz is sufficiently large.

6.2.1 Coherent excitation of a blockaded sample

The outline of the experiment is similar to the one described in the Chapter IV. A gas of ^{87}Rb atoms of temperature $T \simeq 10$ μK and of peak density $\rho_0 \simeq 10^{12}$ cm^{-3} is prepared in an optical lattice. The lattice is shut off, and the atoms are driven in resonance between the ground $|g\rangle = |5s_{1/2}\rangle$ and a Rydberg $|r\rangle$ level with the two-photon Rabi frequency $\Omega(\mathbf{r}) = \Omega_1(\mathbf{r})\Omega_2(\mathbf{r})/(2\Delta_1)$ for a duration $\tau = 1$ μs, with the corresponding single-atom excitation pulse area $\theta \equiv \Omega(0)\tau$, Figure 42 (a) and (b). The transverse size (Gaussian waists $w_x \approx w_y \simeq 6$ μm) of the Rydberg excitation region is determined by the overlap of the nearly counter-propagating two-photon excitation laser fields Ω_1 at 795 nm and Ω_2 at 475 nm. The longitudinal extent of the

ensemble is determined by the sample size of waist $w_z \approx 11$ μm along z.

Lasers of linewidths < 100 kHz are required to achieve coherent two-photon excitation for a duration of 1 μs. 475 nm field is produced by a power-amplified and frequency-doubled 950 nm ECDL and 795 nm light is derived directly from the 795 nm laser. To achieve narrow linewidths, both 795 and 950 nm lasers are stabilized using reflection from a high-finesse optical cavity, in contrast to methods described in Chapter IV, where 795 nm laser was stabilized to a saturation spectroscopy resonance and 950 nm laser was stabilized to a medium-finesse cavity. The new cavity has an ultra-low expansion glass spacer and is thermally stabilized, instead of the previously used Invar spacer-based cavity with a piezo element and stabilized with a laser locked to a rubidium line.

The measurement of the population of state $|r\rangle$ is achieved by the quantum state transfer onto a retrieved light field using a 1 μs long read-out field Ω_3 at 475 nm, in resonance with the $|102s_{1/2}\rangle \leftrightarrow |5p_{1/2}\rangle$ transition [63, 42]. The retrieved field is coupled into a single mode fiber followed by a beam splitter and a pair of single-photon detectors D_1 and D_2. Due to longer excitation (compared to Chapter IV) the single cycle of excitation and readout is extended from 2.5 μs to 3 μs. In addition, the total measurement time is decreased from 200 μs to 50 μs to alleviate the effects of atomic density variations due to the thermal expansion of the cloud.

6.2.2 Experimental data

Figure 43(a) shows the sum of the photoelectric detection event probabilities at the two detectors $P \equiv p_1 + p_2$ as a function of the single-atom Rabi angle θ, varied by changing the intensity of the Ω_1 field. The data are fit with the sinusoidal oscillation of Eq. (15) modified by two Gaussians. The choice of the fit function is motivated by a physical picture in which the visibility of the oscillation is smeared by fluctuations of the atom number and the intensities of laser fields Ω_1 and Ω_2,

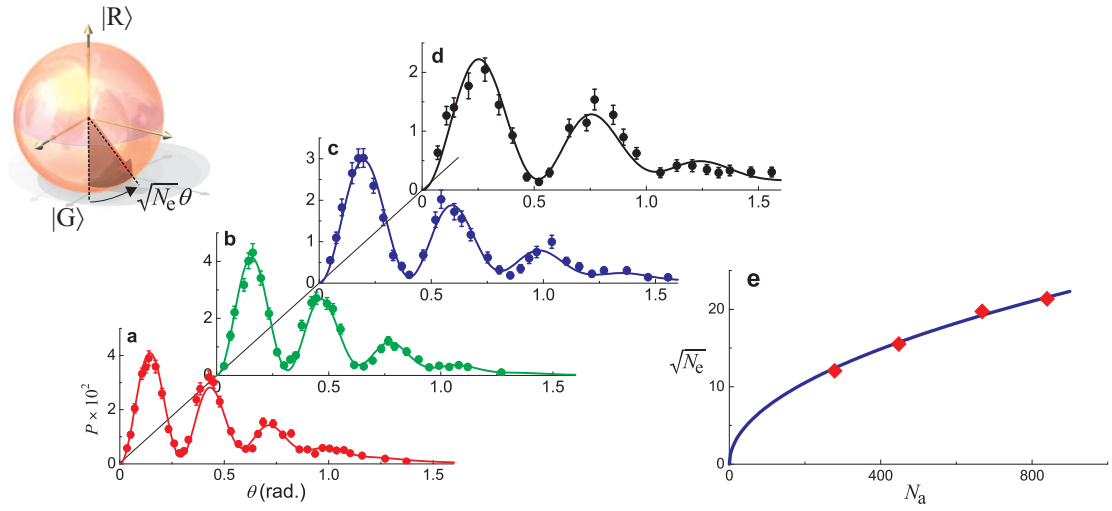

Figure 43: Coherent many-body Rabi oscillations of a mesoscopic atomic ensemble. In panels (a)-(d), probability of photoelectric detection P as a function of the single-atom Rabi angle θ is shown; upper level is $\left|102s_{1/2}\right\rangle$, excitation duration is $\tau = 1$ μs. Solid curves are fits of the form $P = \frac{1}{2}Ae^{-a\theta^2}(1 - e^{-b\theta^2}\cos(\sqrt{N_e}\theta))$. The fit parameters (A, a, b, N_e) were: $(4.3, 1.43, 1.70, 456)$ for (a), $(4.44, 1.43, 1.77, 397)$ for (b), $(3.24, 1.14, 0.72, 243)$ for (c) and $(2.56, 0.79, 0.86, 148)$ for (d). (e) $\sqrt{N_e}$ as a function of number of atoms N_a determined from fluorescence measurements. The data are fit with a function $C\sqrt{N_a}$, with the best-fit value $C = 0.74$. The inset shows a collective Bloch vector tipped by the angle $\sqrt{N_e}\theta$ on the unit sphere corresponding to the many-atom states $|G\rangle$ and $|R\rangle$. The error bars represent $\pm$ one standard deviation $(\sqrt{M})$ for M photoelectric counting events.

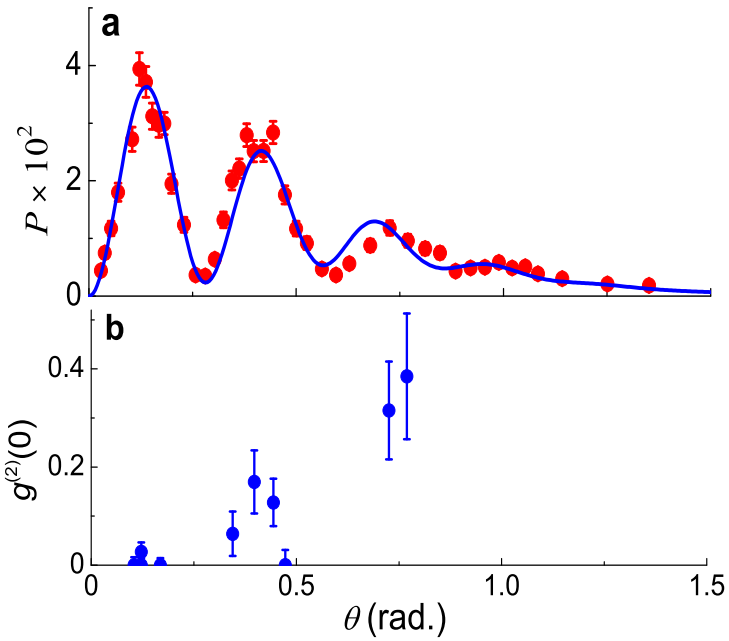

Figure 44: Probability of photoelectric detection P and second-order intensity correlation function at zero delay $g^{(2)}(0)$ as a function of the single-atom Rabi angle θ. Excitation duration is $\tau = 1$ μs and upper level is $\left|102s_{1/2}\right\rangle$. In panel (a) the solid curve is a fit as in Figure 43(a-d). The fit parameters (A, a, b, N_e) were $(3.80, 1.48, 1.86, 492)$. The error bars represent $\pm$ one standard deviation $(\sqrt{M})$ for M photoelectric counting events.

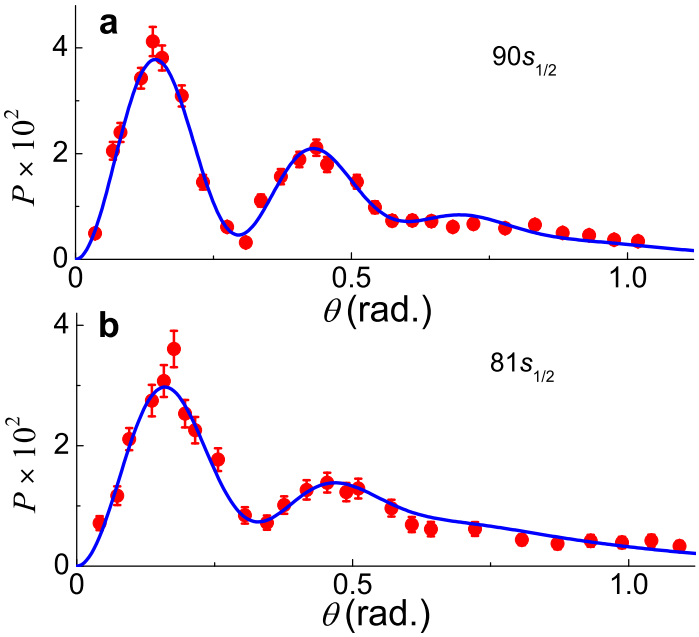

Figure 45: Probability of photoelectric detection P for as a function of the single-atom Rabi angle θ. Excitation duration is $\tau = 1$ μs. The solid curves are fits as in Figure 43(a-d), where the fit parameters (A, a, b, N_e) were $(4.10, 2.00, 3.52, 441)$ for n=90 in (a) and $(3.42, 1.62, 6.70, 335)$ for n=81 in (b), respectively. The error bars represent $\pm$ one standard deviation $(\sqrt{M})$ for M photoelectric counting events.

while the leading contribution to the overall decay of the retrieved signal, for the case when $\sqrt{N_e}\Omega_0 < \Delta E_B$, is due to an inhomogeneous distribution of light shifts for atoms in state $|R\rangle$, $\sim N_e\Omega_0^2/\Delta E_B$ which couple the state $|R\rangle$ to other singly-excited states. The effective number of atoms N_e is defined as $N_e \equiv \sum_{i=1}^{N} \Omega_i^2/\Omega^2(0)$. For our experimental geometry $\Omega_i^2 = \Omega^2(0)\exp(-2x^2/w_x^2 - 2y^2/w_y^2)$, and the atom density $\rho = \rho_0 \exp(-2z^2/w_z^2)$. Therefore $N_e = (\pi/2)^{3/2} w_x w_y w_z \rho_0$.

To explore the collective character of the observed Rabi flopping, we measure P as a function of θ while varying the peak density of the sample ρ_0, Fig. 43(b-d). Figure 43(e) shows the normalized frequency of the Rabi oscillation $\sqrt{N_e}$ extracted from the data in Figure 43(a-d) as a function of number of atoms in the ensemble N_a. The latter is calculated using peak density ρ_0 measured by the hyperfine state-selective fluorescence imaging of the atomic sample with magneto-optical trap cooling beams

used without a repumping field to exclude contribution of $|5s_{1/2}, F = 1\rangle$ atoms. The absence of additional peaks in Fig. 42(c) supports a near-unity value for the fraction of atoms f in the $m = 0$ Zeeman sub-level, with more quantitative measurements being currently under way. Ideally, we expect the effective atom number N_e extracted from the Rabi oscillation period to be equal to the atom number N_a determined by the fluorescence imaging of the sample, so that parameter C in the fit in Fig. 43(e) would equal unity. In addition to being modified by the factor $\sqrt{f}$, the most likely cause for $C = 0.74$ to be less than one is due to alignment imperfections and uncertainties in the determined waists of the two-photon excitation laser beams and in the fluorescence measurements of ρ_0.

We further confirm that the dynamics seen in Figure 43 correspond to the oscillation of Eq. (15) by measurements of the second-order intensity correlation function at zero delay $g^{(2)}(0)$ as a function of θ, shown in Figure 44. Measured values of $g^{(2)}(0)$ well below unity together with substantial visibility of the oscillations indicate that only one Rydberg excitation is present in the entire ensemble of several hundred atoms, which exhibits the behavior of a coherently driven two-level system. The measured values of $g^{(2)}(0)$ for $\sqrt{N_e}\theta \geq 5\pi$ in Figure 44(b) suggest that the contribution of populated doubly-excited states to extracted values of a is substantial. On the other hand, the sizable oscillation visibilities in Figure 43 indicate small population of the doubly-excited states for $\sqrt{N_e}\theta \approx \pi$, as the latter are expected to have a suppressed retrieval efficiency. Combining all the data points for $\sqrt{N_e}\theta \approx \pi$ in Fig. 43(b) we obtain $g^{(2)}(0) = 0.006(6)$, which to our knowledge is the lowest value for this quantity for any previously reported light source. It is consistent with a lower bound of $g^{(2)}_{bg}(0) = 0.012(2)$ due to background counts, of which about half are due to detector dark counts.

The importance of the condition $\Delta E_B \gg \delta\omega$ for observation of many-body Rabi oscillations is checked by reducing ΔE_B in measurements with $n = 90$ and $n = 81$,

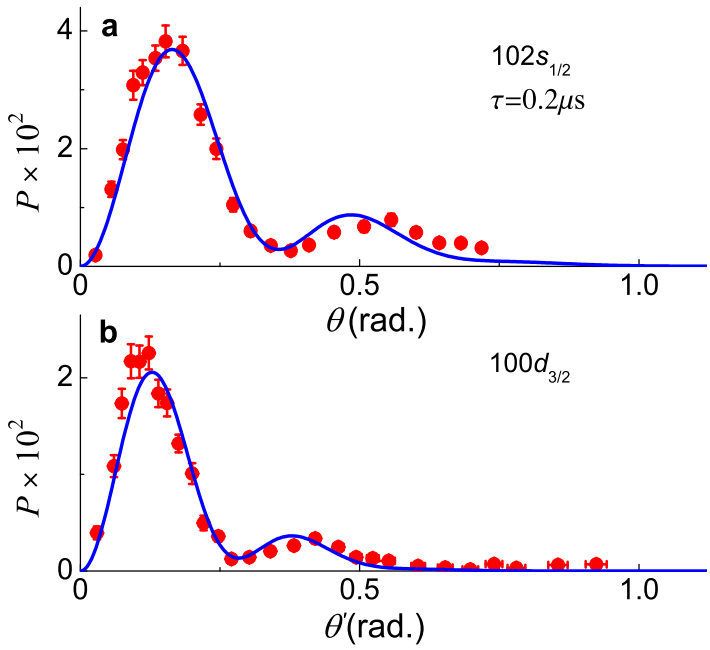

Figure 46: Probability of photoelectric detection P as a function of the single-atom Rabi angle θ. Level $|102s_{1/2}\rangle$ is excited for $\tau = 0.2$ μs in (a), and level $|102d_{3/2}\rangle$ is excited for $\tau = 1$ μs in (b). The solid curves are fits as in Figure 43(a-d), the fit parameters (A, a, b, N_e) were $(4.56, 5.27, 3.86, 340)$ in (a). The excitation spectrum for $|102d_{3/2}\rangle$ shows a complex structure due to an interplay of the bias magnetic field and an ambient electric field. For the data in (b), the laser is tuned to the strongest spectral component, with the scale θ' determined by using the value of $N_e = 492$ from the preceding measurements with the $|102s_{1/2}\rangle$ level, with a fit providing the value of peak single-atom Rabi frequency Ω_0 and the fit parameters (A, a, b) were $(2.58, 10.7, 3.49)$. The vertical error bars represent $\pm$ one standard deviation $(\sqrt{M})$ for M photoelectric counting events. The horizontal error bars in (b) reflect the uncertainty in determination of the x-axis scale θ'.

Fig. 45. Figure 46(a) shows data with increased $\delta\omega$ by using with shorter, $\tau = 0.2$ μs excitation. The oscillation visibility is clearly lower both for smaller ΔE_B, Figure 45, and larger $\delta\omega$, Figure 46(a). Figure 46(b) shows an oscillation with a similarly reduced visibility in measurements with the $|100d_{3/2}\rangle$ level with $\tau = 1$ μs excitation, which may be attributed to the blockade breakdown due to a strong angular dependence of the $|nd\rangle$-levels atomic interaction strengths [5]. It should be also noted that for a Gaussian distribution of atom-field couplings describing a laser beam exciting a large-extent gas in our experiment, the single-atom Rabi oscillations are almost completely washed out [117], which makes the observation of many-atom oscillations under these conditions even more remarkable.

We have demonstrated coherent many-body Rabi oscillations in an ensemble of several hundred cold rubidium atoms. The oscillations provide compelling evidence of the achievement of a collective Rydberg excitation blockade by a single excited atom. Our results pave the way for the realization of quantum simulators which employ qubits encoded in atomic ensembles, with fast two-qubit quantum gates mediated by strong Rydberg interactions [8, 12].

6.2.3 Decoherence model

We employ the following Hamiltonian to describe our system: $\hat{H} = \sum_\mu \hbar(\omega_g \hat{\sigma}_\mu^{gg} + \omega_r \hat{\sigma}_\mu^{rr}) + \frac{1}{2}\sum_\mu \hbar(\Omega_\mu e^{-i\omega_L t}\hat{\sigma}_\mu^{rg} + h.c.) + \sum_{\mu>\nu} \hbar\Delta_{\mu\nu}\hat{\sigma}_\mu^{rr} \otimes \hat{\sigma}_\nu^{rr}$. The atomic operators for the atom μ are defined as $\hat{\sigma}_\mu^{ab} = |a\rangle_\mu\langle b|$, where $a, b \in [g, r]$ with $|g\rangle_\mu$ being the atomic ground state and $|r\rangle_\mu$ being the addressed Rydberg level. The two-photon excitation is modeled using the effective Rabi frequency $\Omega = \Omega_1\Omega_2/(2\Delta)$. The interaction between Rydberg levels is described with a single-channel model.For $\Delta_{\mu\nu} \gg \Omega_\mu, \Omega_\nu \ \forall(\mu, \nu)$, the excitation blockade is operational. Adiabatic elimination of double and higher-order excitations from the equations of motion results in an effective Hamiltonian for the singly-excited part of the spectrum: $\hat{H}_{eff} = \sum_j \hbar\Delta_j|j\rangle\langle j| + \sum_{i>j} \hbar C_{ij}(|i\rangle\langle j| + |j\rangle\langle i|) +$

$\frac{1}{2}\sum_j \hbar\Omega_j(|j\rangle\langle G| + |G\rangle\langle j|)$. Here $\Delta_j = -\sum_{i\neq j}\Omega_i^2/(4\Delta_{ij})$, $C_{ij} = -\Omega_i\Omega_j/(4\Delta_{ij})$, where $|j\rangle$ is the many-body state with the j-th atom in the Rydberg level. The first two terms of the effective Hamiltonian are due to the light shifts induced by the (detuned) doubly-excited states onto the single excitations.

When the interaction-induced inhomogeneous light shifts are omitted, the Hamiltonian results in an ideal Rabi oscillation between the ground state $|G\rangle$ and the single spin wave $|R\rangle = (1/\sqrt{\sum_j \Omega_j^2})\sum_j \Omega_j|j\rangle$. If at time $t = 0$ the system is in state $|G\rangle$, the state at future times is given by $|\psi(t)\rangle = \cos(\Omega t/2)|G\rangle - i\sin(\Omega t/2)|R\rangle$. When the light shift terms are included, the state $|R\rangle$ is coupled to a broad distribution of singly-excited states and therefore leaks into this quasi-continuum, leading to $P \sim |\langle R|\psi(t)\rangle|^2$ decaying with a rate $\sim N_e\Omega_0^2/\Delta E_B$. The doubly-excited states are expected to be populated at a rate $\sim N_e\Omega_0^2$. Trial-to-trial fluctuations $\Delta\Omega$ and ΔN_e in N_e and Ω_0, respectively, lead to a decay of the oscillation visibility. The probability of photoelectric detection per trial P as a function of θ in Figures 43-46 is therefore fit by a function $\frac{1}{2}Ae^{-a\theta^2}(1 - e^{-b\theta^2}\cos(\sqrt{N_e}\theta))$, where dimensionless fit parameters $a \sim N_e$ and $b \sim (\Delta\Omega/\Omega_0)^2 + (\Delta N_e/2N_e)^2$ describe the roles of the light shifts and population of doubly-excited states, and atom number and intensity fluctuations, respectively, while an amplitude A represents the overall measured retrieval and detection efficiency.

CHAPTER VII

CONCLUSION

We have presented new methods for realizing the long-term storage of quantum information with atomic ensembles confined in optical lattices. A spin wave entangled with an optical field was stored for 3.3 ms by encoding the qubit into long-lived ground state coherences of ^{87}Rb with reduced sensitivity to the magnetic field [45]. Quantum memory lifetimes were limited to a few ms by inhomogeneous differential ac-Star shifts due to optical trapping potentials [44, 45]. We have extended memory lifetime up to a few hundreds ms by using laser-induced two-photon compensation [6] and the magnetic dressing of trapping potentials [68].

Along with long lifetimes our group has developed an efficient telecom wavelength interface for long-lived quantum memories, extending the effective communication range by an order of magnitude. We have shown quantum correlations between a telecom-wavelength field (1367 nm) and a spin wave preserved for 11 ms [6], limited by the data acquisition rate. As the next step we have demonstrated entanglement between a telecom-wavelength field and a long-lived qubit encoded into two spatially distinct spin waves, each based on the clock transition between ground state hyperfine levels, and stored for a 10 ms time period that was limited by the data acquisition rate [69]. Entanglement between an infrared (795 nm) field and the spin wave was confirmed for a 100 ms storage period.

In previous experiments atomic losses from the dipole trap due to collisions with room temperature background atoms were setting an upper bound for the longest possible memory lifetime. To offset this limitation we have constructed a differentially pumped ultra-high vacuum chamber with high-pressure section operating as a cold

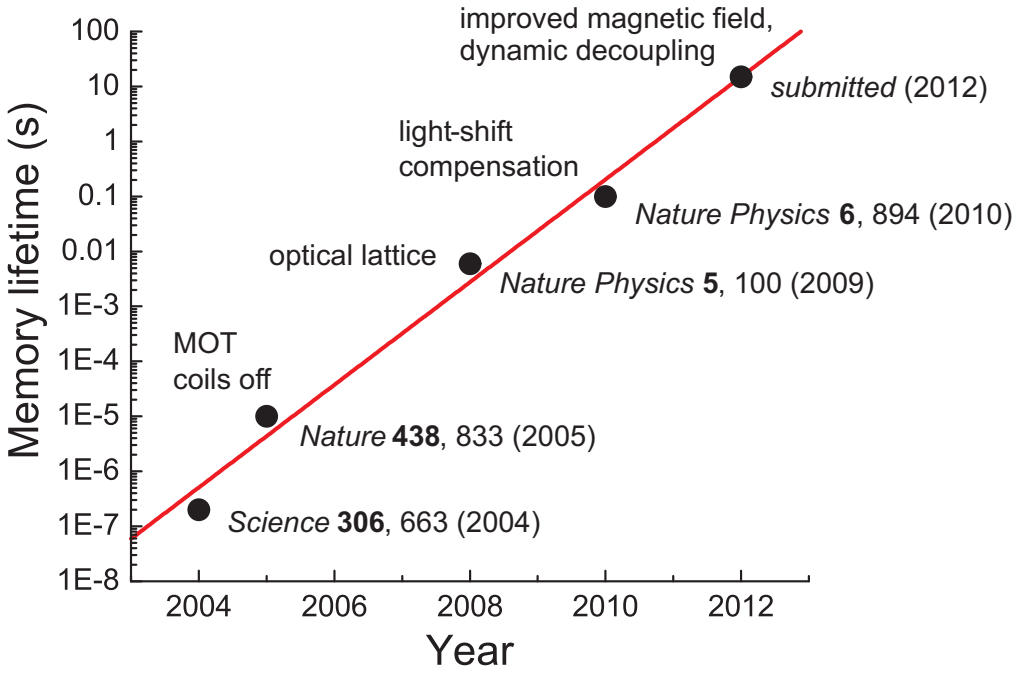

Figure 47: Quantum memory lifetime progress in our group. The data points are labeled with critical improvements and publication references. The solid line is to guide the eye.

atom source and a low-pressure experimental section reaching $\sim 10^{-11}$ Torr. In this new system we have realized a coherent optical memory with a 16 s $1/e$ exponential lifetime [30]. A similar order of magnitude lifetime is fully expected for quantum spin waves as well. Fig. 47 summarizes our group's progress in developing ensemble-based quantum memories over the past eight years.

Ultra-cold Rydberg gases are an emerging new paradigm in quantum optics and quantum information science. In this work we have realized the first basic step - the deterministic creation of single collective excitations in a mesoscopic ensemble of atoms. We have proposed [16] and demonstrated [88] a new mechanism of single photon generation based on the dephasing of multiply excited spin waves, which is complimentary to the Rydberg blockade. In its very first experimental realization the

Rydberg atom based single-photon source demonstrated excellent performance. With improved parameters it would become a valuable element of a quantum network.

With the improved linewidth of the excitation lasers we directly observed multi-atom Rabi oscillations in the presence of the excitation blockade [106]. For an extended, quasi 1D, geometry of the atomic sample we observed spatial correlations between localized Rydberg spin waves [99]. The results of this work pave the way for the next generation of experiments aimed at the synthesis of complex quantum states of matter and light and for the study of strongly correlated quantum systems. The immediate future of this project includes the implementation of a photon-photon gate that would rely on strong state-dependent interactions between Rydberg atoms. If realized, such a gate will become an experimental demonstration of text-book quantum optics and bring optical quantum information processing one step closer to practical scalability.

APPENDIX A

931 NM LASER SYSTEM

The 931 nm laser system is shown in Fig. 48. An extended cavity diode laser (ECDL) provides $\sim$ 40 mW at 931 nm and seeds it into a tapered amplifier (TA), which generates $\sim$ 600 mW. A small part of this light is split with a polarizing beam splitter (PBS), and sent through an acousto-optic modulator (AOM) in the double-pass configuration to shift the frequency, and then into a two-photon spectroscopy cell. A fraction of the dipole trap laser light is sent into the spectroscopy cell as well, although in the counterpropagating direction. Together the two laser fields drive two-photon transition $5S_{1/2}, F = 1 \leftrightarrow 6S_{1/2}, F = 1$.

An atom with velocity projection v on the axis along the 1064 nm beam (Fig. 48) will "see" a Doppler frequency shift $\mathbf{k}_{1064} \cdot \mathbf{v}$ for the 1064 nm beam and $\mathbf{k}_{931} \cdot \mathbf{v}$ for the 931 nm beam. Since $\mathbf{k}_{1064}$ and $\mathbf{k}_{931}$ have very similar magnitudes and opposite directions, the two Doppler shifts cancel each other to a large degree. Therefore for a Doppler broadened collection of atoms, the majority will contribute to the two-photon resonance signal when 1064 nm and 931 nm beams are counterpropagating.

Because of the large one-photon detuning from the D-lines the two-photon resonance was best observed by fluorescence on the D-lines, as opposed to absorption. With 0.7 W of 1064 nm light and 50 mW of 931 nm light used, both of the beams were focused to $1/e^2$ waists of 100 μm at the center of the cell to obtain sufficient two-photon Rabi frequency. To further increase the fluorescence signal the cell was heated in an oven to $\sim$ 200 C°. This was a value measured by a thermocouple placed on the side of the cell, whereas the rubidium concentration was determined by the somewhat colder temperature of the cell's appendix. To suppress background laser

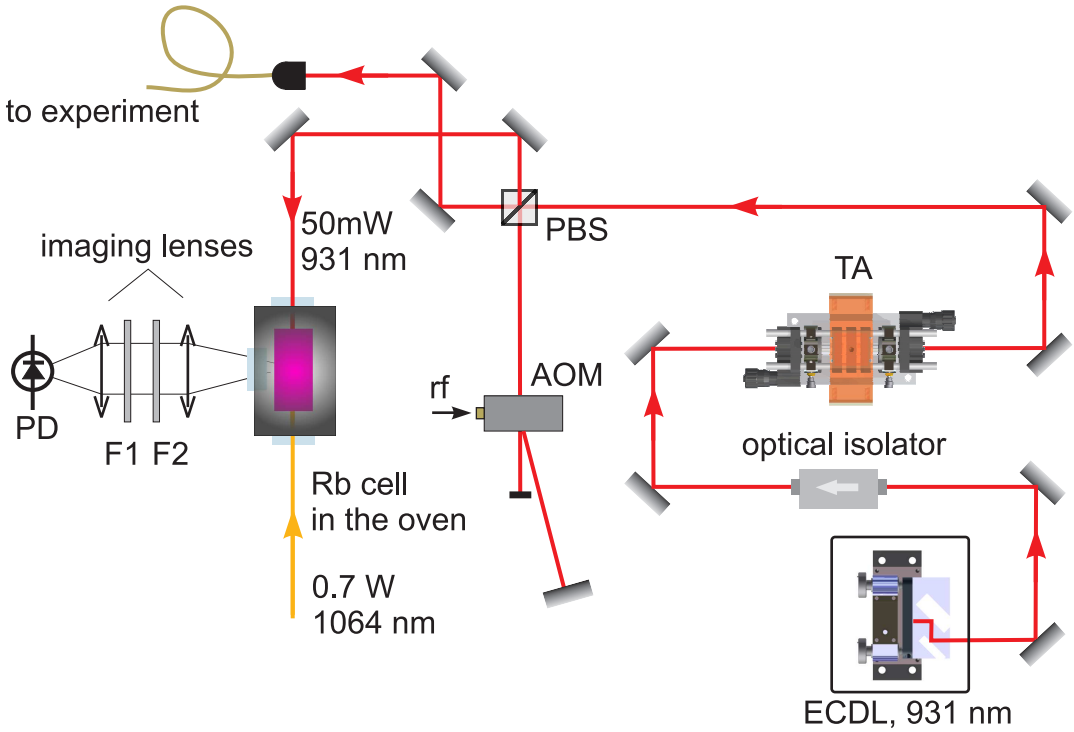

Figure 48: 931 nm laser system.

scattering fluorescence was collected from the central region of the cell where the beams were focused using imaging lenses shown in Fig. 48. In addition, optical filters F1 (Semrock 794/160 bandpass) and F2 (Newport 10SWF-900 short-pass) were placed between the lenses to suppress the background scatter. The fluorescence signal was used to create a feedback signal supplied to the current and the piezo voltage of the 931nm ECDL.

APPENDIX B

2D$^+$-MOT COLD ATOM SOURCE

In our previous work [68] memory lifetime had two major limitations: magnetic decoherence and trap losses. While the former could be circumvented by improving the magnetic environment around the atomic sample, the latter is ultimately limited to a few seconds by trap losses due to collisions with background atoms. Typically background pressure is dominated by room temperature rubidium vapor from which MOT is loaded. A general strategy to solve this problem is to replace room temperature vapor with a cold atom source. Variations include a double-MOT [118], a low-velocity intense source of atoms [119], a Zeeman slower [120], and a 2D-MOT [121]. The operational idea common to all of the mentioned sources (somewhat different for the Zeeman slower) is that the vacuum apparatus is separated into two sections. Atoms are captured from a warm atomic vapor and cooled in the high-pressure section and then transferred to the low-pressure section, where they captured in a 3D-MOT. Pressure difference of a few orders of magnitude between the sections is easily achievable because only a connection with a small conductance is required for cold atoms to pass from one section to another.

We picked the 2D$^+$-MOT configuration because of good atomic fluxes reported in the literature and the simplicity of the design. Our design was inspired by Ref. [122] and ideas from Chris Hamley. The vacuum system is shown in Fig. 49. A square glass 2D$^+$-MOT chamber (Allen Scientific Glass) is mounted on a 2.5" octagon from Kimball Physics which is connected to low-pressure section through a bellow for alignment purposes. The high-pressure section is pumped by an 8 l/s ion pump. A rubidium ampule is connected via a right-angle valve which provides a desired

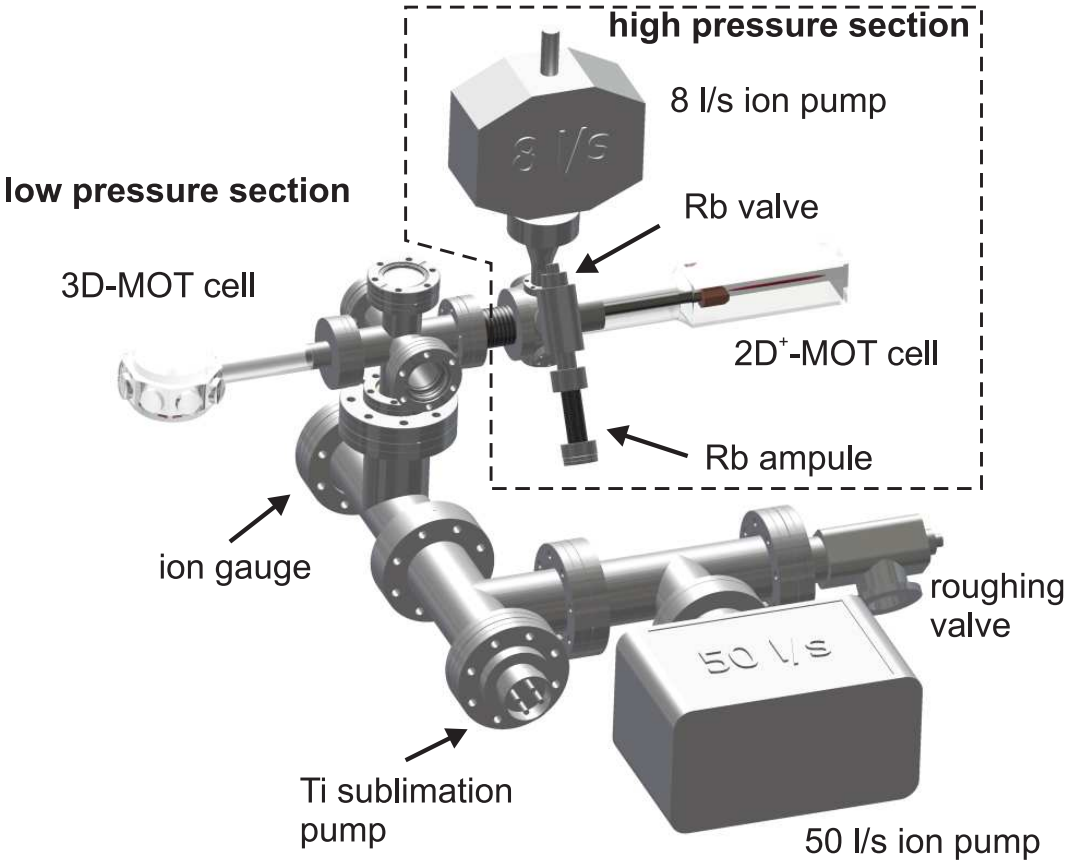

Figure 49: A differentially pumped vacuum system.

rubidium concentration.

The 3D-MOT chamber is a quartz octagon with optical quality AR-coated windows (Precision Glassblowing). The pressure in the 3D-MOT section is maintained by a 50 l/s ion pump in combination with a Ti-sublimation pump. A nude ion gauge is used to monitor pressure.

The differential pumping arrangement is shown in detail in Fig. 50. A copper rod is cut at 45-degrees and has a 2 mm diameter, 25 mm long hole through which cold atoms fly towards the 3D-MOT. The conductance of the hole is only 0.02 l/s which allows for a large pressure difference between the high- and low-pressure sections. The copper rod is held by a stainless tube which is mounted on a tube holder. The tube holder is mounted with zero (within machining tolerances) spacing from a copper blank plate which separates the two sections. The blank plate has a 1/4" diameter hole in the center.

Two pairs of racetrack-shape coils are used in an anti-Helmholtz configuration for the $2D^+$-MOT with electrical currents shown in Fig. 51. Two elliptical cross section transverse cooling beams are reused as shown, which eliminates the need for quarter-wave plates or prisms. The 45-degrees cut and hand-polished copper rod serves as a mirror for the retarding beam (Fig. 51) which is counterpropagating with respect to the pushing beam. The transverse beams are circularly polarized, while the pushing and retarding beams have orthogonal linear polarizations. The intensity balance between the transverse beams together with separate current control for each coil allows for precise alignment of the atomic beam through the aperture. Balance between the pushing and the retarding beams together with laser detuning is used to optimize the loading rate of the 3D-MOT.

For the 3D-MOT, three mutually perpendicular retro-reflected circularly polarized beams are used in combination with a pair of coils in an anti-Helmholtz configuration.

The entire low-pressure section, with the exception of the glass cell, was baked

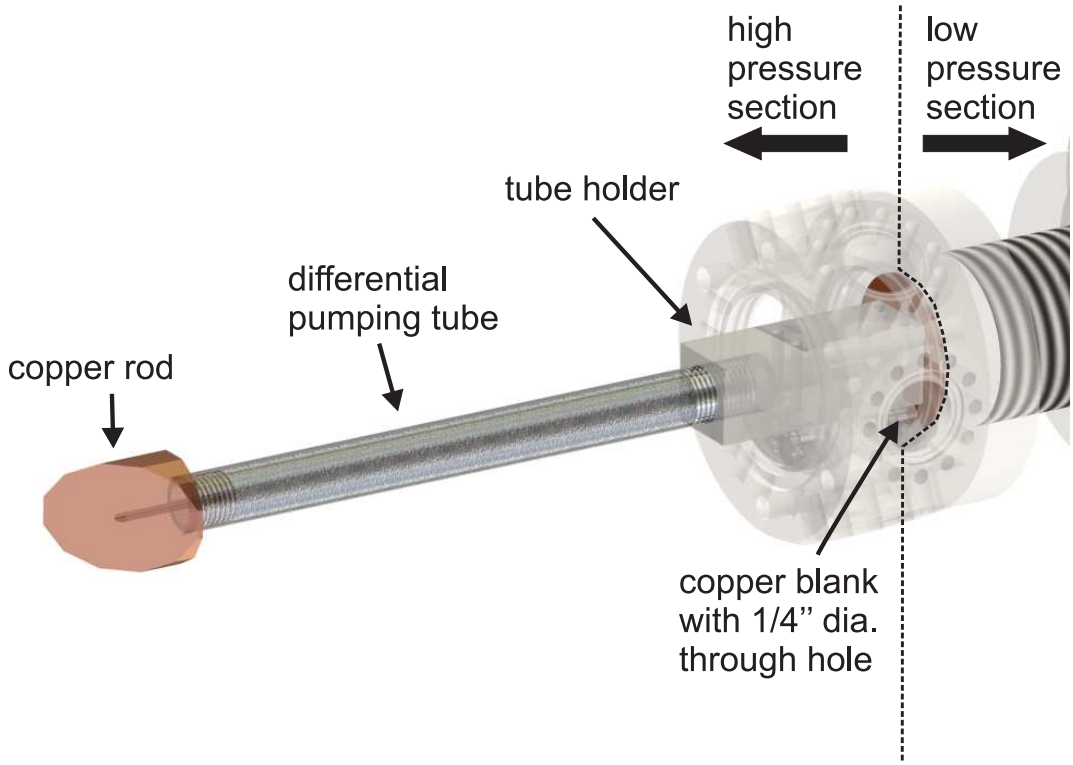

Figure 50: The differential pumping arrangement in detail.

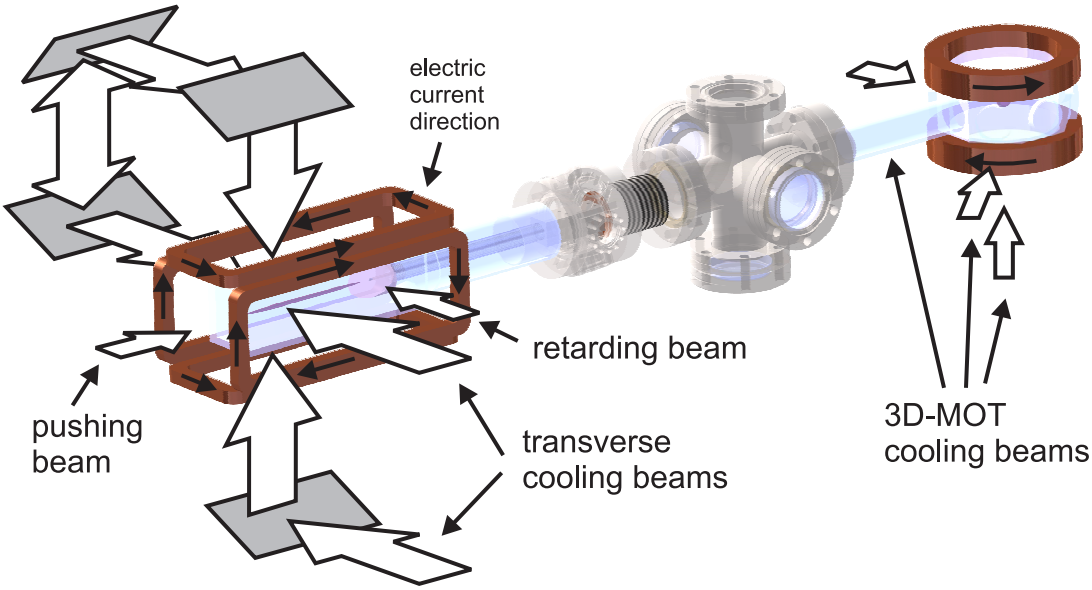

Figure 51: A sketch showing the geometry of the cooling and trapping beams for the $2D^+$-MOT and the 3D-MOT.

at above 350 C° for about a week. After the first bake the glass cell and the high-section pressure section were added and the whole system was baked again, but at lower temperature. After the bake the ion pumps and the Ti-sublimation pump were activated. The final pressures were $\sim 3 \cdot 10^{-11}$ (from the ion gauge reading) and $\sim 10^{-10}$ Torr (from the ion pump current reading) for the low- and high-pressure sections, respectively. The latter increased after the rubidium ampule was broken. The optimal operational pressure for $2D^+$-MOT was found to be around 10^{-8} Torr.

APPENDIX C

475 NM LASER SYSTEM.

To provide fast excitation of highly lying Rydberg states we used two-photon resonance through the D1-line. The 795 nm light was generated by an ECDL locked to a sub-Doppler resonance on the $5S_{1/2} \leftrightarrow 5P_{1/2}$ transition in a rubidium vapor cell. The 475 nm light to address the $5P_{1/2} \leftrightarrow nS_{1/2}$ or the $5P_{1/2} \leftrightarrow nD_{3/2}$ transition was generated by a frequency doubling of the 950 nm laser light. Here n is the principal quantum number of the Rydberg level.

The 475 nm laser system is shown in Fig. 52. An extended cavity diode laser (ECDL) generated $\sim$ 40 mW of 950 nm light which seeded a tapered amplifier (TA) providing $\sim$ 1.2 W of light. A fraction of the light was split after the laser to a transfer cavity to stabilize the wavelength and to a wavemeter (Burleigh WA 1000) to monitor the wavelength. Light after the tapered amplifier was frequency doubled by a commercial doubler (Spectra-Physics WaveTrain) which produced a maximum of $\sim$ 120 mW at 475 nm. Two acousto-optic modulators (AOMs) were used to create excitation and retrieval pulses coupled to the same single-mode fiber. Driving rf frequencies of two AOMs were different by 40 MHz to shift the frequency of the excitation beam off the single-photon resonance by 40 MHz.

To be able to stabilize 950 nm laser frequency at the value corresponding to a two-photon resonance we used an optical transfer cavity as shown in Fig. 53. The Fabry-Perot cavity consisted of two concave mirrors (radii of curvature 25 cm) with a broadband dielectric reflecting coating (finesse $\simeq$ 300). The mirrors were separated by a 8.9 cm long Invar spacer and a 1.3 cm long piezo ring. The cavity was assembled inside a 1" diameter lens tube and placed inside the vacuum chamber, which was

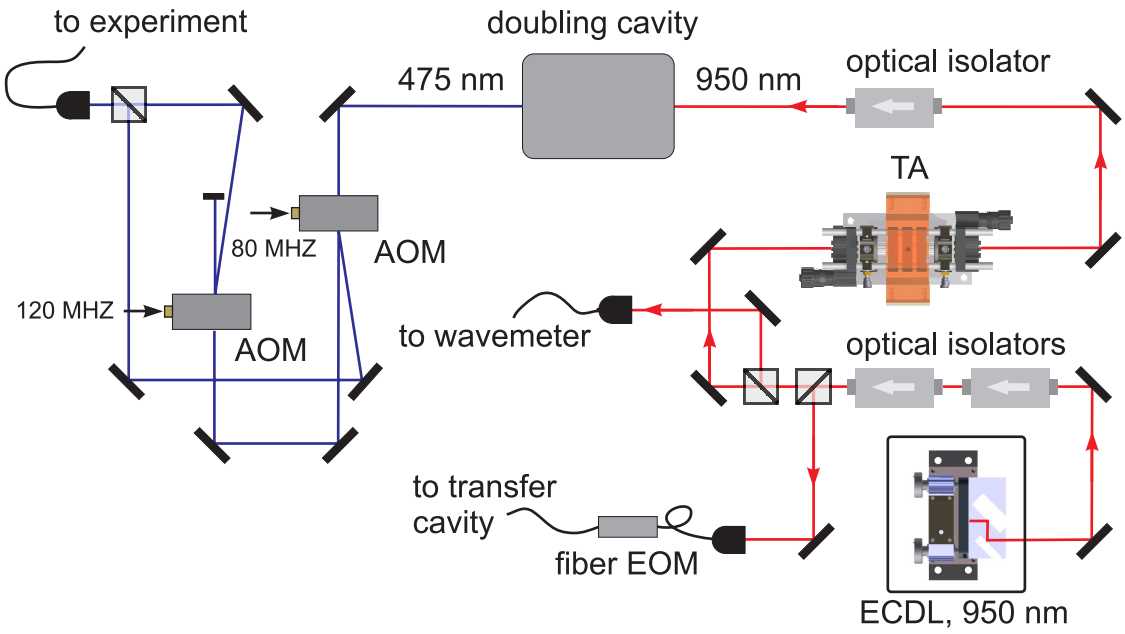

Figure 52: 475 laser system.

pumped down to $\sim 10^{-7}$ Torr and sealed in order to minimize the influence of the atmosphere.

The cavity length was actively stabilized with the help of a transmission signal of 780 nm laser light. The laser was stabilized to the rubidium D2-line. In order to unambiguously identify a particular longitudinal mode every time, transmission of an auxiliary 767 nm laser beam was monitored. The frequency of 767 nm laser was locked to the potassium D2 line. Fig. 54 shows transmission of the 780 and 767 nm beams as a function of the cavity length, which was scanned by a piezo. For every transmission peak of 780 nm light the frequency interval to the closest transmission peak of 767 nm light was different due to the wavelength difference, therefore it was possible to identify a particular longitudinal mode of the cavity by scanning the length and monitoring the mode structure for the two different wavelengths.

The frequency of the 950 nm laser was locked to a transfer cavity transmission signal using the Pound-Drever-Hall technique [123]. A fraction of the laser light

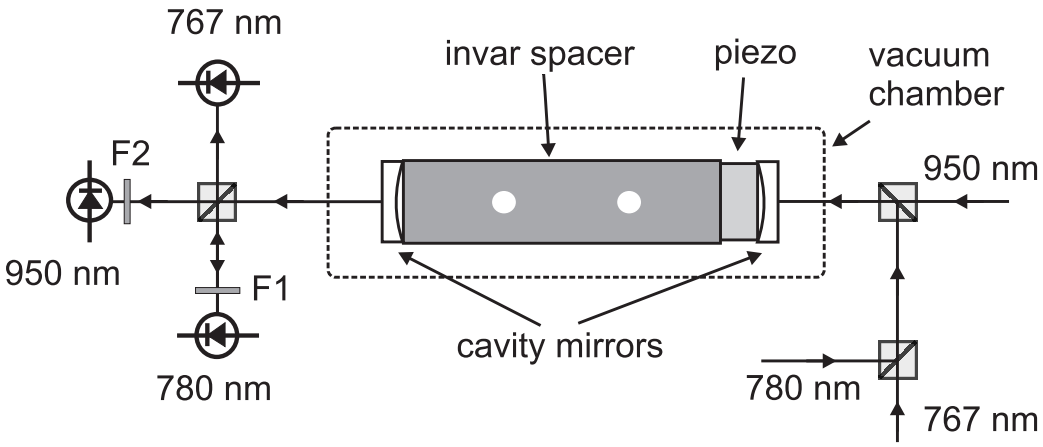

Figure 53: Transfer cavity. Three wavelengths were combined by polarization beam splitters. To separate the wavelengths after the cavity a polarization beam splitter in combination with optical filters F1 (780 center wavelength 5 nm bandpass) and F2 (850 nm longpass) were used.

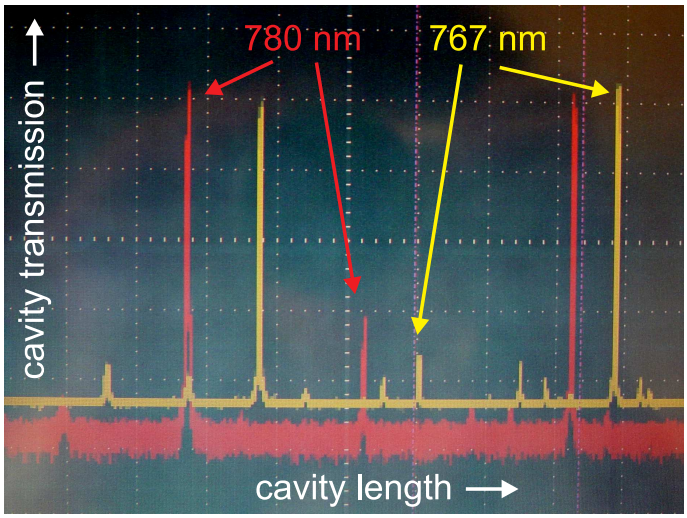

Figure 54: A photograph of the cavity transmission recorded on an oscilloscope.

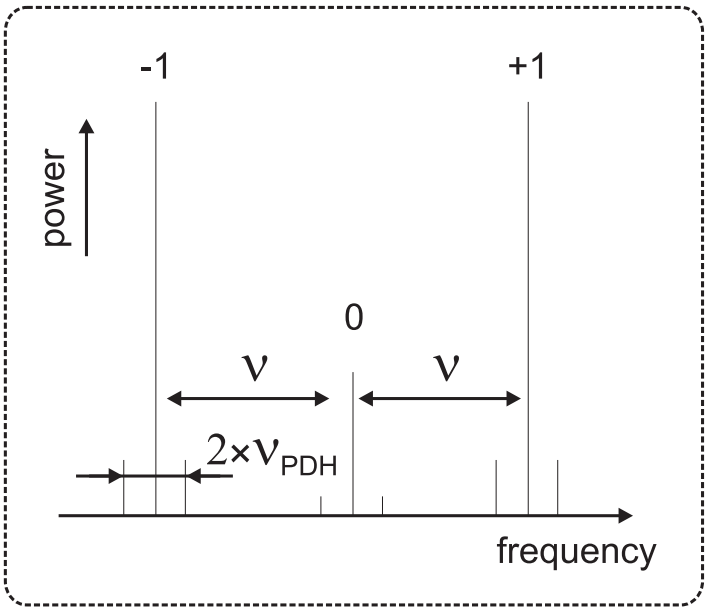

Figure 55: Illustration of an optical spectrum produced by an EOM driven with two frequencies.

was sent through a fiber-based high-bandwidth phase modulator before the cavity. The modulator was fed by two rf frequencies ν and ν_{PDH} combined by a power combiner. The resulting optical spectrum is shown in Fig. 55. High-amplitude first-order sidebands ("+1" and "-1" in the figure) are a result of the modulation at the frequency ν and the smaller sidebands around the large ones and the fundamental are results of modulation at the lower frequency ν_{PHD}. Modulation at ν_{PHD} (typically between 6 and 10 MHz) was used to lock the laser at either negative or positive first sideband produced by modulation at ν. Precise tuning of the laser was accomplished by changing ν.

REFERENCES

[1] S. Kuhr, W. Alt, D. Schrader, I. Dotsenko, Y. Miroshnychenko, A. Rauschenbeutel, and D. Meschede, "Analysis of dephasing mechanisms in a standing-wave dipole trap," *Phys. Rev. A* **72**, 023406 (2005).

[2] L.-M. Duan, M. D. Lukin, J. I. Cirac, and P. Zoller, "Long-Distance Quantum Communication with Atomic Ensembles and Linear Optics," *Nature* **414**, 413 (2001).

[3] D. N. Matsukevich *et al.*, "Entanglement of Remote Atomic Qubits," *Phys. Rev. Lett.* **96**, 030405 (2006).

[4] I. Bloch, J. Dalibard, and W. Zwerger, "Many-body physics with ultracold gases," *Rev. Mod. Phys.* **80**, 885 (2008).

[5] M. Saffman, T. G. Walker, and K. Molmer, "Quantum information with Rydberg atoms," *Rev. Mod. Phys.* **82**, 2313 (2010).

[6] A. G. Radnaev, Y. O. Dudin, R. Zhao, H. H. Jen, S. D. Jenkins, A. Kuzmich, and T. A. B. Kennedy, "A quantum memory with telecom-wavelength conversion," *Nature Physics* **6**, 894 (2010).

[7] M. Zwierlein, J. Abo-Shaeer, A. Schirotzek, C. Schunck, and W. Ketterle, "Vortices and superfluidity in a strongly interacting Fermi gas," *Nature* **435**, 1047 (2005).

[8] M. Lukin, M. Fleischhauer, R. Cote, L. Duan, D. Jaksch, J. Cirac, and P. Zoller, "Dipole blockade and quantum information processing in mesoscopic atomic ensembles," *Phys. Rev. Lett.* **87**, 037901 (2001).

[9] M. Saffman and T. J. Walker, "Entangling Single- and N-Atom Qubits for Fast Quantum State Detection and Transmission," *Phys. Rev. A* **72**, 042302 (2005).

[10] M. Müeller, I. Lesanovsky, H. Weimer, H. P. Buechler, and P. Zoller, "Mesoscopic Rydberg Gate Based on Electromagnetically Induced Transparency," *Phys. Rev. Lett.* **102**, 170502 (2009).

[11] B. Olmos, R. Gonzàlez-Fèrez, and I. Lesanovsky, "Fermionic Collective Excitations in a Lattice Gas of Rydberg Atoms," *Phys. Rev. Lett.* **103**, 185302 (2009).

[12] H. Weimer, M. Mueller, I. Lesanovsky, P. Zoller, and H. P. Buechler, "A Rydberg quantum simulator," *Nature Physics* **6**, 382 (2010).

[13] B. Zhao, M. Mueller, K. Hammerer, and P. Zoller, "Efficient quantum repeater based on deterministic Rydberg gates," *Phys. Rev. A* **81**, 052329 (2010).

[14] G. Pupillo, A. Micheli, M. Boninsegni, I. Lesanovsky, and P. Zoller, "Strongly Correlated Gases of Rydberg-Dressed Atoms: Quantum and Classical Dynamics," *Phys. Rev. Lett.* **104**, 223002 (2010).

[15] A. V. Gorshkov, J. Otterbach, M. Fleischhauer, T. Pohl, and M. D. Lukin, "Photon-Photon Interactions via Rydberg Blockade," *Phys. Rev. Lett.* **107**, 133602 (2011).

[16] F. Bariani, Y. O. Dudin, T. A. B. Kennedy, and A. Kuzmich, "Dephasing of Multiparticle Rydberg Excitations for Fast Entanglement Generation," *Phys. Rev. Lett.* **108**, 030501 (2012).

[17] M. Aspelmeyer, H. R. Böhm, T. Gyatso, T. Jennewein, R. Kaltenbaek, M. Lindenthal, G. Molina-Terriza, A. Poppe, K. Resch, M. Taraba, R. Ursin, P. Walther, and A. Zeilinger, "Long-Distance Free-Space Distribution of Quantum Entanglement," *Science* **301**, 621 (2003).

[18] H.-J. Briegel, W. Dür, J. I. Cirac, and P. Zoller, "Quantum Repeaters: The Role of Imperfect Local Operations in Quantum Communication," *Phys. Rev. Lett.* **81**, 5932 (1998).

[19] L.-M. Duan, M. D. Lukin, J. I. Cirac, and P. Zoller, "Long-Distance Quantum Communication with Atomic Ensembles and Linear Optics," *Nature* **414**, 413 (2001).

[20] O. A. Collins, S. D. Jenkins, A. Kuzmich, and T. A. B. Kennedy, "Multiplexed Memory-Insensitive Quantum Repeaters," *Phys. Rev. Lett.* **98**, 060502 (2007).

[21] L. Jiang, J. M. Taylor, and M. D. Lukin, "Fast and robust approach to long-distance quantum communication with atomic ensembles," *Phys. Rev. A* **76**, 012301 (2007).

[22] N. Sangouard, C. Simon, B. Zhao, Y.-A. Chen, H. de Riedmatten, J.-W. Pan, and N. Gisin, "Robust and efficient quantum repeaters with atomic ensembles and linear optics," *Phys. Rev. A* **77**, 062301 (2008).

[23] D. N. Matsukevich, T. Chanelière, S. D. Jenkins, S.-Y. Lan, T. A. B. Kennedy, and A. Kuzmich, "Deterministic Single Photons via Conditional Quantum Evolution," *Phys. Rev. Lett.* **97**, 013601 (2006).

[24] L.-M. Duan, "Entangling Many Atomic Ensembles through Laser Manipulation," *Phys. Rev. Lett.* **88**, 170402 (2002).

[25] U. Schnorrberger, J. D. Thompson, S. Trotzky, R. Pugatch, N. Davidson, S. Kuhr, and I. Bloch, "Electromagnetically Induced Transparency and Light Storage in an Atomic Mott Insulator," *Phys. Rev. Lett.* **103**, 033003 (2009).

[26] H. Katori, M. Takamoto, V. Pal'chikov, and V. Ovsiannikov, "Ultrastable optical clock with neutral atoms in an engineered light shift trap," *Phys. Rev. Lett* **91**, 173005 (2003).

[27] V. V. Flambaum, V. A. Dzuba, and A. Derevianko, "Magic Frequencies for Cesium Primary-Frequency Standard," *Phys. Rev. Lett.* **101**, 220801 (2008).

[28] J. Y. Kim and D. Cho, *J. Korean Phys. Soc.* **37**, 744 (2000).

[29] N. Lundblad, M. Schlosser, and J. V. Porto, "Experimental observation of magic-wavelength behavior of (87)Rb atoms in an optical lattice," *Phys. Rev. A* **81**, 031611 (2010).

[30] Y. O. Dudin, L. Li, and A. Kuzmich, "Light storage on the scale of a minute," *submitted* (2012).

[31] M. Tanasittikosol, J. D. Pritchard, D. Maxwell, A. Gauguet, K. J. Weatherill, R. M. Potvliege, and C. S. Adams, "Microwave dressing of Rydberg dark states," *J. Phys. B* **44**, 184020 (2011).

[32] E. Urban, T. A. Johnson, T. Henage, L. Isenhower, D. D. Yavuz, T. G. Walker, and M. Saffman, "Observation of Rydberg blockade between two atoms," *Nature Physics* **5**, 110 (2009).

[33] A. Gaëtan, Y. Miroshnychenko, T. Wilk, A. Chotia, M. Viteau, D. Comparat, P. Pillet, A. Browaeys, and P. Grangier, "Observation of collective excitation of two individual atoms in the Rydberg blockade regime," *Nature Physics* **5**, 115 (2009).

[34] K. Singer, M. Reetz-Lamour, T. Amthor, L. Marcassa, and M. Weidemuller, "Suppression of excitation and spectral broadening induced by interactions in a cold gas of Rydberg atoms," *Phys. Rev. Lett* **93**, 163001 (2004).

[35] D. Tong, S. Farooqi, J. Stanojevic, S. Krishnan, Y. Zhang, R. Cote, E. Eyler, and P. Gould, "Local blockade of Rydberg excitation in an ultracold gas," *Phys. Rev. Lett.* **93**, 063001 (2004).

[36] T. Liebisch, A. Reinhard, P. Berman, and G. Raithel, "Atom counting statistics in ensembles of interacting Rydberg atoms," *Phys. Rev. Lett.* **95**, 253002 (2005).

[37] T. Vogt, M. Viteau, J. Zhao, A. Chotia, D. Comparat, and P. Pillet, "Dipole blockade at forster resonances in high resolution laser excitation of Rydberg states of cesium atoms," *Phys. Rev. Lett.* **97**, 083003 (2006).

[38] R. Heidemann, U. Raitzsch, V. Bendkowsky, B. Butscher, R. Loew, L. Santos, and T. Pfau, "Evidence for coherent collective Rydberg excitation in the strong blockade regime," *Phys. Rev. Lett.* **99**, 163601 (2007).

[39] E. Brekke, J. O. Day, and T. G. Walker, "Four-wave mixing in ultracold atoms using intermediate Rydberg states," *Phys. Rev. A* **78**, 063830 (2008).

[40] H. Kübler, J. P. Shaffer, T. Baluktsian, R. Loew, and T. Pfau, "Coherent excitation of Rydberg atoms in micrometre-sized atomic vapour cells," *Nature Photonics* **4**, 112 (2010).

[41] J. D. Pritchard, D. Maxwell, A. Gauguet, K. J. Weatherill, M. P. A. Jones, and C. S. Adams, "Cooperative Atom-Light Interaction in a Blockaded Rydberg Ensemble," *Phys. Rev. Lett.* **105**, 193603 (2010).

[42] D. N. Matsukevich and A. Kuzmich, "Quantum State Transfer Between Matter and Light," *Science* **306**, 663 (2004).

[43] E. Brion, K. Molmer, and M. Saffman, "Quantum computing with collective ensembles of multilevel systems," *Phys. Rev. Lett.* **99**, 260501 (2007).

[44] R. Zhao, Y. O. Dudin, S. D. Jenkins, C. J. Campbell, D. N. Matsukevich, T. A. B. Kennedy, and A. Kuzmich, "Long-Lived Quantum Memory," *Nature Physics* **5**, 100 (2009).

[45] Y. O. Dudin, S. D. Jenkins, R. Zhao, D. N. Matsukevich, A. Kuzmich, and T. A. B. Kennedy, "Entanglement of a Photon and an Optical Lattice Spin Wave," *Phys. Rev. Lett.* **103**, 020505 (2009).

[46] M. D. Lukin, "Colloquium: Trapping and Manipulating Photon States in Atomic Ensembles," *Rev. Mod. Phys.* **75**, 457 (2003).

[47] M. Hijlkema, B. Weber, H. P. Specht, S. C. Webster, A. Kuhn, and G. Rempe, "A single-photon server with just one atom," *Nature Physics* **3**, 253 (2007).

[48] T. Chanelière *et al.*, "Quantum Telecommunication Based on Atomic Cascade Transitions," *Phys. Rev. Lett.* **96**, 093604 (2006).

[49] D. N. Matsukevich, T. Chanelière, S. D. Jenkins, S.-Y. Lan, T. A. B. Kennedy, and A. Kuzmich, "Observation of Dark State Polariton Collapses and Revivals," *Phys. Rev. Lett.* **96**, 033601 (2006).

[50] S. D. Jenkins, D. N. Matsukevich, T. Chanelière, A. Kuzmich, and T. A. B. Kennedy, "Theory of Dark-State Polariton Collapses and Revivals," *Phys. Rev. A* **73**, 021803(R) (2006).

[51] D. N. Matsukevich, T. Chanelière, S. D. Jenkins, S.-Y. Lan, T. A. B. Kennedy, and A. Kuzmich, "Entanglement of Remote Atomic Qubits," *Phys. Rev. Lett.* **96**, 030405 (2006).

[52] J. Simon, H. Tanji, S. Ghosh, and V. Vuletić, "Single-Photon Bus Connecting Spin-Wave Quantum Memories," *Nature Physics* **3**, 765 (2007).

[53] J. Laurat, K. S. Choi, H. Deng, C. W. Chou, and H. J. Kimble, "Heralded entanglement between atomic ensembles: Preparation, decoherence, and scaling," *Phys. Rev. Lett.* **99**, 180504 (2007).

[54] Y.-A. Chen *et al.*, "Memory-Built-In Quantum Teleportation with Photonic and Atomic Qubits," *Nature Physics* **4**, 103 (2008).

[55] K. S. Choi, H. Deng, J. Laurat, and H. J. Kimble, "Mapping photonic entanglement into and out of a quantum memory," *Nature* **452**, 67 (2008).

[56] C. Liu, Z. Dutton, C. H. Behroozi, and L. V. Hau, "Observation of Coherent Optical Information Storage in an Atomic Medium Using Halted Light Pulses," *Nature* **409**, 490 (2001).

[57] D. F. Phillips, A. Fleischhauer, A. Mair, R. L. Walsworth, and M. D. Lukin, "Storage of Light in Atomic Vapor," *Phys. Rev. Lett.* **86**, 783 (2001).

[58] B. Julsgaard, J. Sherson, J. I. Cirac, J. Fiurášek, and E. S. Polzik, "Experimental Demonstration of Quantum Memory for Light," *Nature* **432**, 482 (2004).

[59] J. Longdell, E. Fraval, M. Sellars, and N. Manson, "Stopped light with storage times greater than one second using electromagnetically induced transparency in a solid," *Phys. Rev. Lett.* **95**, 063601 (2005).

[60] P. Grangier, G. Roger, and A. Aspect, "Experimental Evidence for a Photon Anticorrelation Effect on a Beam Splitter: A New Light on Single-Photon Interferences," *Europhys. Lett.* **1**, 173 (1986).

[61] T. Chanelière, D. N. Matsukevich, S. D. Jenkins, S. Y. Lan, R. Zhao, T. A. B. Kennedy, and A. Kuzmich, "Quantum interference of electromagnetic fields from remote quantum memories," *Phys. Rev. Lett.* **98**, 113602 (2007).

[62] D. Harber, H. Lewandowski, J. McGuirk, and E. Cornell, "Effect of cold collisions on spin coherence and resonance shifts in a magnetically trapped ultracold gas," *Phys. Rev. A* **66**, 053616 (2002).

[63] M. Fleischhauer and M. D. Lukin, "Dark-state Polaritons in Electromagnetically Induced Transparency," *Phys. Rev. Lett.* **84**, 5094 (2000).

[64] J. S. Bell, *Physics (Long Island City, N.Y.)* **1**, 195 (1964).

[65] J. S. Bell, *Rev. Mod. Phys.* **38**, 447 (1966).

[66] J. F. Clauser, M. A. Horne, A. Shimony, and R. A. Holt, "Proposed Experiment to Test Local Hidden-Variable Theories," *Phys. Rev. Lett.* **23**, 880 (1969).

[67] S. D. Jenkins, Y. O. Dudin, R. Zhao, D. N. Matsukevich, A. Kuzmich, and T. A. B. Kennedy, "*In situ* determination of Zeeman content of collective atomic memories," *J. Phys. B* **45**, 124006 (2012).

[68] Y. O. Dudin, R. Zhao, T. A. B. Kennedy, and A. Kuzmich, "Light storage in a magnetically dressed optical lattice," *Phys. Rev. A* **103**, 020505 (2009).

[69] Y. O. Dudin, A. G. Radnaev, R. Zhao, J. Z. Blumoff, T. A. B. Kennedy, and A. Kuzmich, "Entanglement of Light-Shift Compensated Atomic Spin Waves with Telecom Light," *Phys. Rev. Lett.* **105**, 260502 (2010).

[70] A. Kaplan, M. Andersen, and N. Davidson, "Suppression of inhomogeneous broadening in rf spectroscopy of optically trapped atoms," *Phys. Rev. A* **66**, 045401 (2002).

[71] D. F. Walls and G. J. Milburn, *Quantum Optics* (Springer-Verlag, Berlin, 1994).

[72] N. L. Manakov, V. D. Ovsiannikov, and L. P. Rapoport, *Phys. Rep.* **141**, 320 (1986).

[73] A. Derevianko, "Theory of magic optical traps for Zeeman-insensitive clock transitions in alkali-metal atoms," *Phys. Rev. A* **81**, 051606 (2010).

[74] S. Kuppens, K. Corwin, K. Miller, T. Chupp, and C. Wieman, "Loading an optical dipole trap," *Phys. Rev. A* **62**, 013406 (2000).

[75] D. N. Matsukevich, T. Chanelière, M. Bhattacharya, S.-Y. Lan, S. D. Jenkins, T. A. B. Kennedy, and A. Kuzmich, "Entanglement of a Photon and a Collective Atomic Excitation," *Phys. Rev. Lett.* **95**, 040405 (2005).

[76] S. Chen, Y.-A. Chen, B. Zhao, Z.-S. Yuan, J. Schmiedmayer, and J.-W. Pan, "Demonstration of a Stable Atom-Photon Entanglement Source for Quantum Repeaters," *Phys. Rev. Lett.* **99**, 180505 (2007).

[77] W. Rosenfeld, F. Hocke, F. Henkel, M. Krug, J. Volz, M. Weber, and H. Weinfurter, "Towards Long-Distance Atom-Photon Entanglement," *Phys. Rev. Lett.* **101**, 260403 (2008).

[78] B. B. Blinov, D. L. Moehring, L.-M. Duan, and C. Monroe, "Observation of Entanglement Between a Single Trapped Atom and a Single Photon," *Nature* **428**, 153 (2004).

[79] E. Togan, Y. Chu, A. S. Trifonov, L. Jiang, J. Maze, L. Childress, M. V. G. Dutt, A. S. Sorensen, P. R. Hemmer, A. S. Zibrov, and M. D. Lukin, "Quantum entanglement between an optical photon and a solid-state spin qubit," *Nature* **466**, 730 (2010).

[80] R. T. Willis, F. E. Becerra, L. A. Orozco, and S. L. Rolston, "Four-wave mixing in the diamond configuration in an atomic vapor," *Phys. Rev. A* **79**, 033814 (2009).

[81] H. H. Jen and T. A. B. Kennedy, "Efficiency of light-frequency conversion in an atomic ensemble," *Phys. Rev. A* **82**, 023815 (2010).

[82] U. Haeberlen, *High Resolution NMR in Solids (Advances in Magnetic Resonance Series)* (Academic, 1976).

[83] L. Viola and S. Lloyd, "Dynamical suppression of decoherence in two-state quantum systems," *Phys. Rev. A* **58**, 733 (1998).

[84] L. Vandersypen and I. Chuang, "NMR techniques for quantum control and computation," *Rev. Mod. Phys.* **76**, 1037 (2004).

[85] M. J. Biercuk, H. Uys, A. P. VanDevender, N. Shiga, W. M. Itano, and J. J. Bollinger, "Optimized dynamical decoupling in a model quantum memory," *Nature* **458**, 996 (2009).

[86] Y. Sagi, I. Almog, and N. Davidson, "Process Tomography of Dynamical Decoupling in a Dense Cold Atomic Ensemble," *Phys. Rev. Lett.* **105**, 053201 (2010).

[87] S. Meiboom and D. Gill, "Modified spin-echo method for measuring nuclear relaxation times," *Rev. Sci. Instr.* **29**, 688 (1958).

[88] Y. O. Dudin and A. Kuzmich, "Strongly Interacting Rydberg Excitations of a Cold Atomic Gas," *Science* **336**, 887 (2012).

[89] A. Polkovnikov, K. Sengupta, A. Silva, and M. Vengalattore, "Colloquium: Nonequilibrium dynamics of closed interacting quantum systems," *Rev. Mod. Phys.* **83**, 863 (2011).

[90] T. Förster, "Zwischenmolekulare energiewanderung und fluoreszenz," *Ann. d. Physik* **437**, 55 (1948).

[91] T. G. Walker and M. Saffman, "Consequences of Zeeman degeneracy for the van der Waals blockade between Rydberg atoms," *Phys. Rev. A* **77**, 032723 (2008).

[92] T. Pohl and P. R. Berman, "Breaking the Dipole Blockade: Nearly Resonant Dipole Interactions in Few-Atom Systems," *Phys. Rev. Lett.* **102**, 013004 (2009).

[93] W. Li, I. Mourachko, M. Noel, and T. Gallagher, "Millimeter-wave spectroscopy of cold Rb Rydberg atoms in a magneto-optical trap: Quantum defects of the ns, np, and nd series," *Phys. Rev. A* **67**, 052502 (2003).

[94] F. Cummings and A. Dorri, "Exact solution for spontaneous emission in the presence of N atoms," *Phys. Rev. A* **28**, 2282 (1983).

[95] F. Bariani and T. A. B. Kennedy, "Retrieval of multiple spin waves from a weakly excited, metastable atomic ensemble," *Phys. Rev. A* **85**, 033811 (2012).

[96] S. Zhang, F. Robicheaux, and M. Saffman, "Magic-wavelength optical traps for Rydberg atoms," *Phys. Rev. A* **84**, 043408 (2011).

[97] B. Kaulakys, "Consistent analytical approach for the quasi-classical radial dipole matrix elements," *J. Phys. B* **28**, 4963 (1995).

[98] K. C. Younge, B. Knuffman, S. E. Anderson, and G. Raithel, "State-Dependent Energy Shifts of Rydberg Atoms in a Ponderomotive Optical Lattice," *Phys. Rev. Lett* **104**, 173005 (2010).

[99] Y. O. Dudin, F. Bariani, and A. Kuzmich, "Emergence of long-range correlations in a cold atomic gas," *arXiv:1205.4708* (2012).

[100] J. Stanojevic, V. Parigi, E. Bimbard, A. Ourjoumtsev, P. Pillet, and P. Grangier, "Generating non-Gaussian states using collisions between Rydberg polaritons," *arXiv:1203.6764* (2012).

[101] T. Pohl, E. Demler, and M. D. Lukin, "Dynamical Crystallization in the Dipole Blockade of Ultracold Atoms," *Phys. Rev. Lett.* **104**, 043002 (2010).

[102] J. Schachenmayer, I. Lesanovsky, A. Micheli, and A. J. Daley, "Dynamical crystal creation with polar molecules or Rydberg atoms in optical lattices," *New J. Phys.* **13**, 059503 (2011).

[103] C. Ates and I. Lesanovsky, "Entropic enhancement of spatial correlations in a laser-driven Rydberg gas," *arXiv:1202.2012* (2012).

[104] B. Olmos, W. Li, S. Hofferberth, and I. Lesanovsky, "Amplifying single impurities immersed in a gas of ultracold atoms," *Phys. Rev. A* **84**, 041607 (2011).

[105] G. Günter, M. Robert-de Saint-Vincent, H. Schempp, C. S. Hofmann, S. Whitlock, and M. Weidemüller, "Interaction Enhanced Imaging of Individual Rydberg Atoms in Dense Gases," *Phys. Rev. Lett.* **108**, 013002 (2012).

[106] Y. O. Dudin, L. Li, F. Bariani, and A. Kuzmich, "Observation of coherent many-body Rabi oscillations," *arXiv:1205.7061* (2012).

[107] D. J. Griffiths, *Introduction to quantum mechanics* (Pearson Prentice Hall, 2005).

[108] I. Rabi, S. Millman, P. Kusch, and J. Zacharias, "The molecular beam resonance method for measuring nuclear magnetic moments," *Phys. Rev.* **55**, 0526 (1939).

[109] N. Ramsey, *Molecular Beams* (Clarendon Press, Oxford, 1985).

[110] R. H. Dicke, "Coherence in Spontaneous Radiation Processes," *Phys. Rev.* **93**, 99 (1954).

[111] R. H. Dicke, "Interaction-free quantum measurements: A paradox?," *American Journal of Physics* **49**, 925 (1981).

[112] L. Allen and J. H. Eberly, *Two-level atoms and optical resonance* (Dover Publications, Mineola, 1987).

[113] T. F. Gallagher, *Rydberg atoms* (Cambridge University Press, Cambridge, 1994).

[114] M. Saffman and T. Walker, "Creating single-atom and single-photon sources from entangled atomic ensembles," *Phys. Rev. A* **66**, 065403 (2002).

[115] J. Stanojevic and R. Cote, "Many-body Rabi oscillations of Rydberg excitation in small mesoscopic samples," *Phys. Rev. A* **80**, 033418 (2009).

[116] M. Viteau, M. G. Bason, J. Radogostowicz, N. Malossi, D. Ciampini, O. Morsch, and E. Arimondo, "Rydberg Excitations in Bose-Einstein Condensates in Quasi-One-Dimensional Potentials and Optical Lattices," *Phys. Rev. Lett.* **107**, 060402 (2011).

[117] J. Deiglmayr, M. Reetz-Lamour, T. Amthor, S. Westermann, A. L. de Oliveira, and M. Weidemüeller, "Coherent excitation of Rydberg atoms in an ultracold gas," *Opt. Comm.* **264**, 293 (2006).

[118] M. Prevedelli, F. Cataliotti, E. Cornell, J. Ensher, C. Fort, L. Ricci, G. Tino, and M. Inguscio, "Trapping and cooling of potassium isotopes in a double-magneto-optical-trap apparatus," *Phys. Rev. A* **59**, 886 (1999).

[119] Z. Lu, K. Corwin, M. Renn, M. Anderson, E. Cornell, and C. Wieman, "Low-velocity intense source of atoms from a magneto-optical trap," *Phys. Rev. Lett.* **77**, 3331 (1996).

[120] C. Dedman, J. Nes, T. Hanna, R. Dall, K. Baldwin, and A. Truscott, "Optimum design and construction of a Zeeman slower for use with a magneto-optic trap," *Rev. Sci. Instr.* **75**, 5136 (2004).

[121] K. Dieckmann, R. Spreeuw, M. Weidemuller, and J. Walraven, "Two-dimensional magneto-optical trap as a source of slow atoms," *Phys. Rev. A* **58**, 3891 (1998).

[122] S. Chaudhuri, S. Roy, and C. S. Unnikrishnan, "Realization of an intense cold Rb atomic beam based on a two-dimensional magneto-optical trap: Experiments and comparison with simulations," *Phys. Rev. A* **74**, 023406 (2006).

[123] R. Drever, J. Hall, F. Kowalski, J. Hough, G. Ford, A. Munley, and H. Ward, "Laser Phase and Frequency Stabilization Using an Optical Resonator," *Appl. Phys. B* **31**, 97 (1983).

LIST OF PUBLICATIONS

[1] R. Zhao, Y. O. Dudin, S. D. Jenkins, C. J. Campbell, D. N. Matsukevich, T. A. B. Kennedy and A. Kuzmich, "Long-Lived Quantum Memory," *Nature Physics* **5**, 100 (2009).

[2] Y. O. Dudin, S. D. Jenkins, R. Zhao, D. N. Matsukevich, A. Kuzmich, and T. A. B. Kennedy, "Entanglement of a Photon and an Optical Lattice Spin Wave," *Phys. Rev. Lett.* **103**, 020505 (2009).

[3] Y. O. Dudin, R. Zhao, T. A. B. Kennedy, and A. Kuzmich, "Light Storage in a Magnetically Dressed Optical Lattice," *Phys. Rev. A* **81**, 041805(R) (2010).

[4] A. G. Radnaev, Y. O. Dudin, R. Zhao, H. H. Jen, S. D. Jenkins, A. Kuzmich and T. A. B. Kennedy, "A Quantum Memory with Telecom-Wavelength Conversion," *Nature Physics* **6**, 894 (2010).

[5] Y. O. Dudin, A. G. Radnaev, R. Zhao, J. Z. Blumoff, T. A. B. Kennedy, and A. Kuzmich, "Entanglement of Light-Shift Compensated Atomic Spin Waves with Telecom Light," *Phys. Rev. Lett.* **105**, 260502 (2010).

[6] F. Bariani, Y. O. Dudin, T. A. B. Kennedy, A. Kuzmich, "Dephasing of Multiparticle Rydberg Excitations for Fast Entanglement Generation," *Phys. Rev. Lett.* **108**, 030501 (2012).

[7] S. D. Jenkins, Y. O. Dudin, R. Zhao, D. N. Matsukevich, A. Kuzmich, and T. A. B. Kennedy, "In Situ Determination of Zeeman Content of Collective Atomic Memories," *J. Phys. B* **45**, 124006 (2012).

[8] Y. O. Dudin and A. Kuzmich, "Strongly Interacting Quantum Excitations of a Cold Atomic Gas," *Science* **336**, 887 (2012).

[9] Y. O. Dudin, F. Bariani, and A. Kuzmich, "Emergence of long-range correlations in a cold atomic gas," *arXiv:1205.4708* (2012).

[10] Y. O. Dudin, L. Li, F. Bariani, and A. Kuzmich, "Observation of coherent many-body Rabi oscillations," *arXiv:1205.7061* (2012).

[11] Y. O. Dudin, L. Li, and A. Kuzmich, "Light storage on the scale of a minute," *submitted* (2012).